UNIVERSITAT POLITÈCNICA DE CATALUNYA
BARCELONATECH

Operation of HVDC converters for transformer inrush current reduction

Zahra Solh Joukhah

ADVERTIMENT La consulta d'aquesta tesi queda condicionada a l'acceptació de les següents condicions d'ús: La difusió d'aquesta tesi per mitjà del repositori institucional UPCommons (http://upcommons.upc.edu/tesis) i el repositori cooperatiu TDX (http://www.tdx.cat/) ha estat autoritzada pels titulars dels drets de propietat intel·lectual **únicament per a usos privats** emmarcats en activitats d'investigació i docència. No s'autoritza la seva reproducció amb finalitats de lucre ni la seva difusió i posada a disposició des d'un lloc aliè al servei UPCommons o TDX. No s'autoritza la presentació del seu contingut en una finestra o marc aliè a UPCommons (*framing*). Aquesta reserva de drets afecta tant al resum de presentació de la tesi com als seus continguts. En la utilització o cita de parts de la tesi és obligat indicar el nom de la persona autora.

ADVERTENCIA La consulta de esta tesis queda condicionada a la aceptación de las siguientes condiciones de uso: La difusión de esta tesis por medio del repositorio institucional UPCommons (http://upcommons.upc.edu/tesis) y el repositorio cooperativo TDR (http://www.tdx.cat/?locale-attribute=es) ha sido autorizada por los titulares de los derechos de propiedad intelectual **únicamente para usos privados enmarcados** en actividades de investigación y docencia. No se autoriza su reproducción con finalidades de lucro ni su difusión y puesta a disposición desde un sitio ajeno al servicio UPCommons No se autoriza la presentación de su contenido en una ventana o marco ajeno a UPCommons (*framing)*. Esta reserva de derechos afecta tanto al resumen de presentación de la tesis como a sus contenidos. En la utilización o cita de partes de la tesis es obligado indicar el nombre de la persona autora.

WARNING On having consulted this thesis you're accepting the following use conditions: Spreading this thesis by the institutional repository UPCommons (http://upcommons.upc.edu/tesis) and the cooperative repository TDX (http://www.tdx.cat/?locale-attribute=en) has been authorized by the titular of the intellectual property rights **only for private uses** placed in investigation and teaching activities. Reproduction with lucrative aims is not authorized neither its spreading nor availability from a site foreign to the UPCommons service. Introducing its content in a window or frame foreign to the UPCommons service is not authorized (framing). These rights affect to the presentation summary of the thesis as well as to its contents. In the using or citation of parts of the thesis it's obliged to indicate the name of the author.

Universitat Politècnica de Catalunya

Departament d'Enginyeria Elèctrica

Departament d'Enginyeria Elèctrica
UNIVERSITAT POLITÈCNICA DE CATALUNYA

CITCEA - Centre d'Innovació Tecnològica
en Convertidors Estàtics i Accionaments

Doctoral Thesis

Operation of HVDC converters for transformer inrush current reduction

Autor: **Zahra Solh Joukhah**

Directors: **Andreas Sumper**
Agustí Egea-Àlvarez
Tutor: **Oriol Gomis-Bellmunt**

Barcelona, September 2017

Universitat Politècnica de Catalunya
Departament d'Enginyeria Elèctrica
Centre d'Innovació Tecnològica en Convertidors Estàtics i Accionament
Av. Diagonal, 647. Pl. 2
08028 Barcelona

Imprès a Barcelona
Primera impressió, September 2017

UNIVERSITAT POLITÈCNICA DE CATALUNYA
BARCELONATECH
Escola de Doctorat

Curso académico:2016-2017

Acta de calificación de tesis doctoral

Nombre y apellidos
Zahra Solh Joukhah

Programa de doctorado
Doctorat en Enginyeria Elèctrica

Unidad estructural responsable del programa

Resolución del Tribunal

Reunido el Tribunal designado a tal efecto, el doctorando / la doctoranda expone el tema de la su tesis doctoral titulada __ Operation of power Systems including Multi-Terminal HVDC grids.

Acabada la lectura y después de dar respuesta a las cuestiones formuladas por los miembros titulares del tribunal, éste otorga la calificación:

☐ NO APTO ☐ APROBADO ☐ NOTABLE ☐ SOBRESALIENTE

(Nombre, apellidos y firma) Presidente/a	(Nombre, apellidos y firma) Secretario/a

(Nombre, apellidos y firma) Vocal	(Nombre, apellidos y firma) Vocal	(Nombre, apellidos y firma) Vocal

______________________, _______ de __________________ de _______________

El resultado del escrutinio de los votos emitidos por los miembros titulares del tribunal, efectuado por la Escuela de Doctorado, a instancia de la Comisión de Doctorado de la UPC, otorga la MENCIÓN CUM LAUDE:

☐ SÍ ☐ NO

(Nombre, apellidos y firma) Presidente de la Comisión Permanente de la Escuela de Doctorado	(Nombre, apellidos y firma) Secretario de la Comisión Permanente de la Escuela de Doctorado

Barcelona a _______ de ____________________ de __________

To Hadi, Kimia, Mehdi, Arash, Kourosh and Elahe
who have shared in all my joys and sorrows, my trials,
failures and achievements; and whose love
courage and devotion have been the
strength of my striving,
this thesis is affectionately dedicated.

Acknowledgements

I wish to express my acknowledgement to my PhD supervisors: Dr.Andreas Sumper, Dr.Agusti Egea-Alvarez and Dr.Oriol Gomis-Bellmunt for the thoughtful guidance and support of this work. Their suggestions and comments, in many technical discussions have essentially contributed to the success of this work.

Furthermore, thanks to Toni Sudria, Roberto, Montesinos and Samuel Galceran for their help and valuable advice. I also would like to thank my colleagues at CITCEA-UPC, Monica Aragues, Ingrid Munne, Edu Prieto, Edu Bullich, Pau Lloret, Francesc Girbau, Rodrigo Teixeira, Pol Olivella, Ricard Ferrer, Joan Sau, Paco, Muhammad Raza, Ana Cabrera, Abel, Kevin, Carlos Collados, Joan Marc, Collados, Quim, Andreu and Gerard for their support and the enjoyable moments shared while working/learning.

Finally and most important, I would like to thank my parents, husband, brothers and sister for their support, encouragement, patience and understanding to reach my wishes over the last years.

Afsaneh
(Zahra)

Abstract

The present PhD thesis deals with transformer inrush current in offshore grids including offshore wind farms and High Voltage Direct Current (HVDC) transmission systems. The inrush phenomenon during transformers energization or recovery after the fault clearance is one of important concerns in offshore systems which can threaten the security and reliability of the HVDC grid operation as well as the wind farms function. Hence, the behaviour of wind turbines, Voltage Source Converters (VSC) and transformer under the normal operation and the inrush transient mode is analyzed.

For inrush current reduction in the procedure of the offshore wind farms start-up and integration into the onshore AC grid, a technique based on Voltage Ramping Strategy (VRS) is proposed and its performance is compared with the operation of system without consideration of this approach. The new methodology which is simple, cost-effective ensures minimization of transformer inrush current in the offshore systems and the enhancement of power quality and the reliability of grid under the transformer energizing condition. The mentioned method can develop much lower inrush currents according to the slower voltage ramp slopes.

Concerning the recovery inrush current, the operation of the offshore grid especially transformers is analyzed under the fault and the system restoration modes. The recovery inrush transient of transformers can cause tripping the HVDC and wind farms converters as well as disturbing the HVDC power transmission. A voltage control design based on VRS is proposed in HVDC converter to recover all the transformers in offshore grid with lower inrush currents. The control system proposed can assure the correct performance of the converters in HVDC system and in wind farm and also the robust stability of the offshore grid.

Resumen

Esta tesis doctoral estudia las corrientes de energización de transformadores de parques eólicos marinos con aerogeneradores con convertidores en fuente de tensión (VSC) de plena potencia conectados a través de una conexión de Alta Tensión en Corriente Continua (HVDC). Las corrientes de energización pueden disminuir la fiabilidad de la transmisión eléctrica debido a disparos intempestivos de las protecciones durante la puesta en marcha o recuperación de una falta.

Para la mitigación de las corrientes de energización durante la puesta en marcha del parque esta tesis propone una nueva estrategia basada en incrementar la tensión aplicada por el convertidor del parque eólico en forma de rampa (VRS). Este método persigue energizar el parque eólico con el menor coste y máxima fiabilidad. La tesis analiza diferentes escenarios y diferentes rampas.

Otro momento en que las corrientes de energización pueden dar lugar a un disparo intempestivo de las protecciones es durante la recuperación de una falta en la red de alterna del parque eólico marino. Esta tesis extiende la estrategia VRS, utilizada durante la puesta en marcha del convertidor del parque, para los escenarios de recuperación de una falta.

Contents

List of Figures

List of Tables

Nomenclature

CITCEA	Centre d'Innovació en Convertidors Estàtics i Accionaments
UPC	Universitat Politécnica de Catalunya
AC	Alternating Current
DC	Direct Current
HV	High Voltage
HF	High Frequency
DFIG	Doubly Fed Induction Generator
PMSG	Permanent Magnet Synchronous Genrator
HVAC	High Voltage Alternating Current
HVDC	High Voltage Direct Current
LCC	Line Commuted Converter
VSC	Voltage Source Converter
MTDC	Multi-Terminal HVDC
VRS	Voltage Ramping Strategy
WT	Wind Turbine
SCIG	Squirrel Cage Induction Genrator
WRIG	Wound Rotor Induction Generator
WRSG	Wound Rotor Synchronous Generator
CSC	Current Source Converter
IGBT	Insulated-Gate Bipolar Transistor
MOSFET	Metal-Oxide-Semiconductor Field-Effect Transistor
MMC	Modular Multilevel Converters
PWM	Pulse Width Modulation
GRT	General Ring Topology
ST	Star Topology
SGRT	Star with a General Ring Topology
WFRT	Wind Farm Ring Topology
SSRT	Substations Ring Topology
PLL	Phase Locked Loop
PCC	Point of Common Coupling

IMC	Internal Model Control
PI	Proportional-Integral Controller
VCO	Voltage Controlled Oscillator
LQG	Linear-Quadratic-Gaussian
MSC	Machine Side Converter
GSC	Grid Side Converter
STC	Saturable Transformer Component model
CB	Circuit Breaker
WTT	Wind Turbines Transformer
FRT	Fault Ride-Through
FCTD	Fault Clearance Time Detection

Chapter 1

Introduction

1.1 Context

Over the past decades, the most prevalent energy sources applied for electricity generation were fossil fuels, falling or flowing water and nuclear fission. The main disadvantages of using sources such as fossil fuels and nuclear fission are harmful environmental effects, limitation of fossil sources, the nuclear risk issue and some countries dependency on other countries for these important sources [4, 5]. Due to the increasing concerns for these difficulties, renewable energy resources are used for satisfying rising need for electricity. Nowadays, these electrical sources play a key role in the electricity industry.

In recent years, energy policies have been built up for Europe Union which its use would allow for the possibility of improving the EUs energy efficiency by 20%, decreasing CO_2 and greenhouse gas emissions by 20% and increasing 20 percent of renewable energy sources in EU energy mix [6]. In fact, these targets would lead to increment of energy security, reduction of climate change, environmental pollution mitigation, renewable energy market development and economic benefits.

One of the most important non-polluting and sustainable electricity generation technologies from renewable energy sources is power plants based on wind. These plants can be located in the situations of onshore or offshore. Due to the lack of proper onshore wind sites, the expansion in wind power further has been proceeded towards offshore wind power plants during last few years.

The offshore wind farms offer significant advantages in comparison with the onshore concepts, such as having stronger and steadier wind speeds in the marine plants, lower installation limitations, higher service life and their compatibility with environment [7]. However, these systems are more expensive than onshore technologies [8].

Focusing on wind turbine of offshore wind farms, two distinguished technologies are being mounted which include: Doubly Fed Induction Generator (DFIG) and Permanent Magnet Synchronous Generator (PMSG). Nowadays, for maintenance costs reduction of the offshore wind turbines, the tendency of wind turbine manufacturers is rather to install PMSG. Although the PMSG type has many constructive options, the direct-driven PMSG with full rated power converter is the most interesting concept presented for offshore wind turbines [4]. The important advantage of this configuration is that the generator is entirely decoupled from the AC power system through full power converters. This feature contrasts with the DFIG in which the stator is directly linked to the AC network. Therefore, this leads in turn to a lower sensitivity of the generator against grid fluctuations. In addition, this topology can operate under different modes of AC power system, due to its implementation with modern approaches.

Moving on offshore wind systems, there are engineering challenges related to the transfer of power produced by offshore wind farms into the mainland Alternating Current (AC) power systems. Various transmission systems have been proposed to solve these challenges which High Voltage Alternating Current (HVAC) is one of the possible solutions. In terms of economic issues, this technology is not cost-effective for long transmission distances over 100 km from the shore [9]. The reason of this fact is that the power transmission using HVAC technology can cause a considerable reactive power in the conductors as well as high power losses which makes the requirement for the compensation devices installation possible [9, 10, 11]. Therefore, High Voltage Direct Current (HVDC) transmission systems have been attracting much attention for integration of the large-scale wind farms far away from the shore into the AC power network [12]. These HVDC technologies actually allow to transmit higher electrical power over longer distances, interconnect the asynchronous systems and transfer the submarine and underground cables [4, 13]. However, these systems have drawbacks compared to AC systems including higher investment costs, and higher losses in short distances [14].

Initially, Line Commutated Converter (LCC) based on HVDC was the most prevalent technology to achieve the abovementioned aim [15]. However, with the development of power electronic devices and the emersion of modern power converters, the HVDC technology based on Voltage Sourced Converters (VSC-HVDC) became a convenient option for transferring offshore wind power into the onshore power grids. In the offshore applications, the VSC converters have a better performance than the LCC converters thanks to their numerous features, such as compact filters, independent active and reactive power regulation, steady control of AC voltage, no commutation failure and black-start ability [15]. However, the main disadvantage of this technology is high losses of converter due to switching [11].

The first topology applied for offshore DC transmission networks is point-to-point HVDC links. These offshore HVDC grids are used for direct connection of an offshore converter station into a main AC power grid. A Multi-Terminal HVDC (MTDC) system is a newfound solution which several large offshore wind farms can be interfaced into various onshore AC networks. However, these meshed DC grids contain technical challenges related to control [16] and protection [15] issues.

To adapt the voltage of the offshore converter station and the voltage of the offshore wind farm platform, a power transformer is applied. During the start-up procedure of the offshore wind farm and the voltage recovery process of the offshore grid, the power transformer will experience a high inrush current due to the sudden enhancement of AC voltage across the transformer winding [17, 18]. The manifestation of this transient current has adverse effects on the offshore power network, such as tripping of VSC and disturbance in HVDC system operation. Hence, the reduction of these inrush currents has grown in importance. Over the previous decades, various techniques have been suggested in order to decrease the current to the minimum possible level. Nevertheless, as far as the author of the thesis knows, there is a research for the reduction of the transformer inrush current in HVDC systems that can be found in literature [19]. Therefore, there is still much research to be done in this topic. Hence, this thesis will propose a new Voltage Ramping Strategy (VRS) for inrush current diminution in offshore grids, based on the gradual increase of the voltage employed in the transformers primary winding.
The main goal of this thesis is to ensure the correct behavior of the HVDC converter in the cases of energization and restoration of the offshore grids transformers, taking into account the proposed technique in the HVDC converter. In this direction, the studies developed can be classified in the two categories below:

- Operation and control of offshore HVDC converters for reduction of transformers energization inrush current.

- Operation and control of HVDC converter for recovery inrush current decrement of the offshore transformers.

1.2 objectives and scope

- **Explain the main components applied to the offshore grids, their topology and integration.** A detailed description of wind turbine types is presented. Also, the offshore collection grid structures and different converter topologies are analyzed. In addition, the HVDC transmission system for interconnection between offshore wind power plants and onshore AC grid is discussed. This study reveals the trend towards the utilization of variable-speed wind turbines equipped with a full power converter and two-level VSC based HVDC transmission systems.

- **Present a dynamic model and different control schemes for a VSC, ensuring the optimal performance of the converter and the stability of the HVDC transmission grid.** The goal of this literature is to represent an average model for converter in order to study the dynamic response of converter at low frequencies. Representations of AC grid filters and DC link of power converter are also presented to design various control systems for the VSC converter. The controllers considered are based on the vector control strategy and ensure better performance of the converter under different operating modes. In addition, this work analyzes the Phase Locked Loop (PLL), current loop and the AC and DC voltage loop dynamics for the control system design.

- **Study a simplified model and a control system for variable speed wind turbine equipped with full power converter to investigate its behaviour in case of transformer inrush transient.** To reflect the dynamic behavior of wind turbines under different wind speeds, a simplified model is presented. This simplification compounds all the models related to the turbine, the drive train, the generator and the machine side converter. Also, the DC bus and the controllers of the mentioned wind turbine are modeled. The DC bus voltage regulation assuring the stability of the system is supported by the converter at the offshore wind turbine grid side.

- **Analyze the transformer inrush current phenomenon in the HVDC systems (disadvantages, effective parameters, etc.), investigate various solutions for inrush transient decrement and design a model for transformer considering the non-linear characteristics of the magnetic core.** Inrush transient of the transformer is caused by a sudden variation of the transformer voltage during energization and restoration conditions. This transient phenomenon can result in the tripping of the HVDC converter due to the current saturation and, consequently, disturbing of the HVDC system operation. Over the last decades, several methodologies based on the insertion of a resistor, controlled switching and variation of residual flux were employed to limit this high inrush current. The application of the mentioned technologies to the HVDC systems is not convenient due to costly, high losses, low reliability and requirement of knowledge of the core residual flux. Furthermore, to analyze the inrush current of the transformer, a T-equivalent circuit model is designed. The transformer behavior in case of core saturation can be approximated by means of this dynamic model. Also, this model is validated using simulation for worst-case scenario of the inrush currents.

- **Design a new strategy to reduce inrush current of HVDC transformer during the start-up and integration of the offshore wind farm into the onshore AC system.** The design of the proposed reduction method is based on the ramping of the voltage in the high voltage terminal of HVDC transformer. The implementation of the mentioned approach is carried out in the control system of the offshore converter. The procedure of the offshore wind farm start-up and integration is analyzed, based on this process, the offshore converter can also provide a smooth start-up for offshore wind farm. Moreover, this reduction design can be confirmed by a comparison between the performance of the system with considered technique and its performance without this approach.

- **Design a voltage ramping strategy-based control system for recovery inrush current diminution of offshore transformers.**

The emersion of transformers recovery inrush currents in offshore grids can influence the operation of available converters. To minimize these transient currents during grid recovery, a voltage control scheme is designed based on Voltage Ramping Strategy (VRS). The proposed control strategy needs a process to reflect the voltage drops due to the fault occurred, as well as to create the considered ramp for the system voltage restoration. Furthermore, the proposed scheme is compared to the control system without this new strategy in order to show the achievement of lower inrush currents in the offshore grids.

1.3 Thesis outline

This PhD represents a novel technique for transformer inrush current reduction during start-up and integration of an offshore wind farm into the onshore AC grid and during the recovery of offshore grid after fault clearance. Further information of each of the chapters of this thesis is included below:

- **Chapter 2** explains the structure of the offshore grid in wind power plants. All sectors of the grid including the wind turbine, collection grid, transformer, converter and HVDC system are discussed in detail.

- **Chapter 3** presents an average model for converter as well as models for AC grid coupling filter including inductive and inductive-capacitive, and for DC grid with back-to-back, point-to-point and multi-terminal configurations. Moreover, different control schemes for power converter are elaborated.

- **Chapter 4** describes a simplified model and a control design for a full power converter wind turbine in offshore grid. Finally, a simulation is carried out to validate the referred representation.

- **Chapter 5** deals with the transient inrush current of transformers in HVDC systems as well as some technologies for restriction of this high current. Furthermore, a dynamic model is presented to analyze transformers behavior in the case of core saturation.

- **Chapter 6** explains a voltage ramping strategy for decrement of the HVDC transformer inrush current during process of the start-up and integration of an offshore wind farm into the main AC system.

- **Chapter 7** presents a control system developed to diminish the recovery inrush current of the entire transformers available in the offshore grid, considering a framework for the voltage restoration.

- **Chapter 8** draws the results and Conclusions of this thesis.

Chapter 2

Offshore grid structure for wind power plants

Explanation of offshore grid structure for a better analysis of the model and control of components applied to the grid is the objective of this chapter.

2.1 Introduction

Offshore wind power plants are one of the fastest-growing renewable energy generation plants in the last few years [20]. This is due to the fact that these offshore technologies offer better characteristics compared to the onshore wind farms [7]. On the other hand, there are stronger and steadier wind resources in offshore wind power plants which in turn lead to generate more power. Furthermore, this technology makes the installation of larger wind turbines possible due to that the limitations of the wind turbine installation are fewer [4, 7].

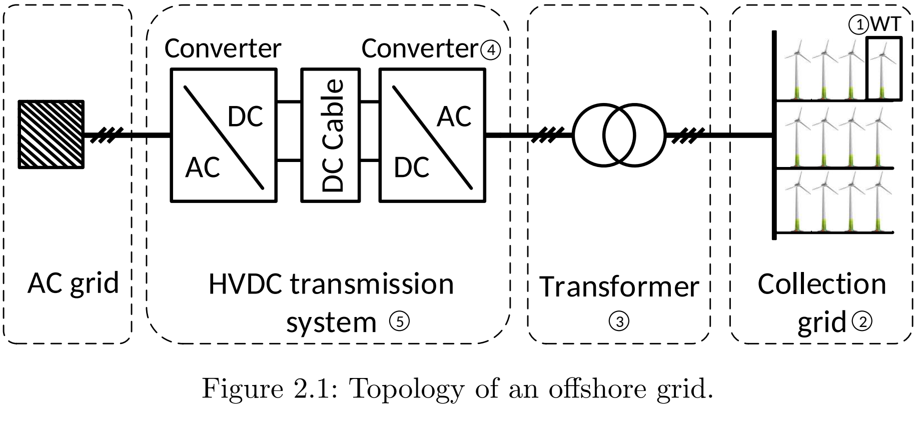

Figure 2.1: Topology of an offshore grid.

The structure of an offshore grid for a wind power plant, composed of Wind Turbines (WTs), an offshore collection grid, a power transformer, power converters, as well as a HVDC power transmission system for connection of offshore wind farm into onshore AC grid is described to better understand the roles of each of these components. Figure 2.1 depicts the topology of the offshore grid. In fact, this picture summarizes the offshore grids fundamental components whose modeling and control system will be studied in this thesis. First, the wind turbine components and technologies with variable-speed wind turbines ① are briefly summarized. Second, the possible layouts of offshore collection grid ② are presented. Here, an AC collection grid is presented for collecting the power generated by the wind turbines. Third, the focus is on transformer ③ which provides the voltage adaptation between the converter of the HVDC system and the collection grid. Fourth, a brief overview of Line Commutated Converter and Voltage Source Converter ④ is provided. In this section, the advantages of VSC over LCC are highlighted. The last section discusses two different types of HVDC transmission system ⑤ for connection of offshore wind farms to the AC power networks. It should be mentioned that this chapter has adopted the HVDC connection for offshore grid.

2.2 Wind turbine

All wind turbines operate in the way to extract the kinetic energy available in the wind and then, convert this energy into the electric power. In the past two decades, the development of the wind power capacity had an increasing trend. For example, a wind turbine had a power capacity of 300 kW in the 1980´s. A decade later, the wind turbine capacity had increased to 1500 kW. Nowadays, the biggest wind turbines for offshore wind farms can be built with an electric power capacity of more than 8 MW [4]. In the future, the wind turbine power capacity for offshore applications is expected to reach 20 MW [21]. The main parts of a wind turbine and its different topologies are studied in this section.

2.2.1 Wind turbine components

Nowadays, the majority of the modern large wind turbines mounted worldwide include the horizontal-axis turbines with three blade rotors. This section focuses on the details regarding the important elements inside wind turbine. Figure 2.2 demonstrates a typical design of this horizontal-axis wind turbine [4].

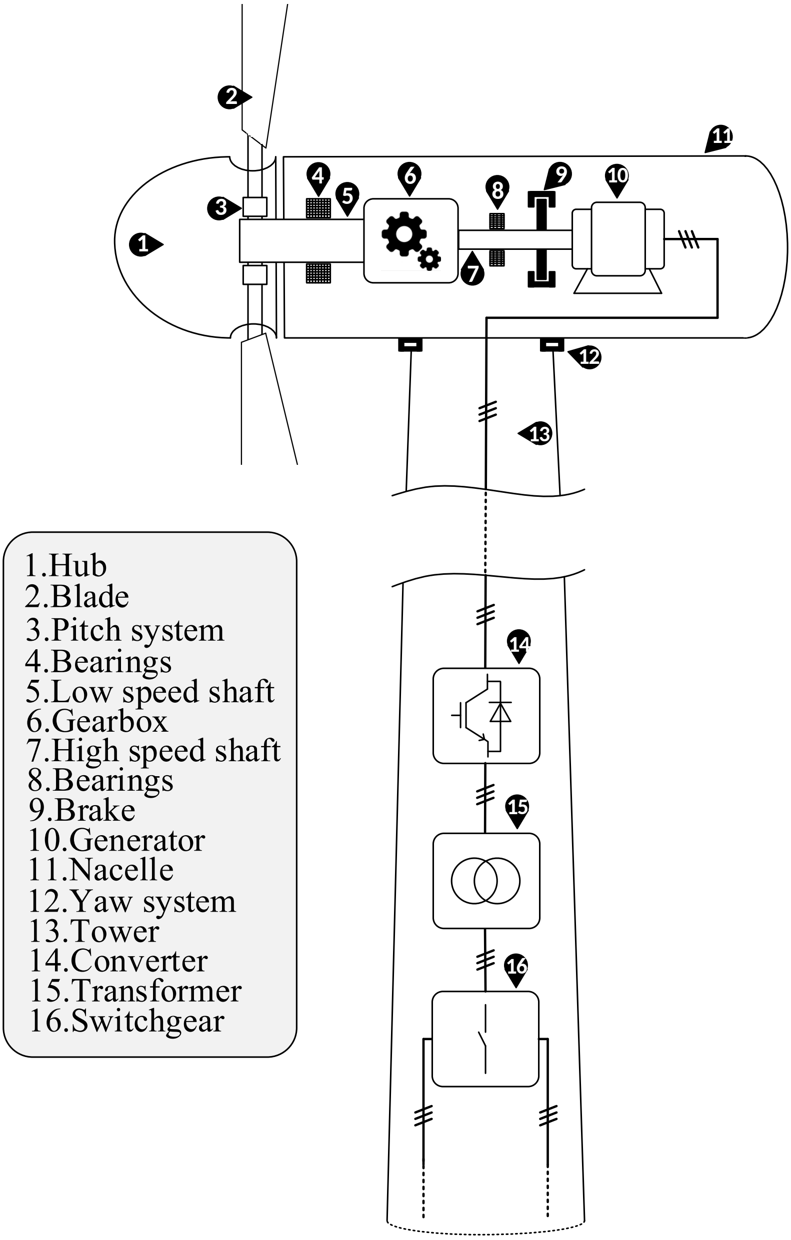

Figure 2.2: The basic elements of a horizontal-axis wind turbine.

The wind turbine system consists of a rotor which is usually incorporated into the hub, the blades and the mechanical shaft. The reason why the blades are mounted on the rotor hub through mechanical joints is to extract the wind energy. Using this shaft, the incoming power is transmitted into the generator. Moreover, a pitch mechanism which varies the angle of blades is located in the rotor hub and allows for the power captured from wind to be restricted. Thus, this action results in keeping the generator below its power margin. Furthermore, for the limitation of the generator speed during its function, mechanical brakes which are safety mechanisms are embedded [4]. A gearbox is commonly implemented in the wind turbines in order to adapt the radial rotating speed of the rotor hub to the high rotating speed of the machine rotor. This gearbox can be eliminated in some wind turbines depending on the generator type. In fact, when the generator can adjust the rotor speed to its electrical speed, the machine is connected to the turbine without the gearbox [4].

The wind turbine generators which are linked directly to the output shaft of the gearbox are employed to transform the mechanical energy into electrical energy. There are various types of these machines, including induction or synchronous generators. In addition, the power converters are designed in wind turbines to attain maximum efficiency and reliability. Thus, these converters can be interfaced with the stator or rotor terminals of generators dependent on the topology of turbine and the type of generator applied. Typically, the wind turbines contain a step-up transformer to match voltage level for interconnections [4].

In terms of distribution of components inside the wind turbine, the generator and gearbox are installed within the nacelle, whereas the other elements of the wind turbine such as the converter or the transformer can be housed either inside the tower or the nacelle [4].

Both the offshore and onshore wind turbines include the parts referred above, however their support layout is different. On the other hand, the offshore structure providing the support system of the wind turbine is based on a structure joined to the sea bed or relying on buoyancy or ballast methods, whilst onshore structures are mounted on a conventional concrete basement [4].

2.2.2 Wind turbine classification

The most significant wind turbine types are categorized in this chapter as fixed-speed wind turbine, limited-speed wind turbine, variable-speed with partial-scale converter and variable-speed with full-scale converter [4]. A brief description of each of these wind turbine technologies is presented here and the variable-speed wind turbine with full-scale converter has been selected to investigate the offshore grid for this thesis.

2.2.2.1 Fixed-speed wind turbine

Fixed-speed wind turbine was the most convenient type of these machines during 80s and 90s [4]. In this type of wind turbines, a three-bladed rotor is generally connected to a Squirrel Cage Induction Generator (SCIG) through a multiple-stage gearbox, as illustrated in Figure 2.3.

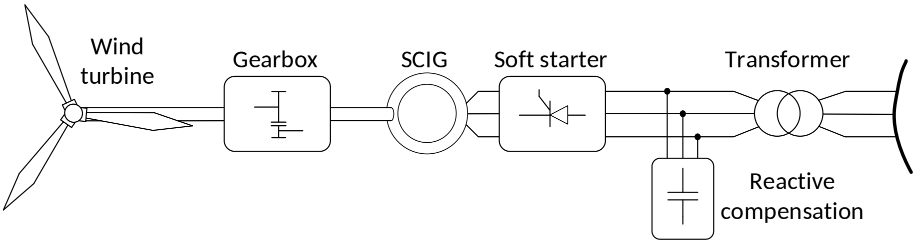

Figure 2.3: Fixed-speed wind turbine with SCIG generator.

Furthermore, the stator of the SCIG is directly coupled to the electrical network through a transformer. The applied SCIG makes the turbine work at constant speed [22].

During normal operating condition, capacitor banks are generally needed to establish reactive power support for SCIG, so as to be able to magnetize the generator. In addition, in order to avoid the inrush current during the machines start-up and connection to the AC grid, a thyristor-based soft-starter is employed in these wind turbines [4, 23]. Moreover, the passive or active stall and pitch systems are used to govern the aerodynamic power [22].

The significant benefits of this wind turbine technology include its robust structure, the relatively low costs of production and simple control [4]. However, the drawbacks are suboptimal energy extraction from the wind, requiring reactive power supply for the induction generators, fault ride-through requirement and high mechanical stress, which lead to the use of the other topologies [4].

2.2.2.2 Limited-speed wind turbine

The limited variable-speed wind turbine which typically includes a Wound Rotor Induction Generator (WRIG) with a variable rotor resistance was suggested during the 90s [4]. This technology can attain a limited range of speed variation using a variable resistance connected in series with the rotor winding of the generator. Thus, the speed can be changed with the variation of the resistor level [4]. Also, in order to control the reactive power and limit the aerodynamic power in such machine, the capacitor banks and pitch control are usually implemented [22].

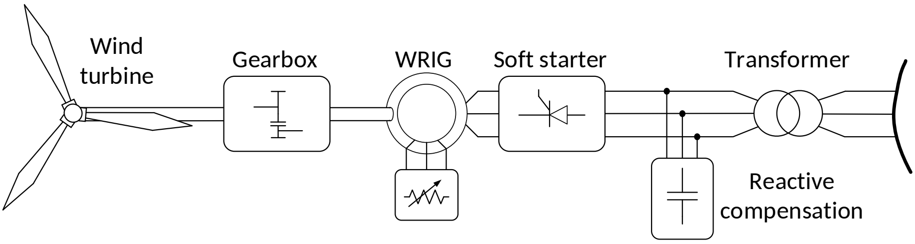

Figure 2.4: Limited variable-speed wind turbine with WRIG generator.

In general, this concept could remove the lack of variable speed with enhancement of the aerodynamic efficiency. However, these wind turbines have drawbacks similar to those of fixed-speed concept for the large turbines [4]. A sketch of this type of wind turbines is shown in Figure 2.4.

2.2.2.3 Variable-speed wind turbine with partial-scale converter

This category of wind turbines is used to increase the operational efficiency of wind turbines. These wind turbines are equipped with a WRIG generator in which the stator winding is directly linked to the AC network and the rotor winding is interfaced with the AC system via a partial-scale power converter. Therefore, the generator of the aforementioned wind turbine is introduced as a Doubly Fed Induction Generator (DFIG) due to the fact that both the rotor and the stator have the ability of power injection into the AC system [24]. Also, the power converter can independently regulate the real and reactive power in a wide speed range (typically from -40% to +30% [4]). This action in turn results in optimum wind energy capture. Hence, the application of this wind turbine type is very effective at sites in which wind oscillations are highly severe [24].
The partial-scale power converter consists of two back-to-back voltage source

converters connected through a DC link [24]. The converter at the grid side can be regulated to support the reactive power and also enhance the wind turbines fault ride-through capability [4]. Typical configuration of such a system is shown in Figure 2.5.

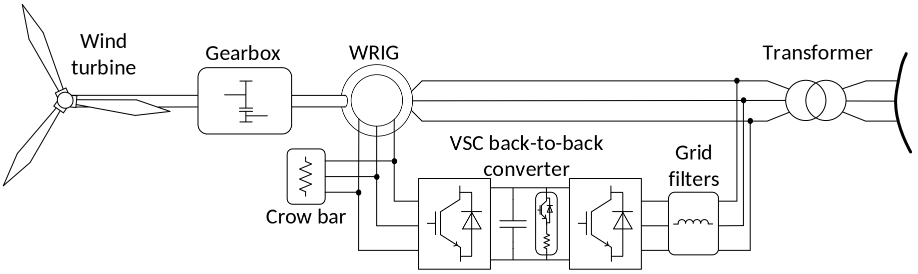

Figure 2.5: Variable-speed wind turbine with DFIG generator.

Nevertheless, this technology has various disadvantages. For instance, the presence of slip rings for power capture from the DFIGs rotor can result in generator operation failures [24, 25]. In addition, the direct connection of the generators stator into the grid can increase the complexity of managing an appropriate ride through operation under grid fault condition [24, 25].

2.2.2.4 Variable-speed wind turbine with full-scale converter

This type of wind turbines is capable of maximizing the power extracted from wind [4]. Thus, the generators of this concept operate at the variable speed in order to achieve this maximum power. There are different generator types for implementation in this wind turbine topology such as Permanent Magnet Synchronous Generator (PMSG), SCIG and Wound Rotor Synchronous

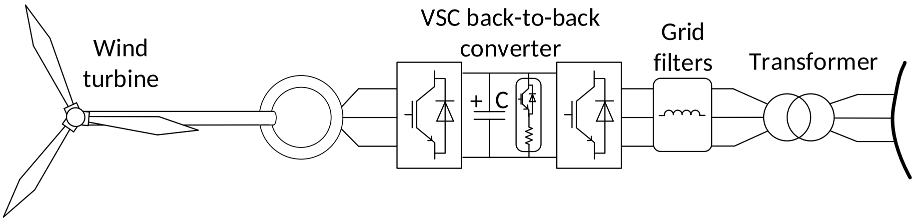

Figure 2.6: Variable-speed wind turbine with direct drive PMSG generator.

Generator (WRSG) [4, 26]. In this thesis, the variable-speed wind turbine with full power converter which includes a direct drive PMSG generator is studied. The configuration of this wind turbine type is depicted in Figure 2.6.

The synchronous generator of this wind turbine produces variable voltage/frequency due to its changeable operating speed [27]. Hence, this machine needs to be entirely decoupled from the constant-frequency AC grid. For this reason, the full power converters are used to link the stator of the generator with the AC network [27]. The application of these power converters allows for the connection between the rotor of the generators and the wind turbine to be done without a gearbox [24]. The power transmission into the grid, DC voltage control and grid voltage/frequency support [24] can be provided through an appropriate control system at the grid side converter. In addition, this converter enables the combination of ride-through techniques [4]. The DC link of the power converters is generally equipped with a DC chopper which allows to bypass excessive currents during the performance [4]. A pitch control system is usually applied to restrict aerodynamic speed during the fault.

2.3 Offshore collection grid layouts

The location of the wind turbines within an offshore wind farm will be specified according to the speed, direction and the turbulence intensity of the wind. Therefore, in order to maximize the wind power extraction, the layout of the offshore collection grid should be optimized considering the foregoing parameters.

A collection grid of AC offshore wind farms can be constructed based on three different connection layouts: radial, ring and star [25, 28, 29]. These designs are explained in detail in this section and the offshore wind farm grid with radial configuration is studied in this thesis.

2.3.1 Radial

The radial collection system rows the wind turbines inside one feeder in a string topology. Figure 2.7 depicts the radial collection scheme. In this configuration, two factors, the nominal power of machines and the capacity of cables, have an important impact on the determination of the maximum number of wind turbines that can be installed in one feeder.

Although this collection topology is the cheapest, the most straightforward and prevalent, it contains difficulties in terms of reliability. On the other hand, when a fault takes place in the interface cable between the first wind turbine and the hub of the feeder, the total power produced by the rest of the wind turbines in the feeder is wasted [4, 29, 30].

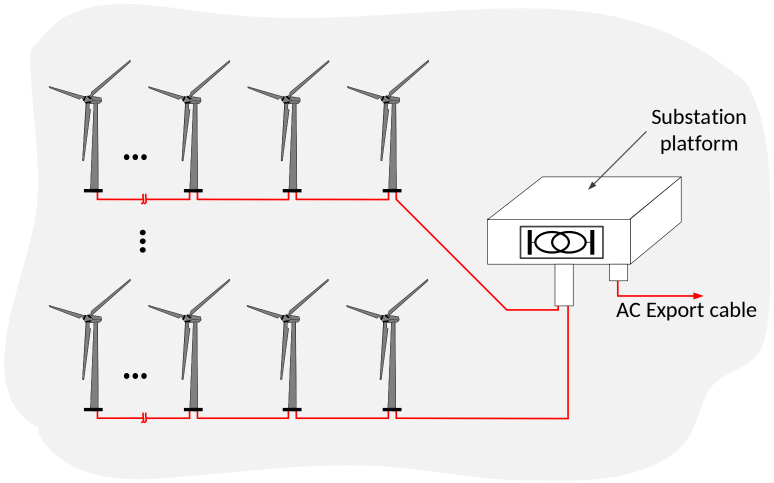

Figure 2.7: Scheme of the radial collection configuration.

2.3.2 Ring

The ring connection grid is achieved by improving the reliability of the radial configuration. Hence, this design is more expensive than the radial collection system. The ring collection system can be also classified based on how the formation of ring. Thus, single-sided, double-sided and multi-ring are three possible ring schemes. In all ring topologies, extra cables are joined to provide redundant paths for the power flow in a feeder. Therefore, in a single-sided ring scheme, the outermost wind turbine within the feeder is interfaced with the collector hub through an interface cable, whilst in the double-sided configuration, the redundant cable couples two feeders in parallel together [4, 30, 31]. The schematics of two ring designs are shown in Figures 2.8 and 2.9. The main disadvantage of the double-sided system is the oversizing of some cables for the bidirectional power flow in the cable fault mode [4].

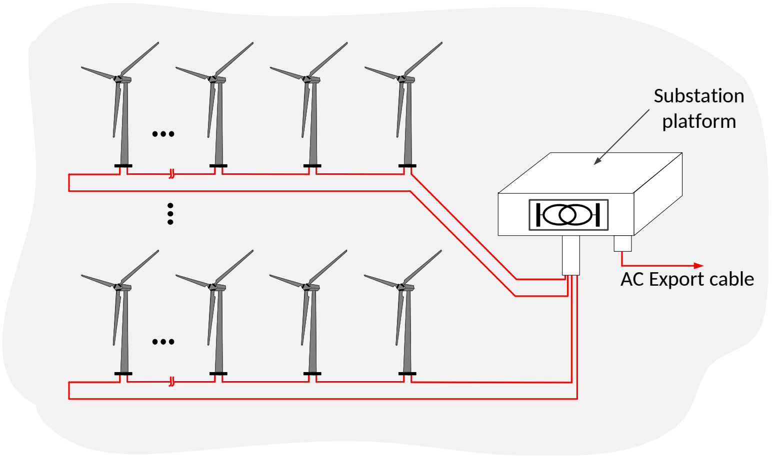

Figure 2.8: Representation of single-sided ring collection configuration.

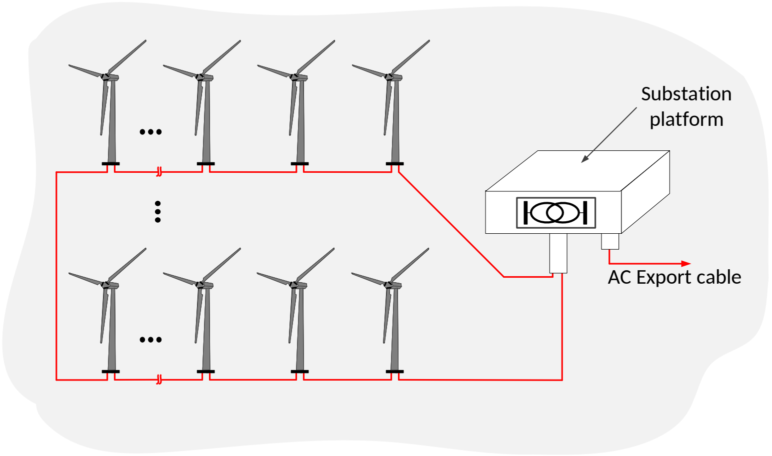

Figure 2.9: Representation of double-sided ring collection configuration.

2.3.3 Star

Using the star topology, the rating of cables joining the wind turbines and collector point can be attenuated and the reliability of the system can be improved. Thus, the common connection point is generally positioned in the middle of all wind turbines situation. Figure 2.10 illustrates the star collection configuration.

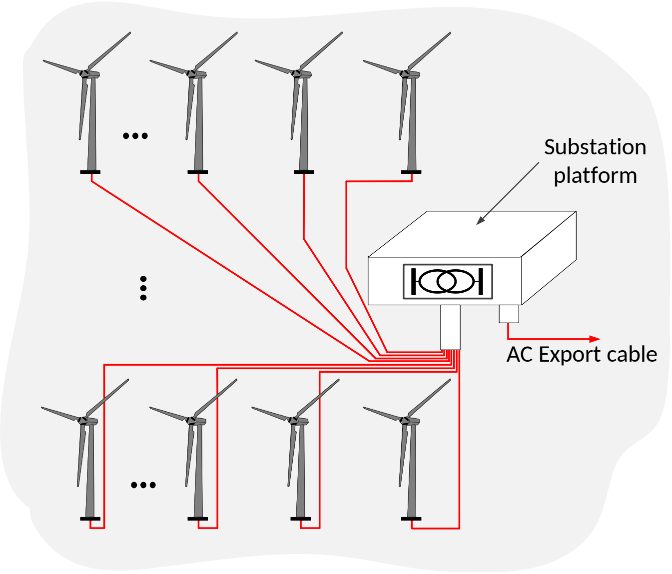

Figure 2.10: Star collection configuration.

In the case of a cable failure, only one wind turbine will be lost and thus, the reliability of the system is enhanced. Therefore, this can be regarded as an advantage of the star design. Nevertheless, the high cost and the losses of cables are its drawbacks which are due to the longer lengths of cables and the application of lower voltage ratings for coupling wind turbines in this system [30, 31, 32].

2.4 Power transformer

The operation of power transformers settled in offshore substations is to match the voltage of the offshore collection grid and of the offshore converter of HVDC grid. In fact, these transformers, increase the voltage level of the inner-array cable (typically from 10-36 kV to 110-200 kV), so as to minimize the electrical losses associated to the export cable [33]. In addition, the voltage control can be achieved by alternating the transformer winding ratio (transformer tap changer).
The design of offshore transformers is virtually similar to the one of the transformers used in onshore AC networks. The difference between them is that the aim of minimizing the maintenance and harmful effects of the marine surroundings are considered in the offshore transformer design. For

instance, corrosion matters are taken into account in order to ensure the protection of the offshore environment. Transformers are commonly constructed with copper windings wrapped around laminated iron cores. To cool the system, these parts of the offshore transformer are digged into the oil [4, 33].

2.5 Converter

The power converter is one of the most important components required for the HVDC system of an offshore grid. It has the ability of converting electrical energy from AC into DC or vice versa. Generally, there are two different types of configuration for converters used in HVDC grids. This classification is determined based on the converter operation principles. Therefore, the topology that requires an AC system to operate is called Line Commutated Converter (LCC) and further topology which is self-commutated employs Voltage Source Converter (VSC). The utilization of VSC in high voltage DC systems of offshore grids is prevalent. The reason for this is that the proper operating facilities for offshore systems such as black-start capability and independent active and reactive power regulation can be provided by means of this technology [15]. This section will present a brief description of VSC converters in offshore grids as well as of the LCC converters used in the HVDC transmission systems.

2.5.1 Line Commutated Converter

The construction of a Line Commutated Converter (LCC) is based on the implementation of the thyristor switches in Current Source Converters (C-SCs) configuration [4]. The thyristors which are bistable switches can be triggered with a gate pulse once in a half cycle [34]. However, the switching-off of these switching devices will take place when the current passes through the zero [4]. Thereby, this causes to restrict the controlling ability of LCC converters [21]. As such, LCCs need a relatively powerful AC voltage source for the commutation of the thyristors [35]. This technology is facing to lack of black start capability and therefore, it requires an auxiliary start-up system in offshore wind power plants or in very weak grids [36].
However, LCC is a mature technology which enables efficiency, reliable and cost-effective power transmission for multiple utilizations. Hence, it can be employed for transferring power over several hundreds of MW [37]. Moreover, LCCs are capable of withstanding short-circuits, since DC inductors have the capability of the current limitation under fault condition [38]. In

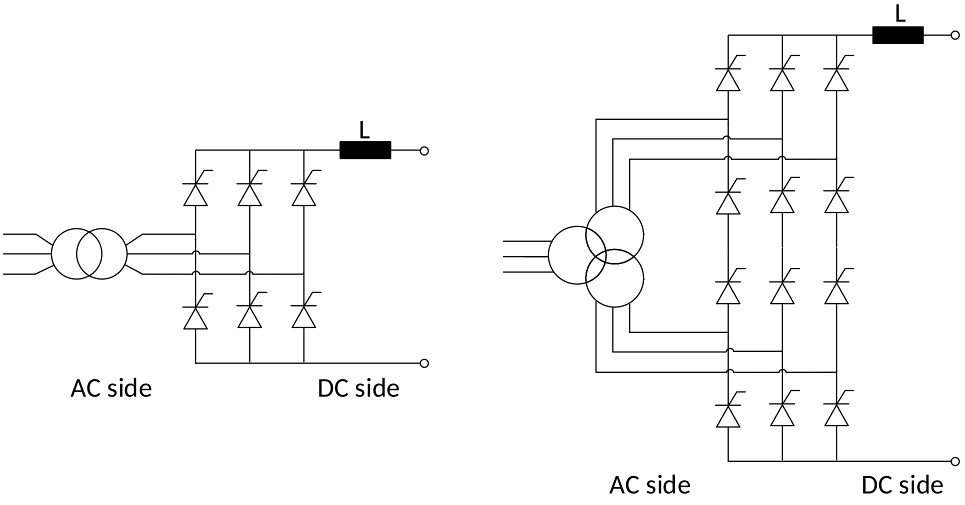

(a) 6-pulse (b) 12-pulse

Figure 2.11: Line commutated converter topology.

addition, this thyristor-based technology renders small number of switchings so that low switching losses can be resulted [21].

The basic building block utilized for LCC converters is a 6-pulse bridge in which six thyristor valves are placed. These thyristor type valves of LCC converter have to fulfill the functions as: conducting high current (up to 5 kA), blocking high voltage (up to 8.5 kV), governing the DC voltage through the firing angle, connecting AC and DC sides and transmitting at higher voltage levels [4, 21]. As such, the power transmission by means of LCC can be performed up to 7200 MW at a DC voltage level of ±800 kV, whereas the VSC is able to transfer up to 1000 MW at ±320 kV [21].

Furthermore, various thyristors are usually connected in series to ensure the achievement of desired high voltages. Therefore, in case of a single thyristor failure, the whole HVDC circuit is not disabled. As a consequence, the redundancy can be foreseen. Most of the classical HVDC topologies employ 12-pulse LCCs in order to cancel the harmonics with orders of 5,7,17,etc [4].

The commutation of line-commutated converters is based on the current transmission from one branch of the converter to another which takes place thanks to a synchronized firing sequence of the thyristor valves. The commutation normally acts with AC system voltage source. Therefore, the short-circuit capacity of the AC system needed for LCC commutation is almost twice the rating of the converter [35]. Figure 2.11 shows the scheme of the

6-pulse and 12-pulse series LCC converters.

2.5.2 Voltage Source Converter

Self-commutated voltage source converters are developed on the basis of power electronic devices. The switching elements in VSCs are Insulated Gate Bipolar Transistors (IGBT) which contains the controllability characteristic of MOSFET and also feature of the BJT reliability [4]. Therefore, these devices do not commutate with frequency in the AC network. Thus, the risk of commutation failure can be eliminated,since an AC grid is not required. The operation of turning-off and turning-on in IGBTs allows for greater controllability and switching symmetry than the LCCs, which leads to a quicker power flow control. The VSC technology enables controlling active and reactive power independently so that the need for costly reactive power compensators is removed [4]. Another feature of VSC is the decrease in the generation of harmonics thanks to a larger number of switching operations [21]. Also, the short-circuit capacity control of AC grid is not required in this technology [4]. An additional advantage is its black start capability. The converter topologies in VSC-HVDC are commonly divided into three groups: two-level converter, three-level converter and Modular Multilevel Converter (MMC). A VSC converter allows for the generation of a sinusoidal AC voltage from a constant DC voltage in an inverter mode and it can carry out the inverse process of this conversion in a rectifier mode. Hence, the utilization of a Pulse Width Modulation (PWM) technique is efficient for the switching of the IGBTs. The reason for this is that the PWM makes the switching devices produce an almost sinusoidal wave at a certain frequency [4]. Figure 2.12 shows the scheme of a two-level voltage source converter.

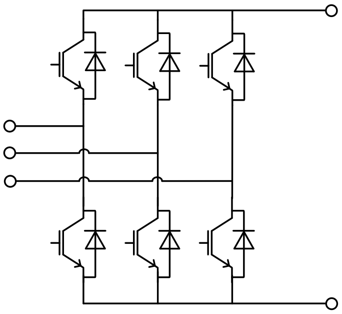

Figure 2.12: Scheme of a 2-level 3-phase VSC.

Focusing on the higher level VSC converters, the harmonic distortions of the output voltage as well as the number of switchings can be reduced through these technologies. Therefore, power losses associated with the switching can be significantly reduced with this topology, compared to the VSC-HVDC systems including two-level converters [4].
Modular Multilevel Converter topology was suggested by Prof. Rainer Marquardt in 2003 and worlds first implementation of this concept was in the Trans Bay Cable project [4]. In this project, two converter stations interconnected together through a transmission line with a voltage level of 200 kV and a length of 88 km were equipped with MMC converters of 400 MW [4].
Multilevel converters are constructed via a series connection of multiple sub-modules in order to maximize the output voltage level of the converter [21]. This concept can be built according to two different configurations which are half-bridge and full-bridge.
In MMC topologies, each module includes the semiconductor switches and a DC capacitor independently. For this reason, this technology has a considerable advantage compared to the two-level and three-level VSC concepts, which is the inexistence of a connection of the common capacitor in the converters DC link [21]. This renders the MMC suitable for applications of high-power and high voltage.
The benefits of MMC concept are small switching losses and a low level of HF-noise in comparison with two-level converter topology, which in turn are related to the low switching frequency[4].
Furthermore, the switching operation of modules in MMC allows for the formation of multiple small voltage steps in order to create step-wise AC waveforms of the output voltage [4]. Therefore, the large voltage steps corresponding to the PWM operation can be diminished by using this concept. Figures 2.13 and 2.14 show the schematics of the MMC with topologies of half-bridge and full-bridge modules, respectively.

2.6 HVDC grid for offshore wind power transmission and applied topologies

To transfer offshore wind power, HVDC grids in which one or multiple large-scale offshore wind power plants are integrated into onshore electric power systems are applied. Offshore HVDC links can be divided into two main configurations depending on the locations of wind farms and onshore AC substations, flexibility, redundancy and reliability of power transmission and

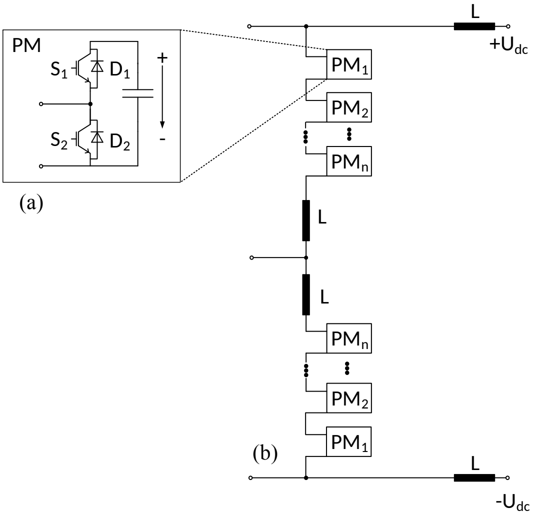

Figure 2.13: Schematic of a half-bridge module and a cascaded configuration.

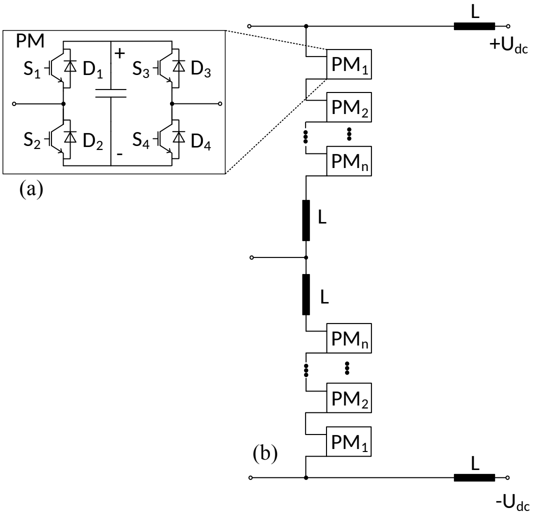

Figure 2.14: Schematic of a full-bridge module and a cascaded configuration.

eventual costs of transmission cables and devices [4], which can be point-to-point (PPT) and multi-terminal HVDC links. The foregoing topologies are discussed below in greater detail.

2.6.1 Point-to-point HVDC topology

Point-To-Point (PPT) HVDC grids are the simplest HVDC configuration to connect a single offshore wind farm with a shore AC network. This type of connection includes two power converters and DC lines. The first PPT-HVDC grid for transmitting offshore wind power to the shore grid is the project of BorWin1. This HVDC connection system is used to link the wind farm of BARD offshore 1 located in the North Sea to the German onshore AC network [21]. Figure 2.15 illustrates a scheme of point-to-point HVDC grid.

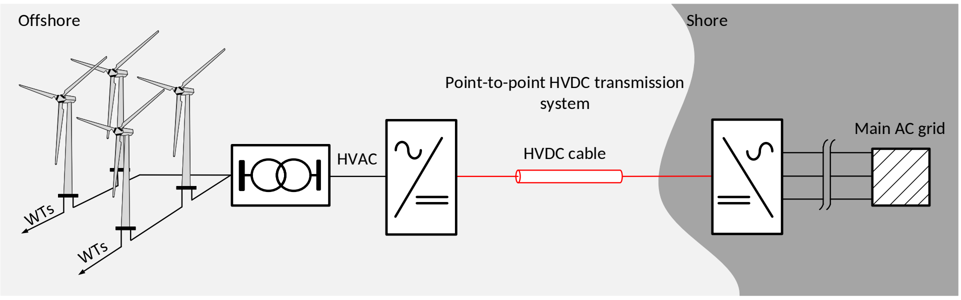

Figure 2.15: Offshore wind power transmission through point-to-point HVDC topology.

In case of fault occurrence in the converter or HVDC circuit, the redundancy in the DC system cannot be foreseen, so that this causes the loss of the wind farm coupled to the faulted link [4]. Also, there is no flexibility in point-to-point grids.

2.6.2 Multi-terminal HVDC topology

The multi-terminal HVDC topology is used for power transmission of several offshore wind farms to the onshore AC grids. This configuration provides sufficient redundancy within the HVDC systems and thus, it improves the reliability of power transmission. Figure 2.16 shows a general scheme of this HVDC grid consisting of various HVDC circuits and converter stations. The worlds first multi-terminal flexible HVDC project constructed in China by the local network operator China Southern Power Grid (CSG), has three terminal ±160 kV HVDC transmission networks. The capacity of this multi-terminal VSC-HVDC project called Nanao is 200 MW [21].
There are different configurations of multi-terminal HVDC grids depending

on the number and capacity of HVDC links, maximum loss of power, flexibility, redundancy, number of HVDC circuit breakers and fast communications [15, 4].

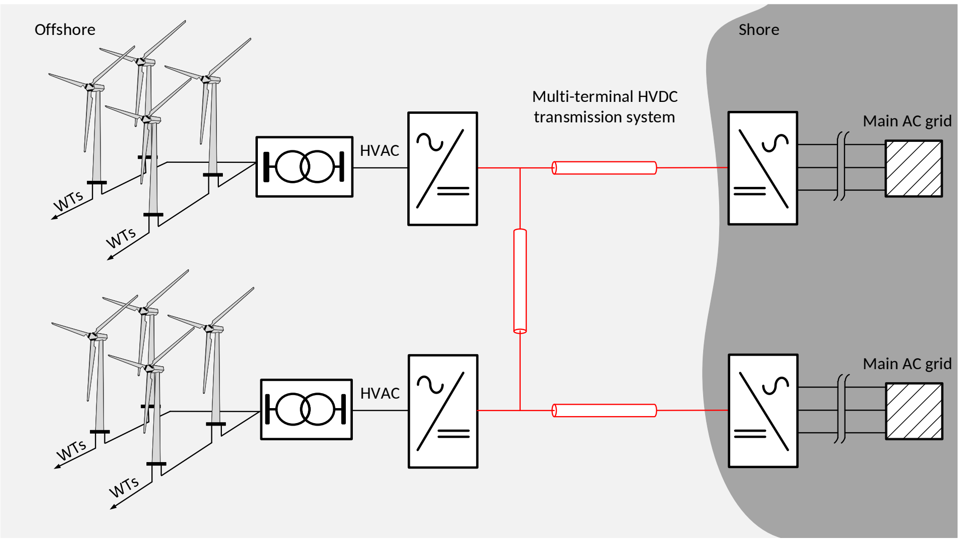

Figure 2.16: Offshore wind power transmission through multi-terminal HVDC topology.

These topologies are the General Ring Topology (GRT), the Star Topology (ST), the Star with a General Ring Topology (SGRT), the Wind farm Ring Topology (WFRT) and the Substations Ring Topology (SSRT) [4].
The common feature of all multi-terminal HVDC grid configurations is flexibility, since the bidirectional power flow is possible in case of failure in these grids. However, some differences can be found between these configurations such as [4]:

- The implementation of ST and SGRT topologies with an offshore platform.
- The requirement for fast communication in the GRT, WFRT and SSRT topologies to attune the protection devices.
- The need for a number of HVDC circuit breakers equal to the number of wind farms or AC grids for WFRT and SSRT topologies and a number of circuit breakers equal to the total number of wind farms and onshore AC substations for GRT, ST and SGRT configurations.

2.7 Summary

This chapter has introduced the offshore grid structure to be implemented in different scenarios such as inrush current reduction of transformers available in offshore systems during start-up and integration of offshore wind farms or during system restoration after fault clearance. Hence, all the main components of the abovementioned grid have been described in detail in order to enable us to better understand and analyze these scenarios.

Chapter 3

VSC converter modeling and control

To analyze the HVDC converter behavior in the offshore grids, modeling of the voltage source converter, modeling of the AC and DC grids of the converter as well as different control systems of converters have been studied.

3.1 Introduction

The VSC-HVDC transmission technology is used in offshore grids to connect the offshore wind farms to the main AC grids. The VSC converter of high voltage DC systems plays a significant role in transferring the power within the offshore grid. Therefore, in order to better understand the dynamic characteristics of converters, an averaged model of power converter is presented. In addition, different representations of AC and DC grids of converters are included. Based on these models, several control schemes of the power converter are introduced in order to ensure the optimal converter performance and stability of HVDC systems under various conditions. Control structures of converters are designed on the basis of a basic vector control strategy including a voltage control loop and an AC current control loop. The design of these controllers is accomplished based on the dynamic equations of the power converter as well as the applications of the control system.
This chapter is organized as follows: an averaged model is described in Section 3.2. In Section 3.3, models of AC grid coupling filters including inductive coupling filter and inductive-capacitive filter are presented. Section 3.4 discusses the modeling of DC grids for back-to-back, point-to-point and multi-terminal configurations. Thereafter, the inner and outer control loops and a Phase Locked Loop (PLL) method to synchronize the system with the AC grid are analyzed in Section 3.5. Finally, a study of the converter control systems under the fault condition is presented in Section 3.6. It should be mentioned that all the information of this chapter is referred to [39, 40].

3.2 Average model of a VSC converter

To scheme the VSC converter control strategies and analyze the HVDC system, an average model of the power converter is considered. This simplified equivalent representation that shows the average dynamic behavior of a converter at low-frequencies is achieved by decoupling the converter AC and DC sections as shown in Figure 3.1.

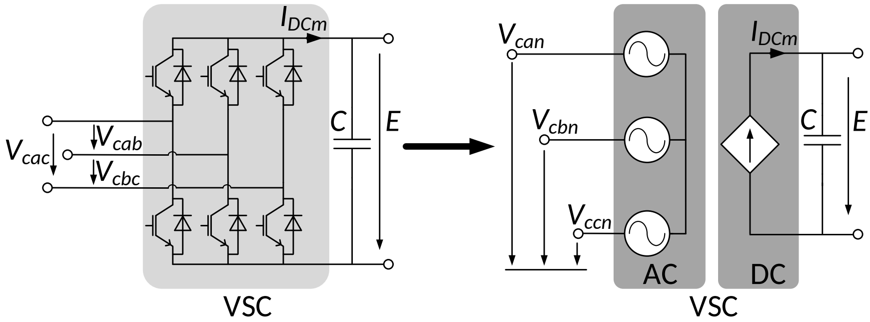

Figure 3.1: Average equivalent circuit of a two-level VSC converter.

In this average model, the converter AC side is represented by three AC voltage sources, whereas the converter DC side is modeled as a controllable current source. By neglecting losses in the voltage source converter, the active power on the AC side becomes identical to the power exchanged at the converter DC side [41, 42] i.e.

$$P_{AC} = P_{DC} = EI_{DCm} \tag{3.1}$$

and therefore, the DC current of the source can be calculated based on the power balance at the AC and DC side of the converter, i.e. [39]

$$I_{DCm} = \frac{P_{AC}}{E} \tag{3.2}$$

where P_{AC} is the active power at the AC side, P_{DC} is the power at the DC side of the converter, E is the DC side voltage and I_{DCm} is the current injected in the DC side of the converter.

3.3 Models of AC grid coupling filter

To decrease high-frequency harmonics in AC current, limit short-circuit currents, avoid variations of the current polarity in IGBT and independently control the active and reactive powers by regulating the current [43], an AC coupling filter between the AC grid and the AC side of the VSC converter is needed. For HVDC applications, the most common filters are inductance filters (L). However, inductance and capacitor filters (LC) are used for voltage regulation when the converter is interfaced with an offshore grid including offshore load or offshore wind farm. The models of AC coupling filters are described in the following subsections.

3.3.1 Inductive coupling filter (L)

The L filter allows for the connection of the VSC converter to the AC grid. The schematic diagram of the VSC connection to the AC system by means of a L filter is sketched in Figure 3.2.

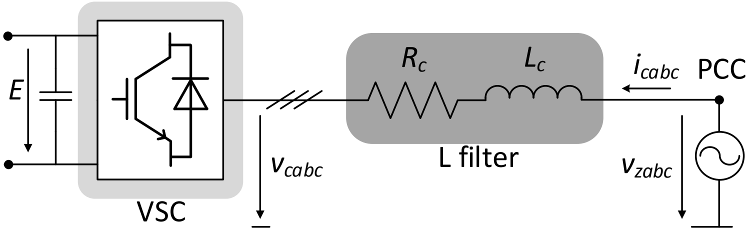

Figure 3.2: Model of the VSC converter connection to the AC grid through a L coupling filter.

According to the average model of the VSC converter, as illustrated in Figure 3.1, and assuming a balanced three-phase grid, differential equations at the AC side of the VSC converter under the stationary frame can be described as

$$\begin{cases} L_c\frac{di_{ca}}{dt} = v_{za} - v_{ca} - R_c i_{ca} \\ \\ L_c\frac{di_{cb}}{dt} = v_{zb} - v_{cb} - R_c i_{cb} \\ \\ L_c\frac{di_{cc}}{dt} = v_{zc} - v_{cc} - R_c i_{cc} \end{cases} \tag{3.3}$$

where v_{zabc} denotes three-phase voltages at Point of Common Coupling (PCC), v_{cabc} is three-phase converter voltages at AC side, i_{cabc} represents three-phase AC currents flowing into the converter through the L coupling filter and $(R_c + j\omega L_c)$ is the resistance and reactance of the coupling inductance between the converter and the PCC.
Using Park transformation, Equation (3.3) can be transformed into the qd synchronous reference frame, as follows.

$$\begin{cases} L_c \frac{di_{cq}}{dt} = v_{zq} - v_{cq} - R_c i_{cq} - \omega L_c i_{cd} \\ L_c \frac{di_{cd}}{dt} = v_{zd} - v_{cd} - R_c i_{cd} + \omega L_c i_{cq} \end{cases} \tag{3.4}$$

where ω is the angular frequency of the grid, v_{zqd} , v_{cqd} and i_{cqd} show qd-axis components of the PCC voltage, converter voltage and the AC current, respectively.

3.3.2 Inductive-capacitive coupling filter (LC)

The LC filter controls the amplitude and frequency of the offshore grid voltage in case of disturbances in the offshore grid current. The LC filter which consists of a series RL branch ($R_c + j\omega L_c$) and a shunt capacitor $(j\omega X_{c_f})$ connects the VSC AC side terminal to the offshore grid (offshore load or wind farm). The implementation of C_f at the PCC provides a low-impedance path to switch current harmonics generated by the VSC converter in order to prevent them from penetrating into the offshore grid. The model of a VSC converter connected to the offshore load by means of an inductance and capacitor filter (LC) is depicted in Figure 3.3.

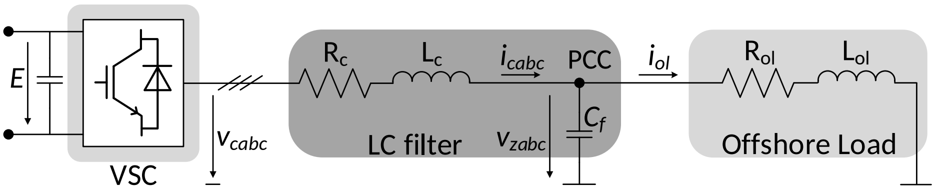

Figure 3.3: Model of the converter connection to the offshore load through a LC coupling filter.

Using the qd synchronous frame transformation, the mathematical model of

Figure 3.3 can be expressed as:

$$L_c \frac{di_{cq}}{dt} = v_{cq} - v_{zq} - R_c i_{cq} - \omega L_c i_{cd} \tag{3.5}$$

$$L_c \frac{di_{cd}}{dt} = v_{cd} - v_{zd} - R_c i_{cd} + \omega L_c i_{cq} \tag{3.6}$$

where ω is the nominal frequency of the power system, i_{cqd} is qd-axis components of the AC current flowing from the converter to the PCC, v_{zqd} refers to the voltages at the PCC and v_{cqd} are the voltages applied by the converter in the synchronous reference frame.

Also, according to state-space equations, dynamics of offshore load voltage in qd synchronous frame can be defined as follows

$$C_f \frac{dv_{zq}}{dt} = \omega C_f v_{zd} + i_{cq} - i_{olq} \tag{3.7}$$

$$C_f \frac{dv_{zd}}{dt} = -\omega C_f v_{zq} + i_{cd} - i_{old} \tag{3.8}$$

where i_{olqd} indicates the currents flowing through the offshore load $(R_{ol} + j\omega L_{ol})$ in qd synchronous frame. Moreover, the dynamic model of the offshore load composed of a series RL branch is written as

$$L_{ol} \frac{di_{olq}}{dt} = v_{zq} - R_{ol} i_{olq} - \omega L_{ol} i_{old} \tag{3.9}$$

$$L_{ol} \frac{di_{old}}{dt} = v_{zd} - R_{ol} i_{old} + \omega L_{ol} i_{olq} \tag{3.10}$$

where R_{ol} and L_{ol} are the resistance and inductance of the offshore load.

3.4 DC grid Modeling

The classification of the DC grids that exist among the converter stations of HVDC transmission systems is established on the basis of the situation and operation of the converter stations. Thus, DC grid configurations can be divided into three main groups: back-to-back, point-to-point and multi-terminal grids.

The cables in the DC grid connecting two or more converter stations are represented by π-equivalent circuits in which the capacitor at each terminal is equal to the summation of the whole capacitors joined in parallel at that end [44].

3.4.1 Back-to-back grid model

The HVDC back-to-back structure is a common configuration used to connect two asynchronous AC systems, operating at various frequencies, through a DC grid. Two VSC converters of this configuration are located at the same station and thus, there is no transmission of power with a DC grid over a long distance. The schematic diagram of a back-to-back system is shown in Figure 3.4.

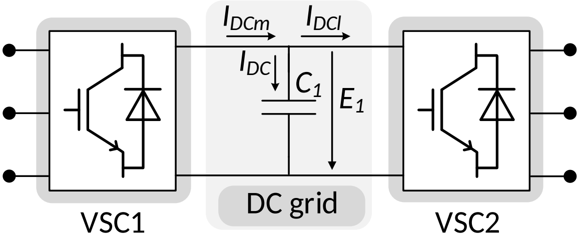

Figure 3.4: Back-to-back converter DC grid model.

applying the Kirchhoffs laws to analyze the DC circuit, the following expressions are obtained

$$I_{DC} = I_{DCm} - I_{DCl} \tag{3.11}$$

$$\frac{dE_1}{dt} = \frac{1}{C_1} I_{DC} \tag{3.12}$$

where E_1 is the DC voltage, C_1 is the capacity of DC capacitor, I_{DCm} is the current coming from the DC side of VSC1, I_{DC} is the current flowing through the DC bus capacitor and I_{DCl} is the current flowing through the DC side of VSC2.

Substituting for I_{DC} in Equation (3.12), based on Equation (3.11), the derivative of the DC voltage can be expressed as a function of the current from both converters as:

$$\frac{dE_1}{dt} = \frac{1}{C_1}(I_{DCm} - I_{DCl}) \tag{3.13}$$

3.4.2 Point-to-point grid model

The point-to-point system is used to connect two AC systems like an offshore wind farm and an onshore AC grid. This type of system is composed of two converter stations that are interfaced by means of a DC transmission line (cable or overhead line). The typical schematic of the point-to-point system is depicted in Figure 3.5.

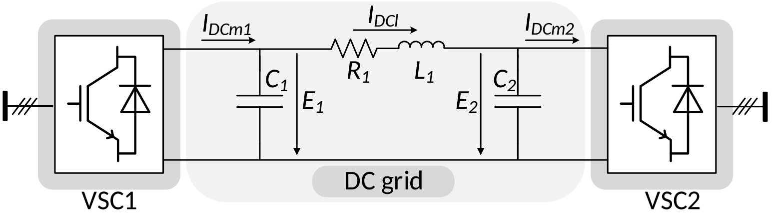

Figure 3.5: The point-to-point system representation for a DC grid analysis.

The DC link differential equations describing the dynamic behavior of the point-to-point HVDC grid can be expressed as follows

$$\frac{dE_1}{dt} = \frac{1}{C_1}(I_{DCm1} - I_{DCl}) \tag{3.14}$$

$$\frac{dE_2}{dt} = \frac{1}{C_2}(I_{DCl} - I_{DCm2}) \tag{3.15}$$

$$\frac{dI_{DCl}}{dt} = \frac{1}{L_1}(E_1 - E_2 - R_1 I_{DCl}) \tag{3.16}$$

where E_1 and E_2 are the voltages of equivalent capacitors, C_1 and C_2 are the equivalent capacitances at both sides of the DC grid, I_{DCm1} and I_{DCm2} are the currents flowing through the converters, I_{DCl} is the current flowing through the DC cable and R_1 and L_1 are the resistance and inductance of the DC cable.

3.4.3 Multi-terminal grid model (three-terminal)

The multi-terminal HVDC configuration contains more than two HVDC converter stations which are geographically separated and linked through DC transmission lines. The scheme of a three-terminal grid, studied in this thesis, is depicted in Figure 3.6.

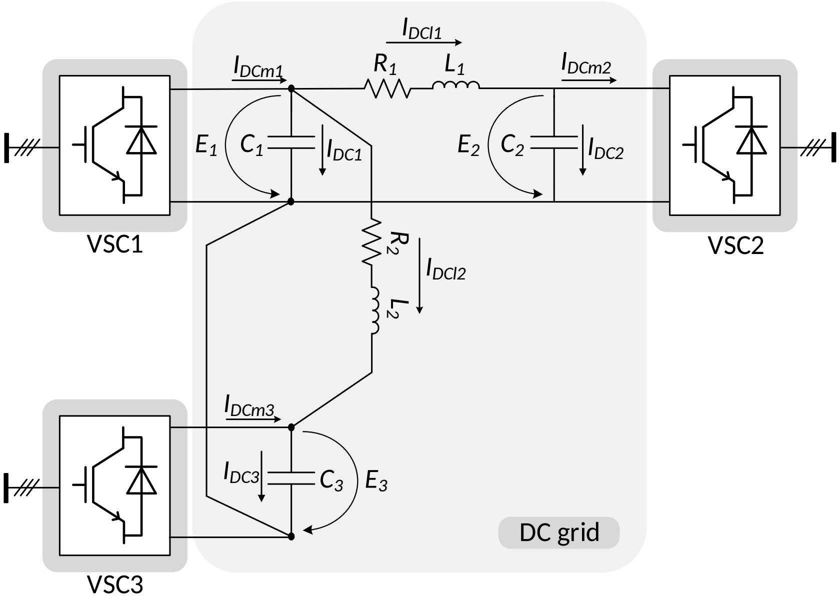

Figure 3.6: Three-terminal DC grid model.

The differential relations of the three-terminal grid shown in Figure 3.6 can be obtained based on circuit laws, as

$$\frac{dE_1}{dt} = \frac{1}{C_1} I_{DC1} \tag{3.17}$$

$$\frac{dE_2}{dt} = \frac{1}{C_2} I_{DC2} \tag{3.18}$$

$$\frac{dE_3}{dt} = \frac{1}{C_3} I_{DC3}, \tag{3.19}$$

$$\frac{dI_{DCl1}}{dt} = \frac{1}{L_1}(E_1 - E_2 - R_1 I_{DCl1}) \tag{3.20}$$

$$\frac{dI_{DCl2}}{dt} = \frac{1}{L_2}(E_1 - E_3 - R_2 I_{DCl2}) \tag{3.21}$$

and also, the following expressions

$$I_{DC1} = I_{DCm1} - I_{DCl1} - I_{DCl2} \tag{3.22}$$

$$I_{DC2} = I_{DCl1} - I_{DCm2} \tag{3.23}$$

$$I_{DC3} = I_{DCl2} + I_{DCm3} \tag{3.24}$$

Substituting for Equations (3.22) to (3.24) in (3.17) to (3.19) and reorganizing the differential equations of the DC grid, the state-space representation can be obtained in the following form.

$$\frac{dx_{3t}}{dt} = A_{3t}x_{3t} + B_{3t}u_{3t} \tag{3.25}$$

For the three-terminal grid, the state vector (x) including the currents in the inductors and the voltages in the capacitors and the input vector (u) are characterized

$$x_{3t} = \begin{bmatrix} E_1 & E_2 & E_3 & I_{DCl1} & I_{DCl2} \end{bmatrix}^T \tag{3.26}$$

$$u_{3t} = \begin{bmatrix} I_{DCm1} & I_{DCm2} & I_{DCm3} \end{bmatrix}^T \tag{3.27}$$

and the matrices in the state-space model are defined as

$$A_{3t} = \begin{bmatrix} 0 & 0 & 0 & \frac{-1}{C_1} & \frac{-1}{C_1} \\ 0 & 0 & 0 & \frac{1}{C_2} & 0 \\ 0 & 0 & 0 & 0 & \frac{1}{C_3} \\ \frac{1}{L_1} & \frac{-1}{L_1} & 0 & \frac{-R_1}{L_1} & 0 \\ \frac{1}{L_2} & 0 & \frac{-1}{L_2} & 0 & \frac{-R_2}{L_2} \end{bmatrix} \tag{3.28}$$

$$B_{3t} = \begin{bmatrix} \frac{1}{C_1} & 0 & 0 \\ 0 & \frac{-1}{C_2} & 0 \\ 0 & 0 & \frac{1}{C_3} \\ 0 & 0 & 0 \\ 0 & 0 & 0 \end{bmatrix} \tag{3.29}$$

3.5 Converter control design

The control strategy implemented in the converters of this thesis is based on the classic vector control [45, 46, 47]. The aforementioned control system enables controlling the active and reactive powers independently as well as limiting current. This control strategy can be classified in two groups: lower level controller and higher level controller. The lower level controller known as current control loop or inner loop is responsible for regulating the q- and d-axis components of the AC current. Moreover, the higher level controller named as voltage control loop or outer loop is used for the production of the current reference components, i^*_{cq} and i^*_{cd}, in order to inject to the inner loop. Depending on the HVDC converter application in the thesis, the outer loop is determined on the basis of the DC and AC voltage control systems. Namely,

- The DC voltage control scheme is employed for converters linking the DC systems to the main AC networks. The DC voltage controller governs the HVDC grid voltage to ensure power balance and DC system stability. Thus, in applications in which i^*_{cq} is provided by the DC voltage controller, the other current component, i^*_{cd}, results from an AC voltage controller in order to be capable of regulating AC voltage at the PCC.

- When the power converter is connected to offshore wind farm, the AC voltage controller is applied to the converter in order to generate a stable voltage at the AC busbar of the offshore wind farm platform. Therefore, the goal of this control system in this case is to provide both current components of the converter, i^*_{cqd} for inner control loop. The fact is that the AC voltage control system is the sole controller available in outer loop.

A detailed description of the inner and the outer controllers is presented in the next subsections. Note that the control systems based on the vector control method are designed in the synchronous reference frame, defined by the grid angle obtained through a Phase Locked Loop (PLL) system. For this reason, the currents and voltages measured at the AC side are transformed into q-and d-components through park transformation.

3.5.1 Converter current control (Inner loop)

The inner current control based on vector control strategy is designed to track the current references obtained by the outer controller in a defined time and to generate voltage references for injecting to the VSC converter. Therefore, the systems active and reactive powers can be independently controlled under these circumstances. Figure 3.7 shows the structure of this inner loop controller.

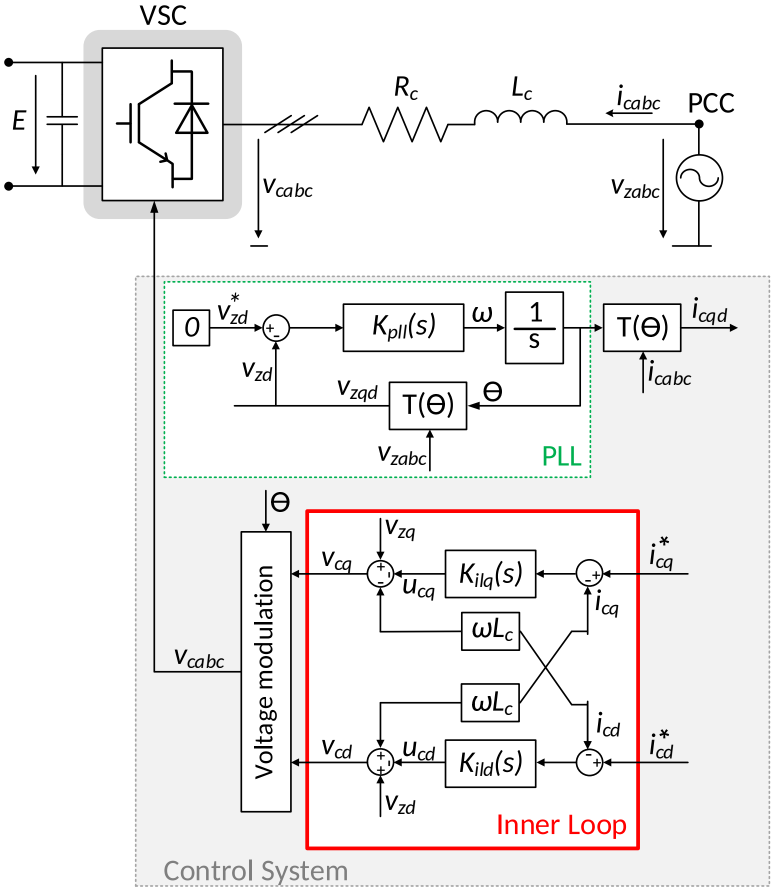

Figure 3.7: Control block diagram of converter current.

According to Subsection 3.3.1, the mathematical model describing the AC side current dynamics of the converter flowing through a L coupling filter, is as follows [39]

$$L_c \frac{d}{dt}\begin{bmatrix} i_{cq} \\ i_{cd} \end{bmatrix} = \begin{bmatrix} -R_c & -\omega L_c \\ \omega L_c & -R_c \end{bmatrix}\begin{bmatrix} i_{cq} \\ i_{cd} \end{bmatrix} + \begin{bmatrix} v_{zq} - v_{cq} \\ v_{zd} - v_{cd} \end{bmatrix} \tag{3.30}$$

Due to the existence of ωL_c terms in Equation (3.30), dynamics of i_{cq} and i_{cd} are coupled to each other. This coupling can result in an adverse trace on the efficiency of the current control loops. For this reason, an approach of the decoupling and independent control of q and d components of current is employed to avoid this drawback. In addition, the decoupling of the $q-$

and $d-$axes needs a feed-forward technique in order to inject the $\omega L_c i_{cd}$ and $\omega L_c i_{cq}$ signals into the q- and d-axis control loops when i_{cq} and i_{cd} are regulated to control the active power and reactive power, respectively. Thus, the cross coupling between q and d axes is compensated using feed-forward signals. Hence, two new control signals (u_{cq},u_{cd}) are introduced here

$$\begin{bmatrix} u_{cq} \\ u_{cd} \end{bmatrix} = \begin{bmatrix} 0 & -\omega L_c \\ \omega L_c & 0 \end{bmatrix} \begin{bmatrix} i_{cq} \\ i_{cd} \end{bmatrix} + \begin{bmatrix} v_{zq} - v_{cq} \\ v_{zd} - v_{cd} \end{bmatrix} \tag{3.31}$$

where u_{cq} and u_{cd} indicate the outputs of two current loop controllers, i_{cqd} represents the qd-axis components of the current flowing at the AC side of the converter, v_{cqd} is the qd-axis components of the voltage generated by the converter, v_{zqd} is the qd-axis components of the voltage at PCC and L_c is the inductance of the coupling filter.

According to the resulting control signals in Equation (3.31) and assuming the d-axis component of the voltage on the AC side is equal to zero ($v_{zd} = 0$), the desired fundamental components of the VSC AC voltage in the qd frame are computed as below.

$$\begin{bmatrix} v_{cq} \\ v_{cd} \end{bmatrix} = \begin{bmatrix} 0 & -\omega L_c \\ \omega L_c & 0 \end{bmatrix} \begin{bmatrix} i_{cq} \\ i_{cd} \end{bmatrix} + \begin{bmatrix} v_{zq} \\ 0 \end{bmatrix} - \begin{bmatrix} u_{cq} \\ u_{cd} \end{bmatrix} \tag{3.32}$$

Therefore, substituting Equation (3.32) into Equation (3.30), two decoupled first-order linear systems can be deduced as

$$\begin{bmatrix} u_{cq} \\ u_{cd} \end{bmatrix} = \begin{bmatrix} R_c & 0 \\ 0 & R_c \end{bmatrix} \begin{bmatrix} i_{cq} \\ i_{cd} \end{bmatrix} + L_c \frac{d}{dt} \begin{bmatrix} i_{cq} \\ i_{cd} \end{bmatrix} \tag{3.33}$$

By transforming the previous equations through Laplace, transfer functions between the currents flowing through the coupling filter and voltages of the current controller are obtained as

$$i_{cq} = \frac{1}{L_c s + R_c} u_{cq} \tag{3.34}$$

$$i_{cd} = \frac{1}{L_c s + R_c} u_{cd} \tag{3.35}$$

where s is the Laplace operator.

Based on Equations (3.34) and (3.35), the $q-$and $d-$axis variables of the converters AC current (i_{cq},i_{cd}) can be regulated by u_{cq} and u_{cd}, respectively. Moreover, by applying the Internal Model Control (IMC) technique [48, 49], the transfer functions of the controller, $K_{ilq}(s)$ and $K_{ild}(s)$, can be designed as

$$K_{ilq}(s) = \ K_{ild}(s) = \frac{K_{p-il}s + K_{i-il}}{s} \tag{3.36}$$

where $K_{ilq}(s)$ and $K_{ild}(s)$ are simple proportional-integral regulators allowing for tracking references and K_{p-il} and K_{i-il} represent proportional and integral gains, respectively. Hence, these gains are defined as

$$K_{p-il} = \frac{L_c}{\tau_{il}} \tag{3.37}$$

$$K_{i-il} = \frac{R_c}{\tau_{il}} \tag{3.38}$$

where τ_{il} is the resulting control closed loop time constant which is selected depending on the requirements of the application and the converters switching frequency. It is typically considered to be a number of times faster than the switching frequency of the VSC in order to track current references from some milliseconds to tens of milliseconds depending on the application [39]. It should be noted that u_{cq} and u_{cd} are the output of two proportional-integral (PI) regulators available in the converters current control system. Additionally, the q and d-axes PI regulators, $K_{ilq}(s)$ and $K_{ild}(s)$, process the error between the reference current and its actual value, i.e. $e_{cqd} = i^*_{cqd} - i_{cqd}$ and then provide u_{cqd}. Hence, the VSC inner controller generates v_{cq} and v_{cd} which, in turn, control i_{cq} and i_{cd} in accordance with Equation (3.30). Consequently, based on these descriptions, the state-space model of the VSC current controller can be deduced as

$$\frac{dx_{il}}{dt} = B_{il}u_{il} \tag{3.39}$$

$$y_{il} = C_{il}x_{il} + D_{il}u_{il} \tag{3.40}$$

where the inputs, outputs and state variables are

$$x_{il} = \begin{bmatrix} ei_{cq} & ei_{cd} \end{bmatrix}^T \tag{3.41}$$

$$u_{il} = \begin{bmatrix} i^*_{cq} & i^*_{cd} & i_{cq} & i_{cd} & v_{zq} & v_{zd} \end{bmatrix}^T \tag{3.42}$$

$$y_{il} = \begin{bmatrix} v_{cq} & v_{cd} \end{bmatrix}^T \tag{3.43}$$

where the matrices are

$$B_{il} = \begin{bmatrix} -1 & 0 & 1 & 0 & 0 & 0 \\ 0 & -1 & 0 & 1 & 0 & 0 \end{bmatrix} \tag{3.44}$$

$$C_{il} = \begin{bmatrix} K_{i-il} & 0 \\ 0 & K_{i-il} \end{bmatrix} \tag{3.45}$$

$$D_{il} = \begin{bmatrix} -K_{P-il} & 0 & K_{P-il} & -\omega L_c & 1 & 0 \\ 0 & -K_{P-il} & \omega L_c & K_{P-il} & 0 & 0 \end{bmatrix} \tag{3.46}$$

3.5.2 Phase Locked Loop

A Phase Locked Loop (PLL) system is used to synchronize the converter controllers with the AC grid voltage as well as to calculate the grid angle for the system Park transformations. The d-axis voltage is oriented with its reference value ($v_{zd}^* = 0$) by means of a PI controller. The output of this regulator measuring the grids angular velocity is integrated to provide the voltage angle for the transformations. The scheme of the PLL combined with the converters control system is shown in Figure 3.7 and its corresponding PI controller is expressed as [39]

$$K_{pll}(s) = \frac{K_{p-pll}s + K_{i-pll}}{s} \tag{3.47}$$

$$K_{i-pll} = \frac{K_{p-pll}}{\tau_{pll}} \tag{3.48}$$

where τ_{pll} is the PLL time constant and K_{p-pll}, K_{i-pll} are the proportional and integral gains of the PI regulator. The controller parameters τ_{pll} and K_{p-pll} are obtained from Equations (3.49) and (3.50).

$$\omega_n = \sqrt{\frac{K_{p-pll}v_z}{\tau_{pll}}} \tag{3.49}$$

$$\zeta_{pll} = \frac{\sqrt{K_{p-pll}v_z\tau_{pll}}}{2} \tag{3.50}$$

where ζ_{pll} is damping ratio, ω_n is the electrical angular velocity and v_z is the AC grid voltage magnitude.

3.5.3 Current limiter

The current of the converter can be enhanced to a given maximum value determined by the thermal limits of the converter [36, 42]. The current limiter compares the current value computed from the active and reactive reference currents with the maximum permitted magnitude. When it exceeds the rated current of the converter, the magnitude of the reference current is limited. The current limit is defined as

$$|I_c^{max}| = \sqrt{(i_{cq}^*)^2 + (i_{cd}^*)^2} \tag{3.51}$$

The current limiter implemented in the VSC control system can be achieved in several ways depending on the priorities between the active and reactive powers. Three different possible strategies for the restriction of the reference current, shown in Figure 3.8, are described below.

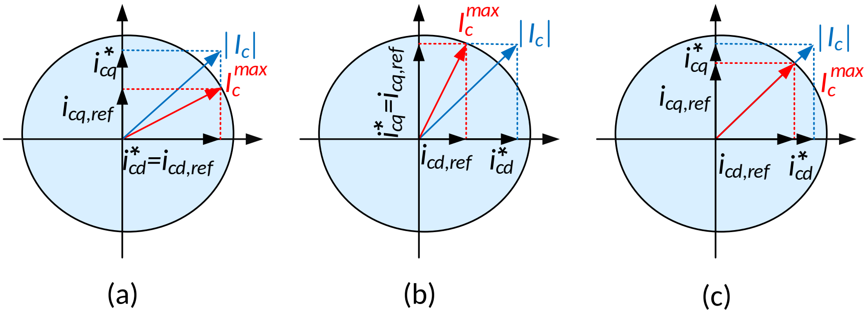

Figure 3.8: Current limiting strategies.

- Reactive power priority (i_{cd}^*): The converter will give this priority to the reactive current reference to keep the AC voltage when the current limit is exceeded. Under these circumstances, the d-axis current will be maintained and q-axis current will be reduced, as shown in Figure 3.8 (a). This strategy is generally selected when the converter is linked to a weak grid or employed to supply an offshore load.

- Active power priority (i_{cq}^{*}): When the converter is connected to a strong grid, priority is normally given to the delivery of active power. Consequently, the q-axis current will keep constant and the d-axis current will decrease, as illustrated in Figure 3.8 (b).
- limiting the current in both axes proportionally and maintaining the power factor constant (Figure 3.8 (c)).

3.5.4 Voltage Controlled Oscillator (VCO)

In the offshore load in which the frequency is not imposed by the AC system or in offshore wind farms in start-up mode, frequency control is a challenge. In order to overcome this issue, the Voltage Controlled Oscillator (VCO) is used instead of the PLL in the converter station supplying power to the offshore load or energizing the offshore grid. The output of VCO which results from the integration of the nominal frequency of the power system is used to transform voltages and currents from stationary into synchronous reference frame and vice verse [50]. Figure 3.9 shows the scheme of the VCO integrated in the VSC control system.

3.5.5 AC voltage control for offshore grids

The aim of the AC voltage controller is to generate an AC voltage with constant amplitude and frequency (v_{zabc}) for the offshore grids including wind farms and load. This voltage control loop is composed of two compensators, a decoupling feed-forward compensation and a load compensating feed-forward in order to ensure uninterrupted and balanced voltage at the offshore grid terminal and also to fulfill a pre-specified dynamic performance [50].

The AC voltage controller strategy is defined according to the load voltage dynamic model, described in Subsection 3.3.2, in order to facilitate the control design.

$$C_f \frac{dv_{zq}}{dt} = \omega C_f v_{zd} + i_{cq} - i_{olq} \tag{3.52}$$

$$C_f \frac{dv_{zd}}{dt} = -\omega C_f v_{zq} + i_{cd} - i_{old} \tag{3.53}$$

The previous relations show that the q and d-axis components of the offshore terminal voltage, v_{zq} and v_{zd}, are regulated on the basis of the AC currents

in the qd synchronous frame, i_{cq} and i_{cd}, and they are coupled to each other. Also, the effects of offshore grid currents are taken into consideration in these expressions. Hence, to eliminate the coupling between the q and d-axis components of offshore terminal voltage, a decoupling feed-forward compensation approach is applied. This technique is designed in a similar way to the one employed to decouple q- and d-axis current components, (i_{cq} and i_{cd}), in the AC current controller system.
Moreover, the control process is developed by means of a further feed-forward mechanism to compensate the impacts of the offshore grid current. For this reason, the offshore grid current values in the qd synchronous frame, i_{olq} and i_{old}, are added to the AC current references.
The AC currents in the synchronous frame can be written as follows [50]

$$i_{cq} = u_{cq} + i_{olq} - \omega C_f v_{zd} \tag{3.54}$$

$$i_{cd} = u_{cd} + i_{old} + \omega C_f v_{zq} \tag{3.55}$$

where u_{cq} and u_{cd} denote the output of the voltage controllers.
Arranging the previous functions and substituting those in Equations (3.52) and (3.53), the following relations can be deduced

$$C_f \frac{dv_{zq}}{dt} = u_{cq} \tag{3.56}$$

$$C_f \frac{dv_{zd}}{dt} = u_{cd} \tag{3.57}$$

Applying Laplace transformation to Equations (3.56) and (3.57), two decoupled $d-$and $q-$axis closed loop transfer functions are obtained

$$v_{zq}(s) = \frac{1}{C_f s} u_{cq} \tag{3.58}$$

$$v_{zd}(s) = \frac{1}{C_f s} u_{cd} \tag{3.59}$$

These equations illustrate that v_{zq} and v_{zd} are independently regulated by u_{cq} and u_{cd}.
Considering the symmetrical optimum method, two PI compensators generating two independent outputs of u_{cq} and u_{cd} can be designed. Therefore, the

PI compensators are

$$K_{ol}(s) = \frac{k_{p-ol}s + k_{i-ol}}{s} = k\frac{s+n}{s} \tag{3.60}$$

$$K_{p-ol} = k, \quad K_{i-ol} = nK_{p-ol} \tag{3.61}$$

where K_{p-ol} and K_{i-ol} are the proportional and integral control gains. In addition, the controller parameters, n and K_{p-ol}, are calculated based on Equations (3.62), (3.63) and (3.64).

$$\delta_{m-ol} = \; sin^{-1}(\frac{1-n\tau_{ol}}{1+n\tau_{ol}}) \tag{3.62}$$

$$\omega_{ol} = \sqrt{n\tau_{ol}^{-1}} \tag{3.63}$$

$$k_{p-ol} = \omega_{ol}\; C_f \tag{3.64}$$

where δ_{m-ol}, ω_{ol} and τ_{ol} denote phase margin, crossover frequency and time constant, respectively. It should be noted that the symmetrical optimum technique has disadvantages in case of offshore grid disturbances, such as load disconnection [51]. Therefore, LQG optimization procedure is appropriate to achieve a better disturbance rejection and also a faster dynamic response [51]. In other words, this methodology is selected in order to ensure the optimum regulation and stability of the closed-loop system which are the important design objectives of the voltage controller [51, 50]. The LQG compensators are defined as [52]

$$K_{ol}(s) = k_1\frac{As^3 + Bs^2 + Cs + D}{Es^3 + Fs^2 + Gs + H} \tag{3.65}$$

It should be noted that two LQG compensators in the qd synchronous frame process the error between the offshore voltage reference and its actual value, $(e_q = v_{zq}^* - v_{zq}, e_d = v_{zd}^* - v_{zd})$, and then provide u_{cq} and u_{cd}. Therefore, i_{cq} and i_{cd} are constructed based on Equations (3.54) and (3.55) and are delivered to the corresponding q and d-axis current control loops.

Finally, the AC voltage control loop of the converter station connected to the offshore grid can be designed as follows

$$i_{cq} = i_{olq} - \omega C_f v_{zd} + K_{ol}(s)(v_{zq}^* - v_{zq}) \tag{3.66}$$

$$i_{cd} = i_{old} + \omega C_f v_{zq} + K_{ol}(s)(v_{zd}^* - v_{zd}) \tag{3.67}$$

Figure 3.9 depicts the control scheme of a converter linked to the offshore load through a LC filter. Note that one assumption adopted in the AC voltage controller of this thesis is that the q and d-axis components of voltage are, $(v_{zq},\ v_{zd})=(v_{zn},\ 0)$. The v_{zn} is the nominal value of offshore terminal voltage.

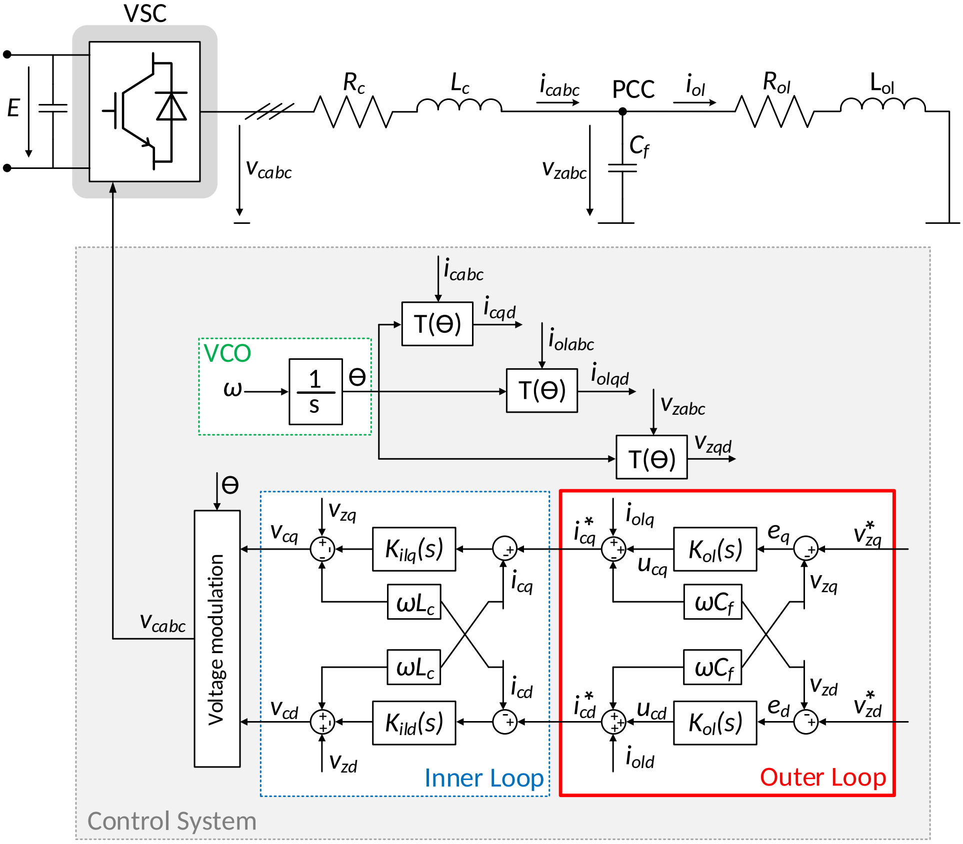

Figure 3.9: Voltage and current controller scheme for the converter connected to an offshore load through a LC filter.

3.5.6 AC voltage control for onshore AC grids

To control the AC grid voltage magnitude with its reference value, the AC voltage controller is handled in the converter station. This controller enables generation of reactive power in order to adjust the AC grid voltage. The foregoing controller comprises a PI regulator to be able to annul steady state errors. Figure 3.10 pictures the scheme of the AC voltage control in the converter linked into the AC grid by means of a L filter.

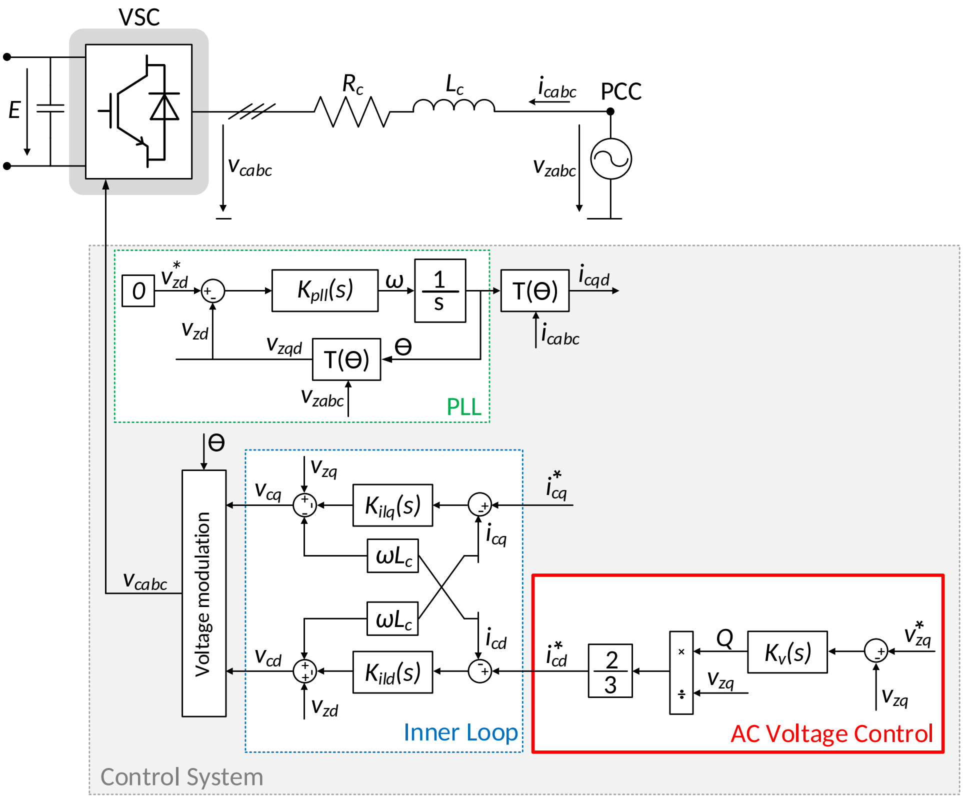

Figure 3.10: Scheme of the AC voltage controller implemention with a inner control loop for a VSC interfaced with the main AC grid through a L filter.

Due to the reactive current is associated with reactive power, as seen in Figure 3.10, the voltage of AC system can be controlled by d-axis reference current. The d-axis component of current reference can be calculated using the PI controller as

$$i^*_{cd} = \frac{2}{3v_{zq}} \underbrace{K_v(s)(v^*_{zq} - v_{zq})}_{Q} \tag{3.68}$$

where K_v is specified as

$$K_v(s) = \frac{k_{p-v}s + k_{i-v}}{s} \tag{3.69}$$

where k_{p-v} and k_{i-v} are the proportional and integral gains of voltage controller.

3.5.7 DC bus voltage control

The objectives of the DC voltage controller are the regulation of the DC voltage in the HVDC grid to ensure DC grid voltage stability and the balance between the DC grid power and the power supplied to the AC grid. This voltage controller operating in outer control loop generates the active current, i^*_{cq}, for AC current control loop. In turn, changing this current allows for the control of the DC voltage. There are several methodologies employed for DC voltage regulation, among which the droop controller and the PI controller are the most common methods. The PI controller is a simple method allowing for the regulation of output current. The foregoing technique is implemented in this thesis and further details are explained in the following subsection. Also, the description of the droop controller can be found in Appendix A.

To control the DC bus voltage by means of the AC current reference, i^*_{cq}, the output of the DC voltage regulator, i^*_{DCl}, is transformed into the active power reference value.

$$P^* = E_1 I^*_{DCl} \tag{3.70}$$

where E_1 is the DC voltage at the converter and I^*_{DCl} is the reference value of the current flowing from the dc side of the converter.

Substituting Equation (3.70) in the Equation (A.12) of Appendix A and rearranging the obtained relation, the current injected to the AC current controller of the converter can be defined as

$$i^*_{cq} = \frac{2}{3v_{zq}} E_1 I^*_{DCl} \tag{3.71}$$

- **PI controller design:**

The PI-based DC voltage regulator is mostly implemented in HVDC grids to control DC voltage at a stable level. The controller scheme for the back-to-back converter linked to the AC grid through an L filter is depicted in Figure 3.11.

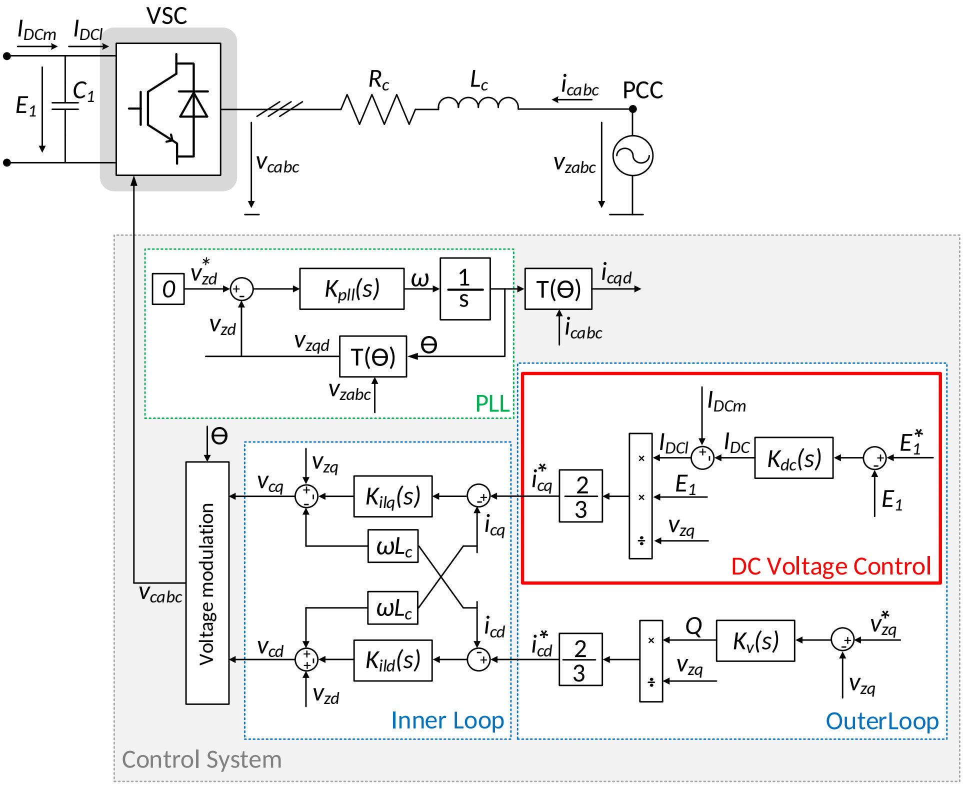

Figure 3.11: DC voltage control structure in a converter connected to the AC grid through a L filter (by using PI regulator design).

The DC bus dynamics as defined in Subsection 3.4.1 are

$$\frac{dE_1}{dt} = \frac{1}{C_1}(I_{DCm} - I_{DCl}) \tag{3.72}$$

The $(I_{DCm} - I_{DCl})$ in Equation (3.72) can be also replaced by the current flowing through the capacitor, I_{DC}, and consequently, the PI controller output can be computed as

$$I_{DC} = C_1 \frac{dE_1}{dt} \tag{3.73}$$

Transformation of Equation (3.73) into Laplace domain results in a transfer function between the controlled current and the DC bus voltage as follows

$$E_1(s) = \frac{1}{C_1 s} I_{DC}(s) \tag{3.74}$$

To achieve a satisfactory performance of the system, a controller with an integrator, such as a PI controller, is used as

$$K_{dc}(s) = K_{p-dc} + \frac{K_{i-dc}}{s} \tag{3.75}$$

where the constants of the PI controller can be computed as

$$K_{p-dc} = 2C_1 \xi_{dc} \omega_{dc} \tag{3.76}$$

$$K_{i-dc} = C_1 \omega_{dc}^2 \tag{3.77}$$

where ξ_{dc} is the desired damping factor of the DC voltage controller and ω_{dc} is the desired angular velocity of the voltage controller. Note that the stable system response can be ensured when the DC voltage controller is designed to have a much slower response than the current regulator [39]. Hence, the DC current flowing through the converter ,I_{DCl}, can be considered to be identical to the reference, I_{DCl}^* [53].

3.5.8 Constant power controller

The purpose of constant active power transmission to the HVDC grid can be attained by employing a constant active power controller in the converter station. This controller, as shown in Figure 3.12, is formulated on the basis of the instantaneous power theory as

$$i_{cq}^* = \frac{2}{3v_{zq}} P^* \tag{3.78}$$

3.6 Control systems for AC fault condition

When an AC grid fault takes place, all the generated power cannot be exported to the AC grid due to the saturation of the converter current limit. In such condition, the power that cannot be supplied to the AC system is

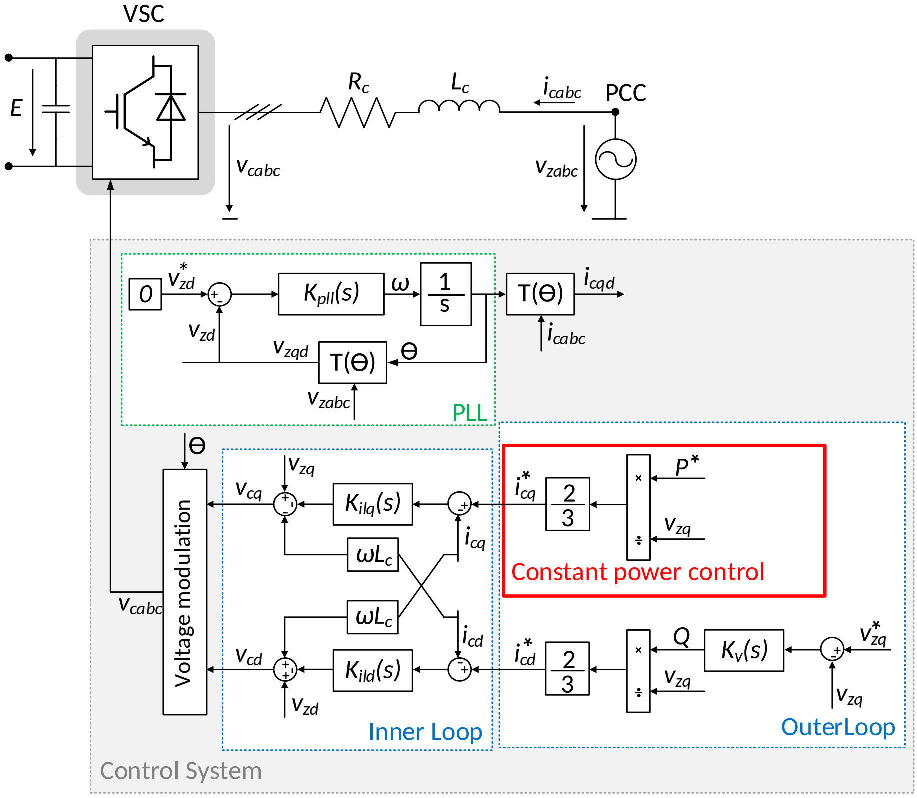

Figure 3.12: Constant power control and current and voltage control structures of a converter connected to the AC grid by means of a L coupling filter.

stored in the capacitors, and the DC voltage increases rapidly. Consequently, controlling the DC voltage will be a priority and this is accomplished by dissipating power in chopper resistors, or by reducing part of the wind farm power. In the first case, a DC chopper is employed to dissipate the additional power in a resistor during the voltage sag. The second solution is implemented by reducing the power generated by the wind farm in order to restore power balance in the HVDC grid. These two approaches are explained in more detail in next Subsections.

3.6.1 DC chopper

During short contingencies, the DC chopper prevents the DC voltage enhancement beyond a maximum permitted value. The reason for this increment is the power imbalance in the HVDC grid. The DC chopper comprising power electronic switches and resistors is installed in the DC voltage controlling converter stations. Moreover, it can be modeled as a voltage controlled direct current source, the value of which can be defined as

$$I^{*}_{dc-chopper} = k_{dc-chopper} \frac{E_2 - E_2^{min}}{E_2^{max} - E_2^{min}} \tag{3.79}$$

where $I^{*}_{dc-chopper}$ is the current injected by the current source, E_2 is the DC voltage, E_2^{max} and E_2^{min} are the upper and lower thresholds of the DC voltage in terminals of the converter and $k_{dc-chopper}$ is a gain chosen on the basis of the nominal capacity of the DC chopper and DC voltage, namely, S_n/E_2 [54]. Figure 3.13 illustrates the scheme of a DC chopper.

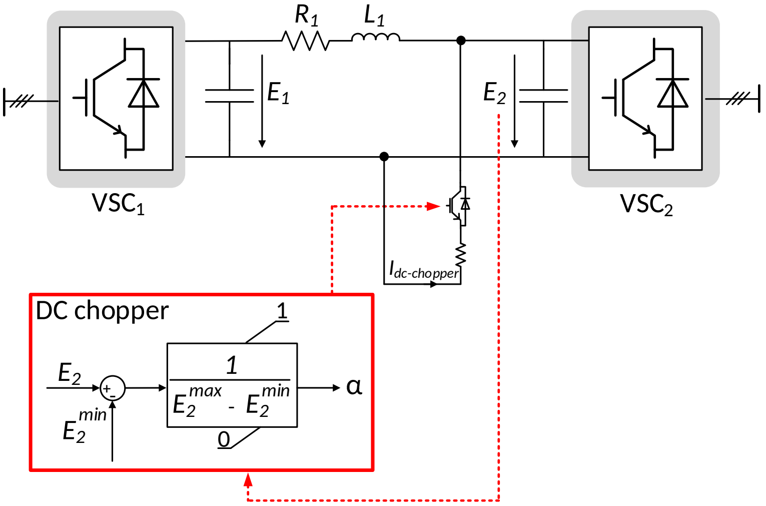

Figure 3.13: Scheme of a DC chopper.

where α is the duty cycle and is issued for transistors controlling the DC chopper. Once the value of E_2 is equal to E_2^{min}, α becomes zero and when the E_2=E_2^{max}, the value of α is to 1. Actually, the DC chopper operates linearly.

when the DC voltage exceeds of the pre-defined threshold, the DC chopper dissipates the amount of current flowing in the DC grid which prevents in turn all the active power from being transmitted to the AC grid. The main advantages of this technique are that the output power of the wind farms remains constant during the fault and the system remains stable in case of fault.

3.6.2 Wind farm power reduction by controlling HVDC converter

HVDC converters connected to the wind farm are adjusted to transfer all the power generated by wind farm to the HVDC grid. When a long fault occurs (e.g. the disconnection of a line) and the DC voltage reaches the allowable limit, E_1^{max}, the operating mode of the converter at the wind farm side is switched to power reduction mode. In this case, the converter enables controlling the DC voltage by decreasing power injection [55]. This action can be implemented using a variation of the wind farm power reference. It should be noted that power dissipation through the DC chopper is not possible due to the overheating of the resistors. The power reduction control law is stated accordingly through the following expression

$$P_{wf}^{red} = P_{wf}^{*} - \underbrace{k_k(E_1^{max} - E_1)}_{P} \tag{3.80}$$

$$k_k = E_1 k_{droop} \tag{3.81}$$

where P_{wf}^{red} is the reduced power of the wind farm, P_{wf}^{*} is the wind farm power reference, E_1 is the DC voltage, E_1^{max} and k_{droop} are control constants to be chosen in the control system design, so that the stability and performance are guaranteed under any possible conditions.
The previous relation indicates that the power reduction approach utilizes a droop characteristic for the injected power decrement.

3.7 Summary

In this chapter, the average model of the VSC converter, AC grid coupling filter models and DC grid models have been studied. Also, a control scheme based on a two-level cascaded control system (inner and outer control loops) has been explained. Three possible control modes for outer loop have been represented: the AC voltage control mode, the DC voltage control mode and the constant power control mode. One technique for DC voltage regulation including a PI controller has been analyzed. In order to create a stable voltage for offshore grids as well as to keep AC voltage constant under normal and abnormal conditions, two different AC voltage control strategies have been presented. It is pointed out that inner current loop is a fundamental to any control systems.

Chapter 4

Modeling and control of a wind turbine equipped with full power converter

The scopes of this chapter comprise the description of a dynamic simplified model for the full power converter wind turbine of an offshore grid and the explanation of a control scheme. Finally, a simulation to test the employed model will be also carried out in this chapter.

4.1 Introduction

A variable-speed wind turbine equipped with a full power converter as well as a control scheme for the wind turbine will be modeled in this chapter. The simplified model is presented in order to reflect the dynamic response of the wind turbine to different incoming winds. The models of turbine, drive train, generator and Machine Side Converter, MSC, are represented together in this simplification, while the mathematical description associated with the DC bus of the wind turbine is separately discussed. Note that the equivalent scheme of the wind turbine converter at the grid side is the same model of converter in the HVDC transmission system. The control systems used for wind turbines can be classified in two groups of electrical and mechanical controllers. The control system of the MSC and GSC converters forms the electrical controller of the wind turbine, whereas the pitch control system and DC chopper of the wind turbine develop the mechanical controller. The control scheme of the Grid Side Converter, GSC, is used for the regulation of DC bus voltage.

Therefore, this study is organized as follows: Section 4.2 briefly describes the wind turbine with full power converter. Section 4.3 focuses on the simplified model of the wind turbine. Section 4.4 discusses the control scheme of this wind turbine system. Finally, the simulation results are presented in Section

4.5 in order to confirm the validity of the model and control design.

4.2 Variable-speed wind turbine with full power converter

PMSG wind turbines equipped with full power converter are increasingly employed in the industry due to their features. In this wind turbine technology, the generator and AC system is decoupled through power converters, to reduce the effect of a grid fault on the generator. In addition, the machine side converter makes the generator operates within a wider speed range. Hence, power extraction from the wind can be maximized. Furthermore, the converter at the grid side can meet the requirements of grid codes. Therefore, the reactive power support can be supplied, especially under fault condition, and the wind turbine can withstand the AC system faults [4, 56].

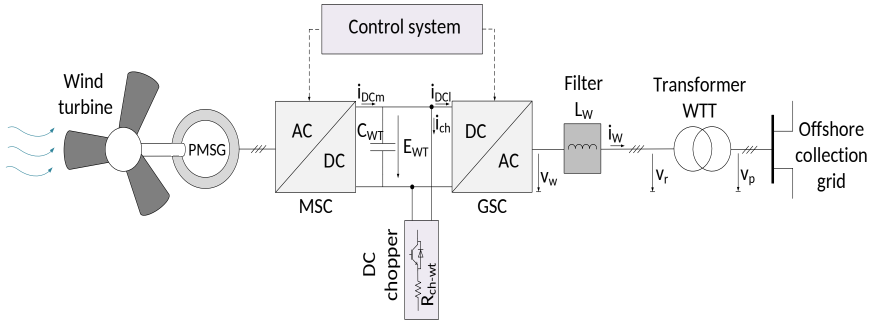

Figure 4.1: General scheme of a wind turbine equipped with full power converter.

A conceptual schematic of the full-scale converter wind turbine is illustrated in Figure 4.1. The wind turbine captures the power from the wind kinetic energy. Then, the extracted power is transmitted through a shaft into a PMSG direct driven generator. This generator, which produces the electrical power, is interconnected to the AC power system through a full power converter. In this type of generator, the excitation is provided by means of the permanent magnets. Therefore, excitation losses can be considerably diminished [4]. Also, the lack of slip rings is an advantage that results in low maintenance of these machines [56]. Thereby, PMSG generators can be used for offshore applications.

The full-scaled power converters linked to the stator windings of the generator are based on the insulated gate bipolar transistors (IGBTs) technology. These converters make the generator speed to be fully decoupled from the constant-frequency AC system. Also, the capacity of converters is considered to be identical to or larger than the nominal generator power.
The converter of the generator side injects the current into the DC circuit in order to charge the DC capacitor. The grid side converter, which is interfaced into the AC power grid (collection grid) through a transformer, controls the DC bus voltage. The transformer of the wind turbine steps up the output voltage of the grid side converter to the voltage of the offshore collection grid. Under operating condition, a DC chopper is applied to bypass the voltage sages [4]. To limit the power extracted from wind, a pitch control system is embedded.

4.3 Simplified model of a full power converter wind turbine

In order to represent the wind turbine dynamic behavior during offshore grid simulations, design the control system and facilitate the study of the wind turbine, which presentes numerous mechanical complexities, a simplified model is considered in this thesis. This dynamic representation applied to wind turbines equipped with full power converter is divided into three main parts, as shown in Figure 4.2. The first one is related to the dynamic model of the mechanical and electrical systems of the wind turbine, including turbine aerodynamic, pitch system, drive train, generator and the machine side converter. The second and the third part refer to the modeling of the grid side converter and the DC link of the wind turbine. The wind turbine converter at the offshore collection grid side can be modeled by the same

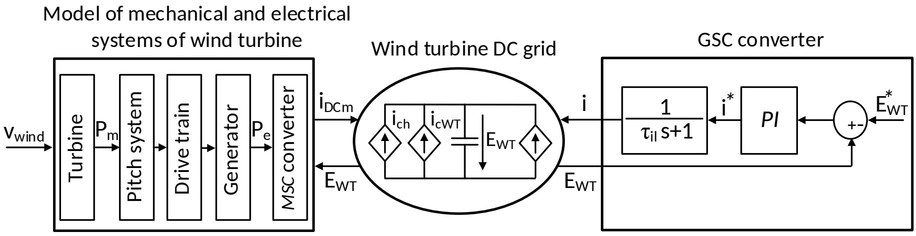

Figure 4.2: Block diagram of simplified model of wind turbine equipped with full power converter.

representation of the HVDC system converter, included in Subsection 3.3.1 of Chapter 3. The model of the electrical and mechanical systems of the wind turbine is expanded in detail below.

The dynamic simplified representation of the electrical and mechanical systems, indicated in Figure 4.3, is presented in order to show the variations of power captured by the wind turbine according to the variations in the incoming wind speed. For this purpose, the turbine aerodynamics are represented by a power-wind speed curve, so that the mechanical power of the wind turbine can be changed depending on the speed of incoming wind. Further description regarding the aerodynamic model can be found in Subsection 4.3.1. For higher wind speeds, the extracted power can be diminished through a pitch control system. In fact, the mechanical power reduction can be accomplished by filtering the difference between the captured mechanical power and the power reference. Henceforth, the power controlled by the pitch system is smoothed thanks to the dynamics of the mechanical and electrical systems. These systems, containing the drive train and generator, allow to transfer the mechanical power into the generator and convert it into electrical power. Therefore, their simplified model is composed of a dynamic $\frac{1}{J_{WT}s+1}$ corresponding to the rotor inertia and a dynamic $\frac{1}{\tau_{ele}s+1}$ corresponding to the electrical system. The J_{WT} and τ_{ele} are inertia and electrical time constants for the wind turbine, respectively [40].

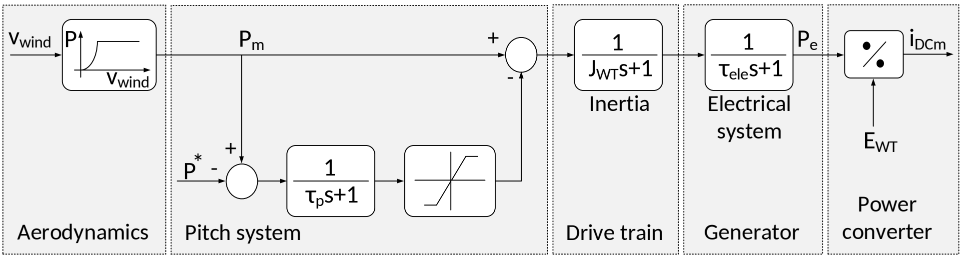

Figure 4.3: The simplified model of wind turbines electrical and mechanical systems.

Finally, the electrical power obtained from the generator can be divided by the DC bus voltage in order to inject current into the DC link of the converter, according to Equation (4.1). Thus, the generator side converter can be modeled.

$$i_{DCm} = \frac{P_e}{E_{WT}} \tag{4.1}$$

Moreover, the dynamic model of the wind turbine DC link shown in Figure 4.2 can be defined as

$$\frac{dE_{WT}}{dt} = \begin{bmatrix} \frac{1}{C_{WT}} & -\frac{1}{C_{WT}} & -\frac{1}{C_{WT}} \end{bmatrix} \begin{bmatrix} i_{DCm} \\ \frac{E_{WT}}{R_{ch-wt}} \\ i_{DCl} \end{bmatrix} \tag{4.2}$$

where E_{WT} is voltage of DC bus, C_{WT} is the capacitor of wind turbine DC bus, i_{DCm} is DC current injected by the machine side converter, i_{DCl} is the current through the DC side of the GSC converter and R_{ch-wt} shows the resistance of DC chopper in DC bus.

4.3.1 Aerodynamic model of the wind turbine

The mechanical power generated, P_m, depends on a power coefficient, C_p, and kinetic energy in the air passing across an area swept by rotor blades, P_{wind} [57]. In fact, the value of this extracted aerodynamic power can be calculated as [57]

$$P_m = C_p P_{wind} = \frac{1}{2} C_p \rho A v_{wind}^3 \tag{4.3}$$

where ρ is the air density, A is the area swept by the rotor blades and v_{wind} is the wind speed. The power coefficient C_p which is a function of the tip speed ratio λ and the blade pitch angle ϑ can be achieved as

$$C_p(\lambda, \vartheta) = c_1(c_2 \frac{1}{\Lambda} - c_3\vartheta - c_4\vartheta^{c_5} - c_6)e^{-c_7 \frac{1}{\Lambda}} \tag{4.4}$$

where $[c_1 ... c_9]$ are the wind turbine power coefficients and Λ is defined as

$$\frac{1}{\Lambda} = \frac{1}{\lambda + c_8\vartheta} - \frac{c_9}{1 + \vartheta^3} \tag{4.5}$$

The relation between the rotational speed of the wind turbine ω_t and the average wind speed can be described as the tip speed ratio λ

$$\lambda = \frac{\omega_t R}{v_{wind}} \tag{4.6}$$

where R is the turbine radius.

Through the differentiation from Equation (4.4) and solution of its roots, the computation of the maximum efficiency of a wind turbine is possible. For the sake of facility, the pitch angle of blades is considered as a constant value of ϑ=0. Therefore, the optimal value of the power coefficient C_p^{opt} can be deduced as follows

$$C_p^{opt} = \frac{c_1 c_2 e^{-\frac{c_6 c_7 + c_2}{c_2}}}{c_7} \tag{4.7}$$

Moreover, the optimum tip speed ratio for the calculation of C_p^{opt} is

$$\lambda_{opt} = \frac{1}{c_9 + \frac{c_6}{c_2} + \frac{1}{c_7}} \tag{4.8}$$

Therefore, in order to maximize the energy extraction from the wind, the tip speed ratio should be kept at λ_{opt}.

4.4 Control system of full power converter wind turbine

To regulate a wind turbine, two controller types are required: the mechanical and the electrical control system. Each of the power converters of the wind turbine, MSC and GSC, contains a classic vector control that acts as the electrical controller. The structure of the GSC control, as shown in Figure 4.4, consists of an inner loop and an outer loop. The outer loop comprises only a DC voltage controller and is responsible for DC bus voltage regulation. This voltage loop is controlled by means of a proportional-integral (PI) regulator and provides the current reference for the inner current control loop. The AC voltage controller is eliminated in the outer loop of the wind turbine GSC converter in order to avoid the confluence of the aforementioned controllers operation with that of the AC voltage control system of the offshore HVDC converter [37]. Moreover, to orient the control system with grid voltage, a Phase Locked Loop (PLL) is used in the GSC. In the power converter of the machine side, only DC current is injected to the DC link, corresponding to the power generated by the wind turbine and the DC bus voltage. The mechanical control of the wind turbine includes a pitch system. This control system diminishes the power captured from the wind when the power is above the nominal level. The pitch system has the slow dynamics. Hence, a DC chopper is implemented in the wind turbine in order to dissipate the power in case that power reduction through the pitch

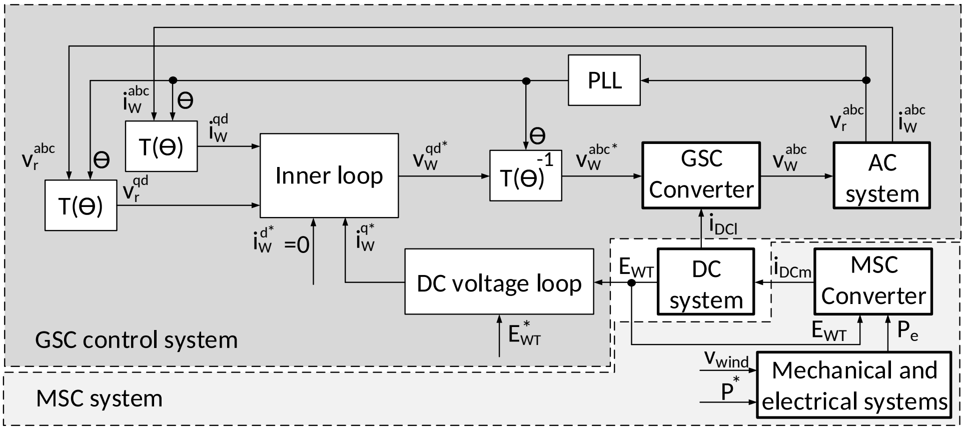

Figure 4.4: Control scheme of the wind turbine.

controller is not possible. Further details about the DC chopper, DC voltage controller and inner loop can be found in Chapter 3.

4.5 Simulation results

To evaluate the performance of the simplified model and the wind turbine control system, a simulation is carried out using MATLAB/SIMULINK software. The scheme of the simulated system is shown in Figure 4.3. The characteristic parameters of the wind turbine used in this simulation have been presented in Table 4.1. The wind turbine considered is based on Areva M5000 model.

Figures 4.5 (a)-(d) show the wind speed, the mechanical power, the mechanical power controlled by the pitch controller and the electrical power, respectively. It can be seen that the mechanical power varies along with changes in wind speed. Also, this power extracted by the turbine can be limited through a pitch system, when it exceeds the nominal value, as illustrated in Figure 4.5 (c). The electrical power generated by means of the machine that reflects the wind speed variations and dynamic behavior of the drive train and PMSG is indicated in Figure 4.5 (d).

Table 4.1: Wind turbine characteristic parameters

Parameter	Value	Units	Description
R	58	m	Turbine baldes radius
ρ	1.225	kg/m^3	Air density
J_{WT}	1.7	s	Inertia time constant
ϑ	0	°	Pitch angle of rotor blades
τ_{ele}	0.01	s	Electrical time constant
τ_p	0.17	s	Pitch time constant
ω_{nom}	14.8	$\min^{-1}$	Nominal speed
c_1	0.5	1	C_p function parameters
c_2	116	1	
c_3	0.4	1	
c_4	0	1	
c_5	0	1	
c_6	5	1	
c_7	21	1	
c_8	0.08	1	
c_9	0.035	1	
λ_{opt}	0.411	1	Optimum tip-speed ratio
C_p^{opt}	8	1	Optimum power coefficient
P_{WT}	5	MW	Nominal power of wind turbine
$v_r/\ v_p$	3.3/33	kV	Nominal transformer voltage
P_{conv}	5.6	MVA	Nominal converter power
E_{WT}	6	kV	Nominal DC voltage

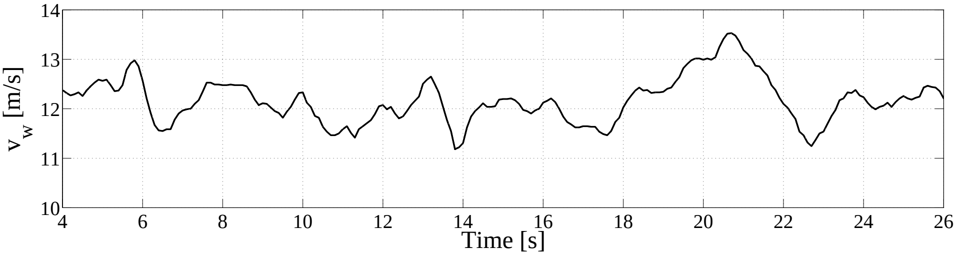

(a) Wind speed

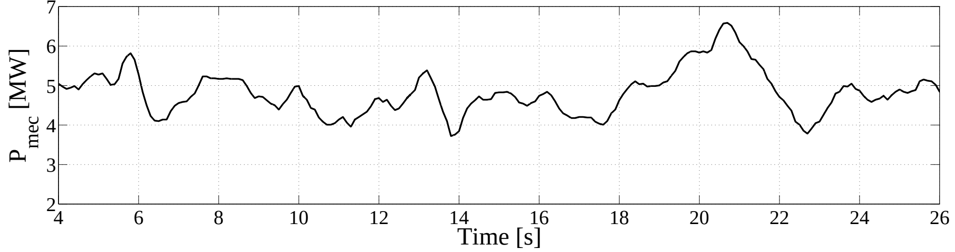

(b) Mechanical power

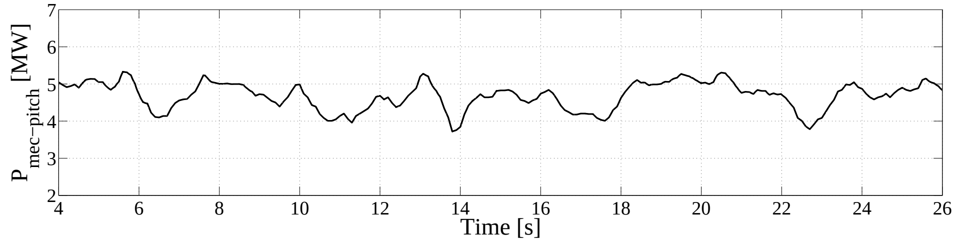

(c) Mechanical power controlled by pitch

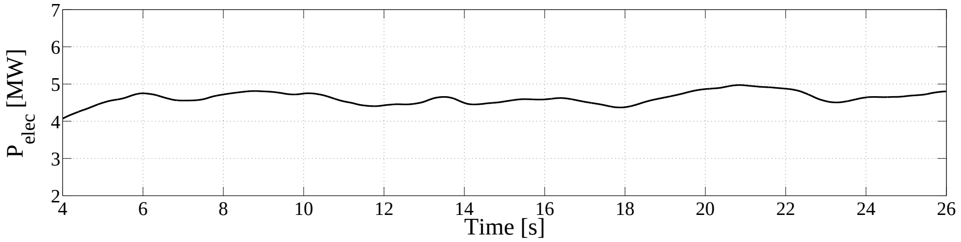

(d) Electrical power

Figure 4.5: The performance of the simplified model for various wind speeds.

As shown in Figures 4.6 (a) and (b), the DC bus voltage is stable due to the utilization of the DC voltage controller in GSC, whereas the AC current value of GSC varies on the basis of the produced power.

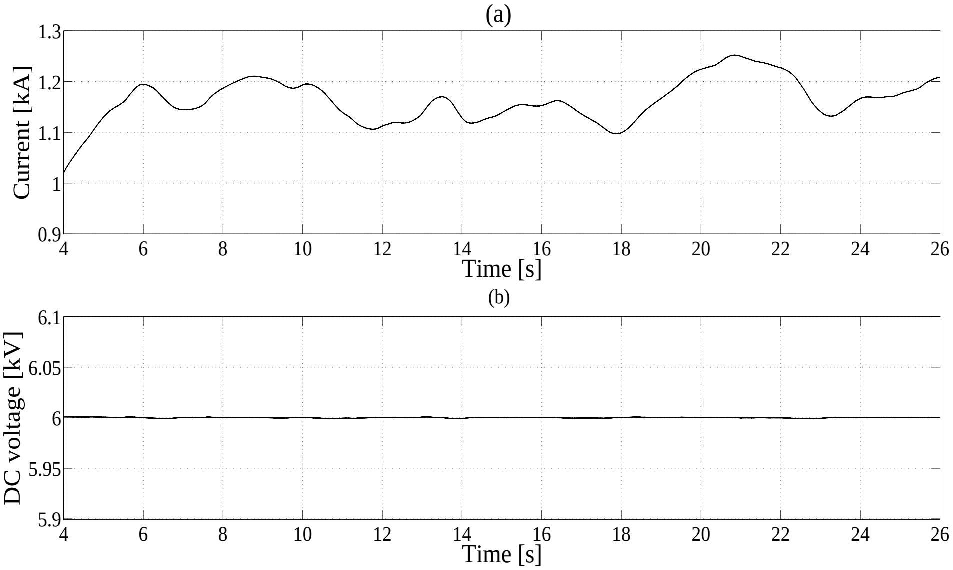

Figure 4.6: Evaluation of the current of GSC converter and DC voltage.

Chapter 5

Transformer inrush current in HVDC systems

This chapter will describe the state of the art of transformers inrush current, the impact of the inrush current phenomenon on the HVDC system, the techniques applied for inrush current limitation and the requirement for a novel reduction strategy in HVDC transmission systems. Finally, it will present a transformer model considering magnetic core effects for inrush current investigation.

5.1 Introduction

The security and reliability of the offshore HVDC grid in operation under different condition is important. One of the challenges related to power transmission in HVDC systems is transformers inrush current during energization and restoration after fault removal. Tripping the HVDC converter and disturbing HVDC power transfer can be the outcome of these high inrush currents [58, 59]. Transient magnetizing currents or the selfsame magnetizing inrush currents are generated by the iron core saturation of the transformer. These currents are one of the significant abnormalities in transformers as well as their amplitudes are generally several times the nominal current. The first inrush current was observed by Ferranti when commissioning the Deptford to London 11 kV link in 1890 [60]. For more than 100 years, these transformer inrush currents have caused some difficulties, such as the malfunction of protective relays and power quality reduction of the network [17, 60]. Hence, knowledge of transformers behavior under normal operation and transient cases is a requirement for the reliable and stable performance of transformers protection devices [61, 62]. Thus, the possibility of achieving this knowledge could be provided by transformer modeling which is a vast topic. Therefore, in order to study inrush transient behavior of transformers during the energization and recovery modes, some representations have been proposed.

These models used for transformers transient are classified as: Matrix model (BCTRAN model), Saturable Transformer Component (STC) model, Topology-based model (Duality based model and Geometric model), Model based on a T-equivalent circuit and Model based on a π-equivalent circuit [63, 64].

These models deal with the main problems, such as, the lack of information about parameters, modeling of hysteretic iron-core, modeling of winding losses, adequate modeling of transformers behavior in complete saturation and determination of the residual fluxes in order to investigate inrush transients. In this chapter, a simplified model of a three-phase transformer is presented to show the non-linear behavior of transformers under transient condition. The suggested dynamic model, which is based on a T-equivalent circuit, represents in detail the non-linear magnetic core. In fact, an appropriate representation for the nonlinearity of the magnetizing branch is proposed in which the saturation characteristics of the core are estimated by means of a piecewise linearization method. Based on this model, the non-linear differential equations defining the transient behavior of the magnetizing branch can be solved easily, and finally, yield results in reasonable simulations.

Furthermore, due to the importance of the power grids reliability and stability in the electric industry, transformer inrush current reduction has attracted researchers attentions. Over the past decades, many techniques for transformer inrush current control have been proposed, based on the idea that the magnetizing current is dependent on various operating conditions [65]. However, the application of these techniques in HVDC transmission systems has drawbacks such as high costs, high losses and slight reliability [66, 67, 68, 69, 70]. Moreover, the reduction of the transformer inrush current in HVDC systems using a pre-insertion resistor has been suggested in Literature [19]. This method, applied for the inrush current decrement in the energization procedure of the doubly-fed induction generator offshore wind farms connected to Modular Multilevel Converter (MMC)-HVDC system, has disadvantages such as high costs and losses. Therefore, due to the importance of HVDC operation during the inrush transient period, a better scheme is needed to overcome these problems. Therefore, this thesis proposes a strategy based on transformers voltage ramping in order to minimize the inrush current within the energization and restoration of transformer and improve power quality.

5.2 Transformers inrush current

In power systems, transformers manifest themselves as non-linear elements due to the magnetizing characteristics of the iron core during the transients. For this reason, the inrush transients can take place and endanger the HVDC system operation. These inrush currents are generally categorized into three different groups: recovery inrush current, sympathetic inrush current and energization inrush current. The recovery inrush current takes place when the transformers voltage is restored after removal of short-circuit in the system. The sympathetic inrush can occur when two or more transformers are operated in parallel. In addition, the energization inrush current is the most common form of inrush current [71] and results from the switching-on of a transformer which has been previously de-energized. This current, including the highest current magnitudes, is analyzed in detail below.

Transformers energization in offshore power systems usually results from connecting a HVDC converter to a transformer under the no-load condition. When energization occurs, the voltage across the high voltage winding of the transformer will experience an abrupt change. Therefore, a magnetic flux in the core equal to the integral of the induced voltage is created [17, 18] and is added to the residual flux. A brief description of the residual flux has been provided in Appendix B.

When the polarity of residual flux is in the direction of flux produced after transformers switching, the whole flux can exceed the saturation knee point of the iron core. Therefore, the transformers core will be driven into the saturation region and the transformer winding will operate as a winding with an air-core. Consequently, the inductance of the transformer winding is rapidly reduced to the percentage of its normal value and hysteresis and eddy losses will also be negligible. Due to flux saturation in the magnetic core, the transformer will draw a large magnetizing current from the supplying network to be able to maintain the magnetic flux in the core. This current is known as energization inrush current [66, 72].

This energization inrush current rises suddenly to its maximum level in the first half cycle after the transformers switching-on and thereupon, it fades slowly [73]. Each cycle of this current is also composed of a steady-state component and a transient component. The first one is governed by the used voltage and air-core impedance of the excited winding and the second one derives from the saturation of transformers core [72].

5.2.1 Effects of different factors on inrush current

During the energization of the no-load power transformer, the magnitude, waveform and time duration of the magnetizing inrush current drawn by the transformer are generally influenced by parameters of the power network supplying the transformer and by the characteristics of the transformers design (i.e., the structure of transformers and magnetic effects of transformer core) [60, 74]. These two factors are the phase angle of applied voltage at the moment of the transformers energization (i.e., switching angle), the impedance of the power system [65, 75], transformers size, core material, winding connections in three-phase transformers [65, 75] and the magnitude and polarity of the residual flux stored in the transformer core at the instant of energization, ϕ_r, [60, 66, 67, 76, 68, 77].
Depending on the combination of the foregoing parameters, the worst-case scenario of inrush current can take place. This case includes the highest peak current which will usually appear in the first period after the transformers magnetization [78]. Hence, these mentioned parameters are briefly described in the following sections.

A: Switching angle:
One of the important parameters determining the amplitude of the peak inrush current is the point on the voltage wave at the moment of transformers switching-on or the switching angle β [66, 77, 79]. This switching angle can be obtained based on Equation (5.1) [79]

$$\beta = \arccos\left[\frac{i_{max}}{i} - \frac{\phi_r - \phi_{sat}}{\phi_n} - 1\right] \tag{5.1}$$

$$i = \frac{v_m}{\sqrt{R^2 + (\omega L_{sat})^2}} \tag{5.2}$$

where i_{max} indicates the peak inrush current, i states the amplitude of the steady-state current for the saturated transformer, v_m is the magnitude of the source voltage, L_{sat} is the winding inductance during the saturation, R is DC resistance of the energized high voltage winding, ϕ_n is the nominal flux of the winding, ϕ_{sat} and ϕ_r are the saturation flux and residual flux, respectively. The description of the fluxes can be found in Appendix B.
When the energization of the transformer takes place at the zero point on the voltage wave ($\beta = 0°$) and the transformer has positive residual flux, the

maximum inrush current will be reached in the high voltage winding. Therefore, this can be called as the worst-case scenario in the energization of the transformer [75, 80].
In addition, the transformers energization at a maximum point on the applied voltage waveform ($\beta = 90°$) leads to the minimum inrush current [1, 75].

B: Impedance of the supply circuit:
During energization, impedance between the transformer and the supply source affects the amplitude of the voltage at the transformers terminals.
Hence, the magnitude of the peak inrush current is influenced by this source impedance. Namely, an increment in the source impedance leads to a reduction in the peak inrush current [81].

C: Transformer power (MVA):
The magnitude of the peak inrush current depends on the MVA size of the transformer. On the other hand, small power transformers provide higher amplitude of peak inrush current compared to larger transformers with the same core material [75].

D: Core material:
A transformer core saturated during the inrush phenomenon is constructed from laminations. These laminations are thin strips of high-grade electrical steel and are electrically isolated by a thin coating of insulation. The flux density of the steel, the design of the core and the connection method used for the laminations to create the core section influence the magnitude and duration of the magnetizing inrush current.
Over the last few decades, there have been some changes in transformers design [75]. Nowadays, some transformers are designed using high-permeability (High-B) electrical steel (e.g. H & D materials) in order to provide more consistent grain orientation. This feature in turn results in a greater saturation flux density, a bigger linear portion of the magnetization characteristic curve and a smaller level of residual flux density in comparison with the conventional grain-oriented electrical steel type materials (e.g. R material) [75]. Therefore, transformers with these core materials, namely modern transformers, have lower magnetizing inrush currents [75].

E: Residual flux:
The residual flux within the transformers core causes changes in the inrush current changes. The level of this flux that remains in the transformers core

depends on the instant of transformers de-energization and can be within the range -1pu to $+1$ pu. When a transformer is energized at the zero point of voltage, the inrush current increases or decreases with regard to the polarity of residual flux [80]. Further details about the residual flux can be found in the Appendix B.

F: Winding connection type:
For a three-phase transformer of power system, the propagation of the inrush current in one phase to the other phases is dependent on the coupling type of transformers windings and the grounding of transformers winding with star (Y-) connection. Due to the presence of full inrush current in the Y-connected primary winding, the line current will be increased, whereas the reduction of line current can be illustrated in Δ-connected primary winding. The reason of this fact can be crossing inrush current in the other phases of Δ-connected winding [71, 75].

5.2.2 Magnitude, waveform and time period of inrush current

The magnetizing inrush currents are frequently generated during the power transformers energization. The severity of the first peak inrush current, which is influenced by numerous factors, such as the residual flux, voltage angle, etc., may attain many times the nominal magnetizing current of the power transformer. For this reason, this current can be mistaken with a short circuit current and lead to the trip out overcurrent and differential relays. Hence, the accurate calculation of the amplitude of the inrush current is important for the design of protective systems of transformers [65].

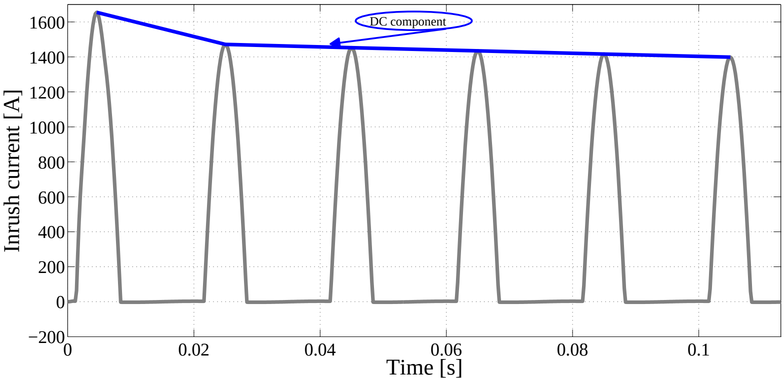

Figure 5.1: Inrush current waveform for one phase of the HVDC transformer.

The waveform of the magnetizing inrush current is non-symmetrical. For this reason, this current has high order harmonics and DC component which makes power quality decrease [60]. A typical inrush current waveform is illustrated in Figure 5.1. The DC component and even harmonics of different magnitudes can be easily seen. It should be noted that the DC component and the current waveform decrease along with time.
The magnitude of inrush current is not a constant quantity, but it changes with time and decays slowly after several minutes [81, 82]. Therefore, this current can take along time to reach its steady-state value. The attenuation time of inrush current depends on the impedance of the circuit including the impedance of the system connected to the transformer, as well as that of the transformers winding and magnetizing impedance [81]. Due to the nonlinear effect of transformer magnetization inductance, the calculation of the decay rate using a L/R time constant is very difficult.

5.2.3 Inrush current harmonics

The transformer is a harmonic current source. The energization of the transformer will produce a magnetizing inrush current which includes all harmonic components and a DC component [60]. The harmonics of the transformer inrush current generally decay when this current fades to the steady-state mode [60]. The second harmonic content of this current is a significant order of harmonics and is also dependent upon the magnetizing characteristic of the core. In fact, its value becomes higher when the saturation flux density, B_{sat}, is smaller. Moreover, current corresponding to the second harmonic order is usually applied to distinguish inrush currents of power transformer from fault currents, so as to restrain the operation of the transformer differential protection during energization.

5.3 Impacts of transformer inrush current on the HVDC system

Transformer inrush transient can influence the operation of the HVDC transmission system and threaten the stability of this grid. In fact, the function of the HVDC converter can be interrupted through converter protection due to current saturation as well as transition of the HVDC power can be delayed. Moreover, this large transient current, which is rich in terms of harmonic content and contains a high direct current component, can result in the unexpected tripping of the transformers protective devices and consequently, it can lead to failure of the transformers energization or recovery operation.

Furthermore, insulation failures in power transformers which are energized under no-load condition or are restored after fault clearance are hazardous effects of the inrush current [66]. In addition, the presence of drastic electromagnetic stresses provided by the magnetizing inrush current alleviates power transformers life time [68].

5.4 Reduction strategies of transformer inrush current

Considerable inrush current in the power transformer can occur due to the magnetic saturation resulting from a sudden change in the transformers voltage. In order to limit the magnetizing inrush current magnitude, several technologies have been rendered by researchers, which can be classified as: pre-insertion resistor, controlled switching, neutral resistor with sequential switching, reduction of residual flux and prefluxing [67].

The most prevalent techniques among them are controlled switching and pre-insertion resistors. However, the transformer controlled switching method needs the value of residual flux in transformer core, it is more economical and reliable than the pre-insertion resistors [83]. The reason is that the pre-insertion resistor method needs to install large resistors [84]. Therefore, the present section will explain the available technologies for inrush current diminution.

5.4.1 Pre-insertion resistor strategy

One old method for the reduction of the energization transients in transformers is the pre-insertion resistor scheme. In fact, this technique is based on the temporary insertion of a relatively large resistor in series with the circuit when the transformer is switched on. Consequently, using this strategy, voltage collapse can take place across the pre-insertion resistor and the decrement of transformer windings voltage and the core flux can also result from this [85]. Finally, the inrush current can be decreased.

Although this technique is simple and leads to inrush current reduction, it has two disadvantages: the excessive loss and the considerable cost to upgrade the breakers [17, 69, 70].

5.4.2 Controlled switching strategy

Controlled switching technology is mainly designed to decrease transformer inrush currents at the moment of energization and to prevent power quality degradation. This much more flexible method switches on the transformer at the optimal point on the voltage waveform to be able to suppress transient inrush currents [86].

If the appropriate time for transformer energization is at the peak of the voltage waveform, reduction of the transient flux caused by the transformer core and consequently inrush current are certain. However, transformer energization at the zero point on the voltage waveform can lead to the generation of a peak inrush current [69].

Therefore, there are three various strategies for controlled energization of the transformer that are discussed below. In these techniques, the closing instants of circuit breaker poles are controlled and performed in an adequate sequence [66, 68].

A: Rapid closing strategy:

The function of this methodology is to close one phase first and then the other two phases during a quarter cycle to minimize the inrush current and to improve power quality in the power system. The main shortcomings of this approach are the need for residual flux information in all phases and the independent regulation of circuit breakers, which are necessary to fulfill this closing process [66, 68].

B: Delayed closing strategy:

This closing technique implies to energize one phase in the beginning and to delay the switching of the two remnant phases 2-3 cycles later. The requirements of this strategy are the data of the residual flux just in one phase and the independent control of circuit breaker [66, 68].

C: Three phase simultaneous closing strategy:

This strategy has proved to reduce the magnetizing current by simultaneously closing all phases at a proper polarity and amplitude of residual flux. Thus, the information regarding the residual flux of all phases is important in this method.

The application of this strategy is limited to cases where the residual fluxes are equal to zero in one phase and have high values in the other two with opposite polarities [66, 68].

5.4.3 Neutral resistor with sequential switching strategy:

A proposed approach for reduction in the inrush current is sequential energization with a neutral resistor, as shown in Figure 5.2. This method involves a combination of a grounding resistor at the neutral point of the energizing transformer and a sequential switching strategy [1, 87]. The basic principle for the restriction of the inrush current in the referred technique is the establishment of some damping in the inrush currents by means of the neutral resistor. The reason for this is the unbalanced flow of these currents in different phases. Hence, in this method, each of the transformer phases is sequentially switched on and the neutral resistor will be connected in series with the switched phase. Thereby, the reduction of the induced voltage across the energized winding occurs. Consequently, it can be stated that the performance of the proposed technique is similar to that of the pre-insertion resistor technique [1, 87]. In view of the fact that the diminution in transformer transient current is a function of the size of the neutral resistor, an appropriate choice of this resistance value can considerably decrease the peak inrush current [1, 87].

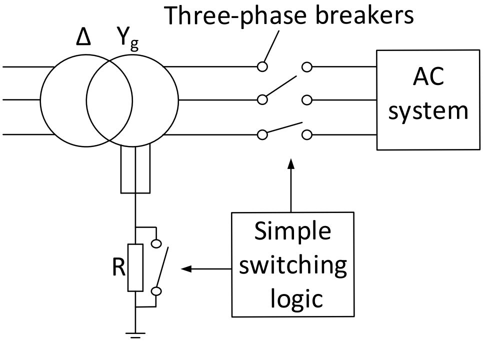

Figure 5.2: Scheme of neutral resistor with sequential switching strategy [1].

Compared to the pre-insertion resistor scheme, its simplicity and much more cost-effective, due to the existence of only one resistor, are the main advantages of this technique. However, the proper selection of the resistor size for optimal operation has not been completely solved and this methodology is limited to star grounded connected transformers and some specific non-earthed star connections [1, 87].

5.4.4 Residual flux reduction strategy

The phenomenon of transformer inrush current can be mitigated via the reduction of the residual flux in the core of the transformer. This implies that the magnitude of the residual flux in the transformer is one of the main parameters affecting the inrush current amplitude. Therefore, decreasing the amount of residual flux can reduce this current. The value of residual flux can be decreased using a capacitor mounted on the primary side of the transformer or using a low-power ultra-low-frequency voltage source [81].

5.4.5 Prefluxing strategy

Another strategy for inrush current reduction is the regulation of the transformer residual flux at a high amplitude and desired polarity and then, the transformer energization at an optimal point on the system voltage wave in accordance with the polarity of the residual flux. Hence, this process is called pre-fluxing technique [66, 2]. On the other hand, the pre-fluxing technique is implemented to feed some DC flux first, before transformers switching-on, so as to make inrush current reduction possible with closing circuits breakers [66, 2].

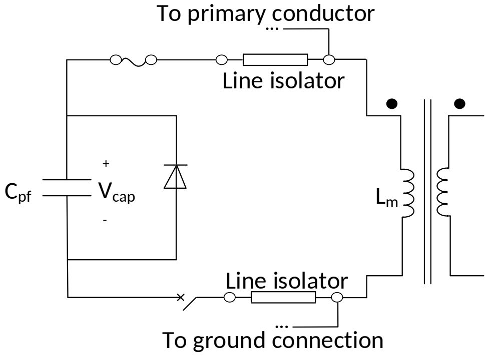

Figure 5.3: Prefluxing device [2].

The main benefit of this scheme over the other decrement schemes is that the pre-fluxing device (capacitor) adjusts the transformer flux to the desired value and consequently, it can make the transformer residual flux information unnecessary. The pre-fluxing device, which has a simple construction, only acts within the isolation term and afterwards, it is disconnected from the AC network according to energization. This results in another advantage over the methodology of the pre-insertion resistors [66]. Figure 5.3 illustrates the prefluxing device.

5.5 No application of inrush current reduction strategies on HVDC systems

The mentioned techniques for inrush current minimization depend on factors such as the switching instant of the Circuit Breaker (CB), data or computation of the residual flux in the transformer core, installation of large resistances, the connection type of the winding, the appropriate choice of resistor size and the model for CBs switching control. Therefore, the application of these schemes for inrush current reduction in HVDC systems entails higher costs, higher losses and more complexity.

Hence, due to the importance of the correct operation of the HVDC transmission system, especially the power converter, during energization and restoration of the power transformer as well as the economic and technical issues of the system, a simpler, highly efficient and more cost-effective technique to limit inrush current is required. This thesis proposes a new method called Voltage Ramping Strategy (VRS). The implementation of this proposed method is easier due to the fact that information of transformer parameters is not needed. In addition, the basic principle of this approach is the creation and regulation of ramp in the voltage across the transformers winding connected the power converter. Therefore, this strategy is implemented in the AC voltage controller of the HVDC converter in order to achieve lower inrush current and ensure that there is no interruption of the HVDC converter during inrush transient.

5.6 Dynamic model of transformer

The most common representation for a three-phase two-winding transformer which had been proposed by Steinmetz in 1897 is model based on a T-equivalent electric circuit [63].

This classical transient representation that considers winding connections (e.g., Y-Y or Y-Δ) and transformer losses is applicable to transformer transient studies. In other words, the transformer behavior during the energization of its iron core can be modeled by using a T-equivalent circuit. Since three-phase transformers applied in HVDC transmission systems are commonly constructed through three single-phase transformers with Y-connection on its primary side and the inrush current in each of the phases is different [88], the T-model is represented by the composition of three separate single-phase units containing the efficacy of the magnetic core saturation [89]. In addition, the saturation of the core is modelled by a current source in this scheme [73]. The topology for electrical equivalent circuit of a two-winding transformer is illustrated in Figure 5.4.

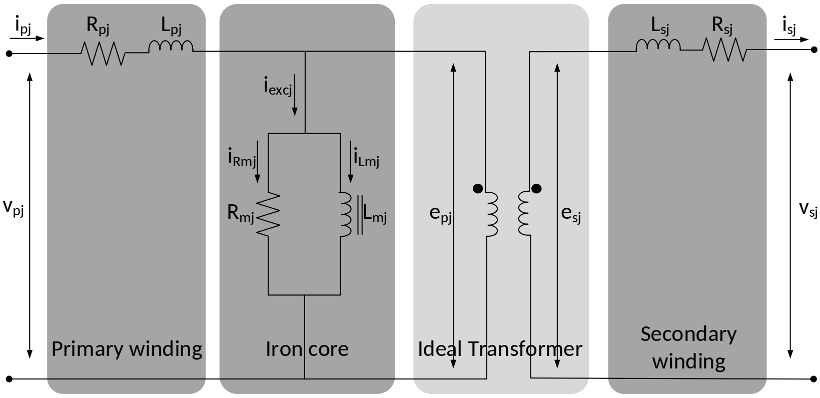

Figure 5.4: T-equivalent circuit model of a two-winding transformer.

In order to establish the T-model for a single-phase transformer, two main components, windings and the iron core, must be considered. Therefore, the winding resistances and leakage inductances, are defined for the transformer primary and secondary windings. The iron core behavior can be also modeled by means of a parallel excitation branch which is a parallel combination of a linear magnetizing resistance and a non-linear inductance, R_{mj} and L_{mj}, respectively [63, 90, 91].

The R_{mj} and L_{mj} indicate the core losses and the magnetic core saturation. Consequently, the iron core presents the non-linear behavior during the analysis of the transformer transients [91].

A model of three-phase two-winding transformer with a Y to ground- Δ connection can be derived from the electric circuit diagram shown in Figure 5.5.

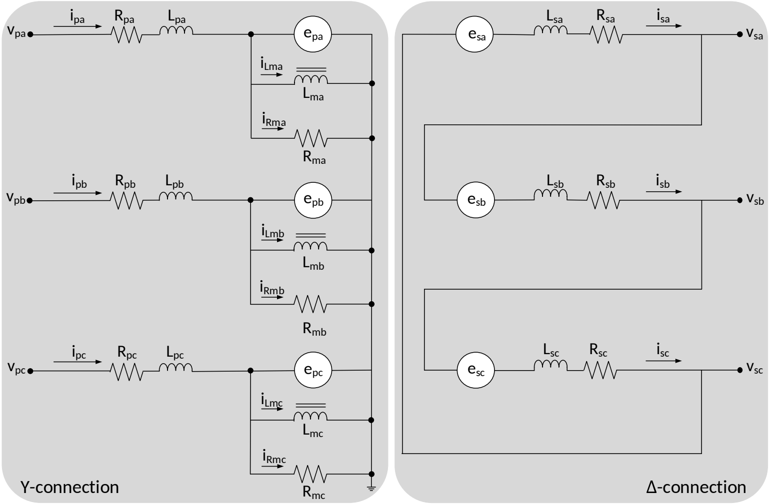

Figure 5.5: Electric circuit diagram of a three-phase two-winding transformer with a Y to ground-Δ connection [3].

5.6.1 Modeling of transformer primary winding

For the transformer primary windings, R_{pj} and L_{pj} present the winding resistance and leakage inductance for each of the transformer phases. These resistances and leakage inductances are linear [90]. The state equation describing the primary side of a three-phase transformer in Figure 5.4 can be expressed as follows [3]:

$$v_{pj} - e_{pj} = R_{pj} i_{pj} + L_{pj} \frac{di_{pj}}{dt} \tag{5.3}$$

where j denotes the corresponding phase, v_{pj} and e_{pj} show the primary terminals voltage and the voltage induced in the primary winding, respectively. The e_{pj} differs from v_{pj} due to the voltage drop across the winding resistance and the leakage reactance and it also lags the main flux by 90°. The i_{pj} represents the current in the primary windings.
Applying Laplace transform to Equation (5.3), the following formula can be written.

$$i_{pj} = \frac{1}{sL_{pj}} [v_{pj} - e_{pj} - R_{pj} i_{pj}] \tag{5.4}$$

Based on Equation (5.4), a block diagram for the transformer primary side can be shown in Figure 5.6.

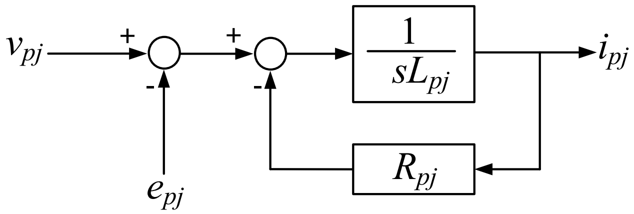

Figure 5.6: Block diagram for the transformer primary windings.

Furthermore, according to the equivalent circuit of Figure 5.4, the current of the primary side, i_{pj}, will consist of the excitation branch current, i_{excj}, plus the current component of the secondary winding, i_{sj}, [90]. So,

$$i_{pj} = i_{sj} + i_{excj} \tag{5.5}$$

5.6.2 Modeling of the iron core

Power transformer modeling considering iron core effects is an important issue to analyze the inrush current transients during transformer exciting and recovery. The reason for this is that the flux in the magnetic core reaches the limit of the saturation flux and consequently, leads to the saturation of the core. Then, this saturation influences the magnetizing current and finally, concludes to occur the inrush current. Hence, the transformer model must take into account the effect of the core saturation at the time of transformer energization and recovery. This is not enough for the model of the core, the consideration of the core losses composed of hysteresis and eddy-current losses is also required. In general, the representation of the transformer will be more practical due to the implementation of these impacts, however it becomes more wrapped [91].
Therefore, the iron core presents a non-linear behavior during the transformer transients due to the effects of saturation and losses of the transformer core. Hence, the non-linear operation of the core can be modeled in three methods: [92]

a) Linear resistor and nonlinear inductor.
b) Nonlinear resistor and nonlinear inductor.
c) Linear resistor and nonlinear hysteresis inductor.

In order to study inrush current transient, the method (a), which includes non-linear inductance (L_m) and linear resistance (R_m), is more commonly applied to model the non-linear iron core of transformer, due to its simplicity. In this method, the R_m and L_m are the core losses and the magnetic core saturation, respectively [92]. Moreover, the core model, as shown in Figure 5.4, is interfaced with a point of the T-equivalent circuit that the integral of the voltage is identical to the flux of the core [91].

According to Figure 5.4, current in the excitation branch, i_{excj}, is computed as follows [90]:

$$i_{excj} = i_{Rmj} + i_{Lmj} \tag{5.6}$$

where i_{Rmj} and i_{Lmj} denote the core losses and magnetizing currents, respectively.

In the representation of the transformer core, the magnetizing branch indicating core saturation can be modeled by a current source [60, 73], as illustrated in Figure 5.7. The magnetizing current presented by this current source depends on the total flux of the transformer core. In general, the total flux, ϕ_j, results from the sum of the integral of the induced voltage across the magnetizing branch, $e_{pj}(t)$, and the residual flux remained in the core, ϕ_{rj}, [3].

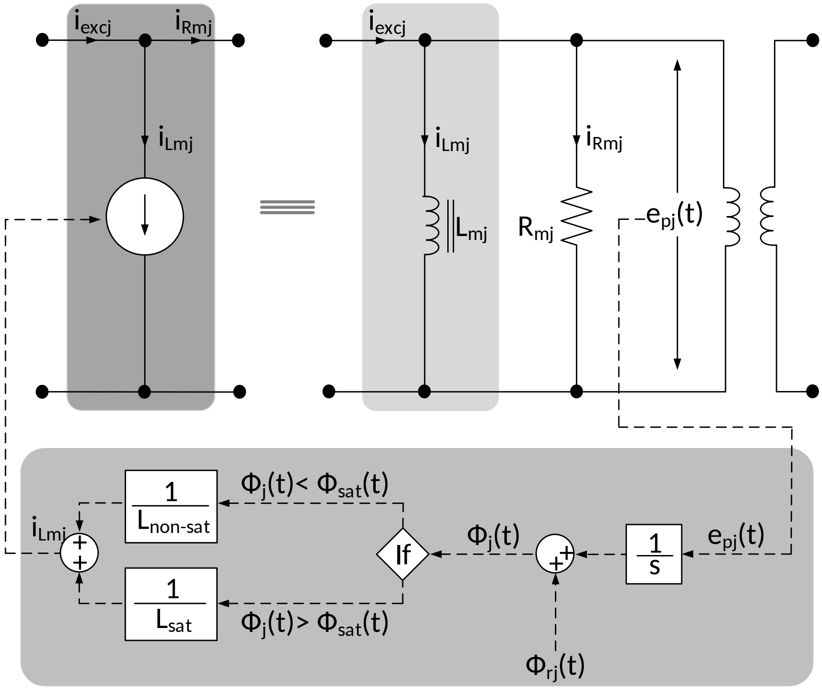

Figure 5.7: Equivalent model of a nonlinear inductor.

Thus,

$$\phi_j(t) = \int e_{pj}(t)dt + \phi_{rj} \tag{5.7}$$

In addition, the mentioned flux can be obtained based on the following expression [93]

$$\phi_j(t) = L_{mj} i_{Lmj}(t) \tag{5.8}$$

Substituting for $\phi_j(t)$ in Equation (5.7), based on Equation (5.8) and taking Laplace, the following relation can be deduced for the magnetizing current.

$$i_{Lmj}(s) = \frac{1}{L_{mj}}[\frac{1}{s}e_{pj} + \phi_{rj}] \tag{5.9}$$

where L_{mj} shows the magnetizing inductance. The magnetizing current is in time phase with its associated flux to excite the core. The block diagram of magnetizing current is shown in Figure 5.8.

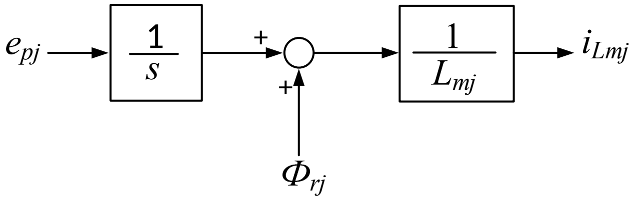

Figure 5.8: Block diagram of the magnetizing current.

For transformers with connection of Y-Y, the current of the magnetizing branch in each phase, i_{Lmj}, can be obtained through the reduction of the component of the core loss current, i_{Rmj}, from the primary winding current, i_{pj}, on the basis of Equations (5.5) and (5.6). Thus,

$$i_{Lmj} = i_{pj} - i_{Rmj} \tag{5.10}$$

It should be noted that in transformers with configuration of Y-Y, the current in the secondary windings is equal to zero [90].

The theorem of the magnetizing branch current in Y-Δ connected transformers is quite different. Figure 5.9 shows the equivalent electric circuit of a Y-Δ connected transformer which is excited from the star side.

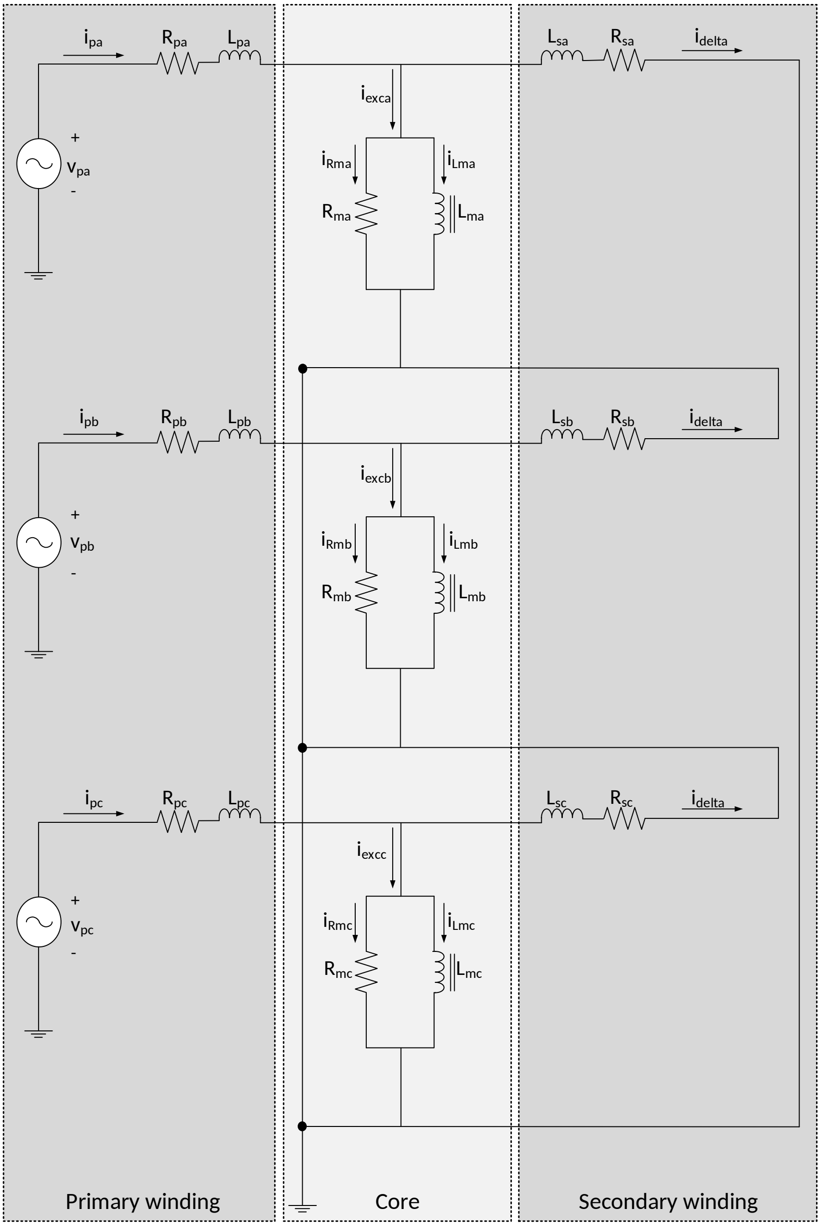

Figure 5.9: Equivalent electric circuit for a Y-Δ transformer [3].

Under no-load normal operation state, the transformer secondary terminals, which are in delta configuration, are not connected to the load. Therefore, the induced voltages across the windings with delta connection become almost balanced and the delta winding current can be considered zero [90].
However, when the three-phase transformer is energized, an unbalance may arise in the induced voltage. This implies that a high voltage collapse will take place in the leakage impedance of the primary winding. Hence, the unbalance of induced voltage results in the creation of a current in the delta winding [90].
Based on the T-equivalent circuit and supposing the secondary windings with delta connection, the computation of magnetizing current is as follows [90]:

$$i_{Lmj} = i_{pj} - i_{Rmj} - i_{delta} \tag{5.11}$$

The current of delta winding, i_{delta}, is related to the rate of flux changing.

A: Modeling of non-linear inductance:
Changing the non-linear magnetizing inductance, L_m, shows the essential feature of the iron core during the transformer energization and restoration, namely saturation and non-saturation of the transformer core [93]. This inductance can be defined using the curve of magnetizing characteristic, magnetic flux versus magnetizing current, $(\phi - i)$. The slopes of this magnetic curve represent the core magnetic inductance at the non-saturation and saturation modes [60, 73, 78, 93, 94].
Figure 5.10 shows the curve of magnetizing characteristic. During the steady operation of transformer, no saturation occurs in the magnetic core, namely $\phi < \phi_{sat}$, and the value of magnetizing current is low. Thus, in this mode, the core magnetizing inductance is located in the linear segment of the magnetizing characteristic curve and its content becomes equal to a stable value, L_{nonsat} [93].
However, when a transformer is switched on, the core flux exceeds the saturation flux, namely $\phi > \phi_{sat}$. Hence, the transformer core is driven into saturation and the inrush current will be generated, which results in the variation of the magnetizing inductance. On the other hand, the periodic saturation and non-saturation conditions of iron core in the transformer appear during the inrush current phenomenon. Therefore, the core saturation and the severe non-linear of the core lead to the variation of the magnetizing inductance of

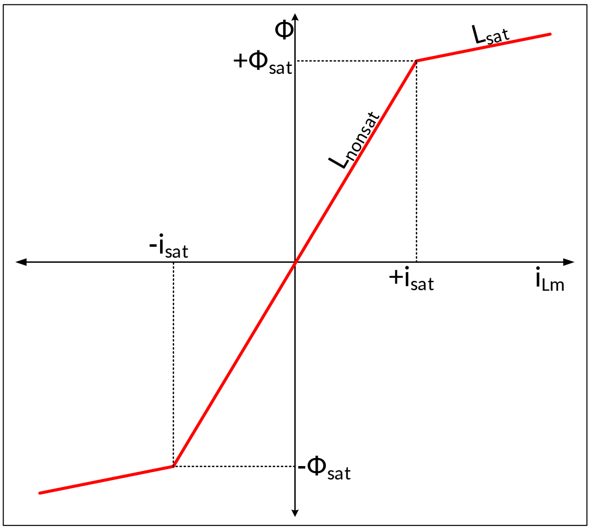

Figure 5.10: Magnetizing characteristic curve of a transformer.

the core from the linear region of the curve towards the non-linear region of curve. In fact, the value of this saturated core inductance will change from $L_{non-sat}$ to L_{sat} and subsequently, the magnetizing current becomes larger [93].

According to the air-core theory, the transformer iron core shows a behavior similar to that of the air with permeability μ_0 when the complete saturation of core is achieved [78]. Consequently, the amount of magnetizing inductance, L_{sat}, will be close to the air-core inductance value, depending on the saturation level. So, in case of saturation, it can be concluded that $L_{nonsat}{>}L_{sat}$ [78, 93].

The magnetizing inductance calculation in the nonlinear region, L_{sat}, needs the detailed knowledge of the core and the structures of windings. Since this data is not always available and the accurate estimation of the magnetizing inductance dependent on the core flux is really difficult, the non-linear inductance of the transformer core can be represented using piece-wise linearization of the non-linear characteristic curve, $(\phi - i)$ [92].

Therefore, in this study, the magnetizing characteristic curve of transformer, $(\phi - i)$, can be represented by a two-slope piecewise linear inductance. Namely, the inductance is characterized by two segments, L_{nonsat} and L_{sat}.

The two-slope magnetizing curve shown in Figure 5.11 is described by magnetizing currents, $i_{Lm} = [i_{Lm1},\ i_{Lm2},\ i_{Lm3}]^T$, and magnetizing fluxes, $\phi_j = [\phi_{j1},\ \phi_{j2},\ \phi_{j3}]^T$ [92].

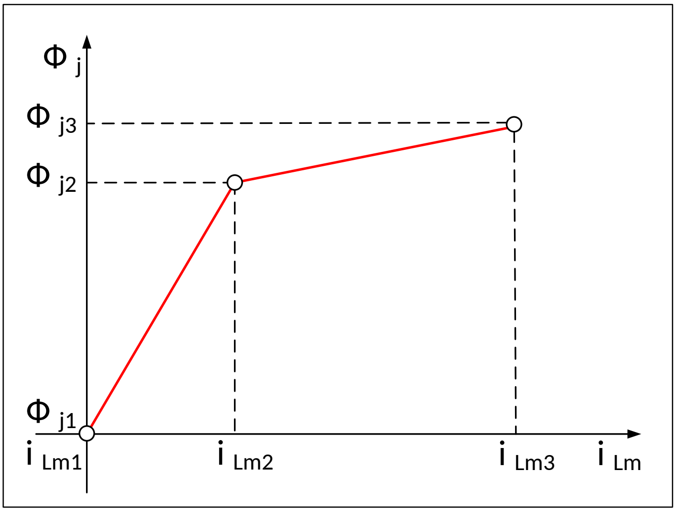

Figure 5.11: Two slope saturation curve.

This model of magnetizing inductance based on piecewise linearization of the non-linear characteristic curve is adequate to regulate the state-space expressions showing the transient behavior of the transformer during excitation or restoration.
The equation for magnetization inductance of the K_{th} $(k = 1, 2)$ linear segment of the foregoing curve is as the following: [92]

$$L_{mk} = \frac{d\phi}{di_{Lm}} = \frac{\phi_{k+1} - \phi_k}{i_{Lmk+1} - i_{Lmk}} \tag{5.12}$$

This Equation (5.12) is contingent on the situation of the operating region and its value is identical to the slope of the K_{th} linear segment of the magnetizing curve [92].
In order to determine the ϕ_k in Equation (5.12), the following formula is applied:

$$\phi_k = \frac{v_k}{\omega} \tag{5.13}$$

where ω is the angular frequency.

B: Modeling of linear resistor:
In order to model of the Hysteresis and eddy-current losses of the magnetic core, a linear resistance, R_{mj}, is considered [91]. In fact, this resistance is indicated with a fixed amount computed at the fundamental frequency of the induced voltage [90]. The Equation (5.14) can be used to calculate this linear component.

$$R_{mj} = \frac{e_{pj}}{i_{Rmj}} \tag{5.14}$$

where R_{mj} represents the linear resistance and i_{Rmj} shows the eddy-current of the respective phase.

5.6.3 Modeling of transformer secondary winding

Figure 5.4 shows that the transformer secondary windings are only composed of the resistance, R_{sj}, and the leakage inductance, L_{sj}, at each phase. According to the equivalent circuit of Figure 5.4, the generalized analytical expression for the transformer secondary winding can be deduced as

$$e_{sj} - v_{sj} = R_{sj} i_{sj} + L_{sj} \frac{di_{sj}}{dt} \tag{5.15}$$

where v_{sj} and e_{sj} are the voltage at the secondary winding terminal and the induced voltage in the secondary side by ideal transformer, respectively. Similar to the primary side of the transformer, the applied voltage, v_{sj}, differs from e_{sj}, in the voltage drop across the resistance and the leakage inductance of the secondary winding, represented in Figure 5.4. The i_{sj} represents the secondary winding current.

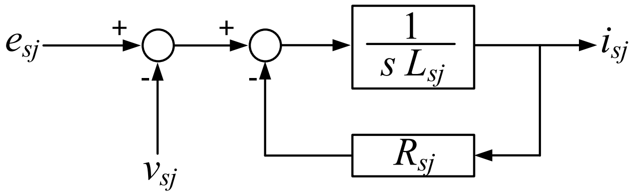

Figure 5.12: Block diagram for the transformer secondary windings.

Taking the Laplace transform from both sides of Equation (5.15), the Equation (5.16) and the block diagram of Figure 5.12 can be obtained.

$$i_{sj} = \frac{1}{sL_{sj}}[e_{sj} - v_{sj} - R_{sj}i_{sj}] \tag{5.16}$$

It should be mentioned that parameters calculation of the transformer equivalent circuit are described in Appendix C.

5.7 Simulation results

In this section, the inrush current transient of the power transformer energizing through a HVDC converter has been simulated by MATLAB/SIMULINK software. Here, the studied scenario is the inrush current analysis once the voltage applied to the transformer primary side in phase-a crosses the zero point, and the residual flux reaches the highest level. This mode produces the largest inrush current, which is called worst-case scenario of inrush current. Thereby, the dynamic model implemented for the transformer simulation has been manually initialized to the residual fluxes of (+0.94 pu, -0.94 pu, +0.84 pu) for phases a, b and c, respectively. Figure 5.13 sketches a simplified single-line diagram of case study. The characteristics of the transformer are summarized in Table 5.1.

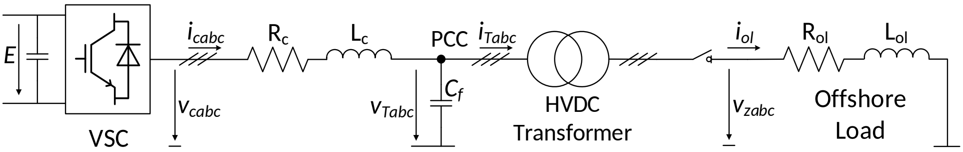

Figure 5.13: Single-line diagram of the case study.

5.7.1 Worst-case scenario of inrush current

Figure 5.14 indicates the inrush current of a 195/33 kV transformer and the voltage applied on the high voltage side of the transformer for energizing. In this case of study, the HVDC converter connected to the transformer is instantaneously energized and afterwards, the voltage at the transformer primary side, v_{Tq}, reaches a peak value of 159.22 kV at t=0, as shown in Figure 5.14 (a). Hence, voltage amplitude becomes stable. It should be noted that this value is kept constant by means of the AC voltage controller of the

Table 5.1: Transformer specification per phase

Parameter	Value	Unit
Nominal voltage	195/33	kV
Nominal current	1036.3/6123.4	A
Nominal power	350	MVA
Frequency	50	Hz
R_p/R_s	0.326/0.028	Ω
L_p/L_s	0.0484/0.0041	H
R_m	54321	Ω
Connection	$Y_n d_{11}$	-
ϕ_{sat}	$\approx 1.25\phi_n$	pu
ϕ_r	$\approx(+0.94, -0.94, +0.84)\phi_n$	pu

converter.

The inrush current waveforms measured on the high voltage terminal of the three-phase transformer are shown in Figure 5.14 (b). Regarding Figure 5.14 (b), it is obvious that inrush currents are higher than the rated currents. Moreover, it can be deduced that the shape and magnitude of the inrush currents depend on the voltage at the connection instant as well as the assumed amount of residual flux. Also, the zoomed plot of inrush current can be observed for a duration of 0.7s in Figure 5.14 (c).

In Figure 5.15, the magnetizing inrush currents, their zoomed view and the envelope of inrush current peaks are displayed for each of the transformer phases. These plots illustrate that the inrush current takes place when the transformer is magnetized to its nominal voltage (195 kV) through instantaneous switching of the VSC.

Initially, it is assumed that the residual fluxes in the core contain the maximum values, (+0.94 pu, -0.94 pu, +0.84 pu) for phases a, b and c, respectively and the transformer is energized at the instant that the voltage of phase-a is crossing the zero. Thus, the inrush currents obtained from MATLAB simulation are considered as a worst-case scenario. It should be noted

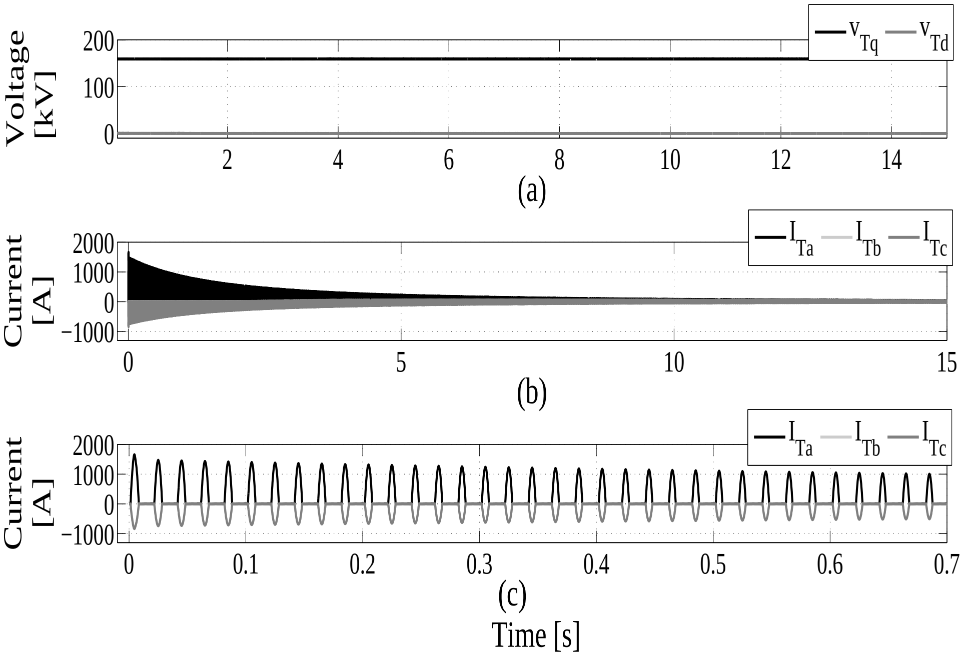

Figure 5.14: Inrush current and voltage of a transformer under worst condition. (a) The applied voltage at the transformer primary side. (b) Inrush current of a transformer for time duration 15s. (c) Inrush current for time duration 0.7s.

that the steady-state case will appear after a long time.

As shown in Figure 5.15, the highest peak inrush current is related to phase-a, the value of which reaches 1654.2 A in 4 millisecond after switching in phase-a. This implies that a high value of residual flux and the switching at the instant when voltage passes through zero influence the magnitude of inrush current. The maximum values of inrush current for the other phases, b and c are -824.52 A and -829.72 A, in accordance with the Figure 5.15. Moreover, two other conclusions can be stated corresponding to the Figure 5.15. The first one is that the inrush current waveforms include large and long lasting DC components. The second one is that the time necessary for the inrush current to drop to 50 % of its maximum value ($\tau_{50\%}$) is approximately 1.065s, 1.065s and 1.07s for phases a, b and c, respectively.

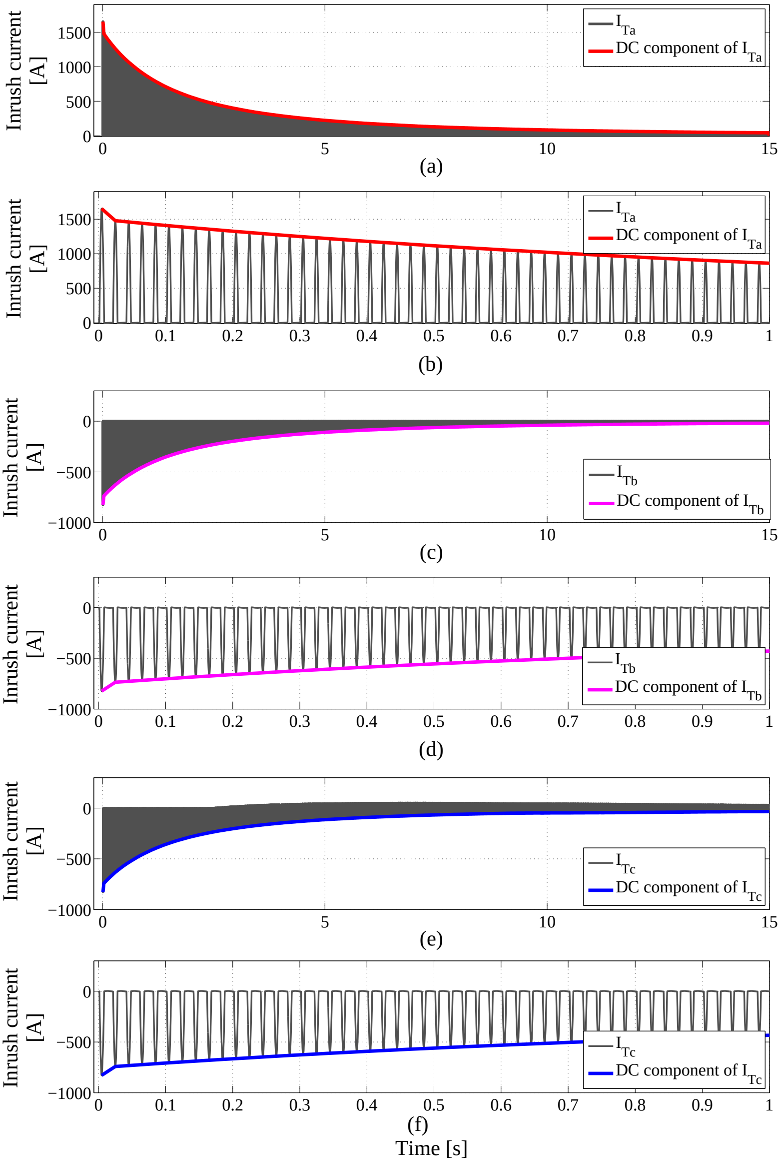

Figure 5.15: Simulation results of transformer inrush current for each phase during energization. (a) Inrush current of phase-a. (b) Zoomed of inrush current for phase-a. (c) Inrush current of phase-b. (d) Zoomed of inrush current for phase-b. (e) Inrush current of phase-c. (f) Zoomed of inrush current for phase-c.

The voltage waveform at the transformer secondary side during energization is demonstrated in Figure 5.16 (a). It can be observed that the voltage level has been changed from 159.22 kV to 26.944 kV through transformer relation. As shown in Figure 5.16 (a), there are small transients on the wave shape of the secondary voltage that are caused by the inrush current phenomenon which took place at the transformer primary terminal. It should be noted that these transients can be mitigated by inrush current reduction techniques.

The secondary current waveform of a three-phase transformer is also illustrated in Figure 5.16 (b). Current in each phase is approximately equal to zero, because the transformer is energized in no-load condition. Moreover, small fluctuations in the current waveforms can be seen due to the inrush transients.

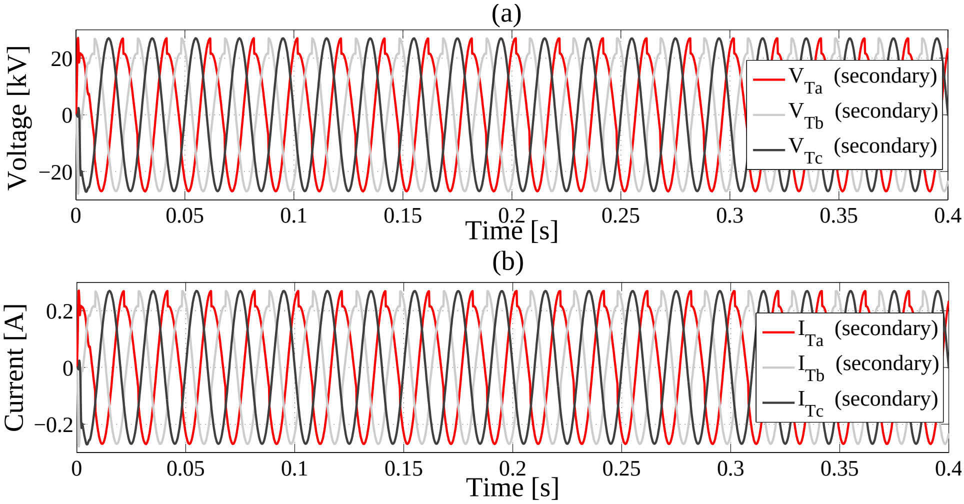

Figure 5.16: Secondary voltage and current waveforms of transformer during the energization. (a) The simulated voltage for 0.4s. (b) The simulated current for 0.4s.

The total flux of the magnetic core for each phase during the first 50 cycles is plotted in Figure 5.17. It can be seen that the total fluxes generated by the excitation of the no-load transformer start from the residual fluxes 476.39 wb, -476.39 wb, 425.71 wb for phases a, b and c, respectively.

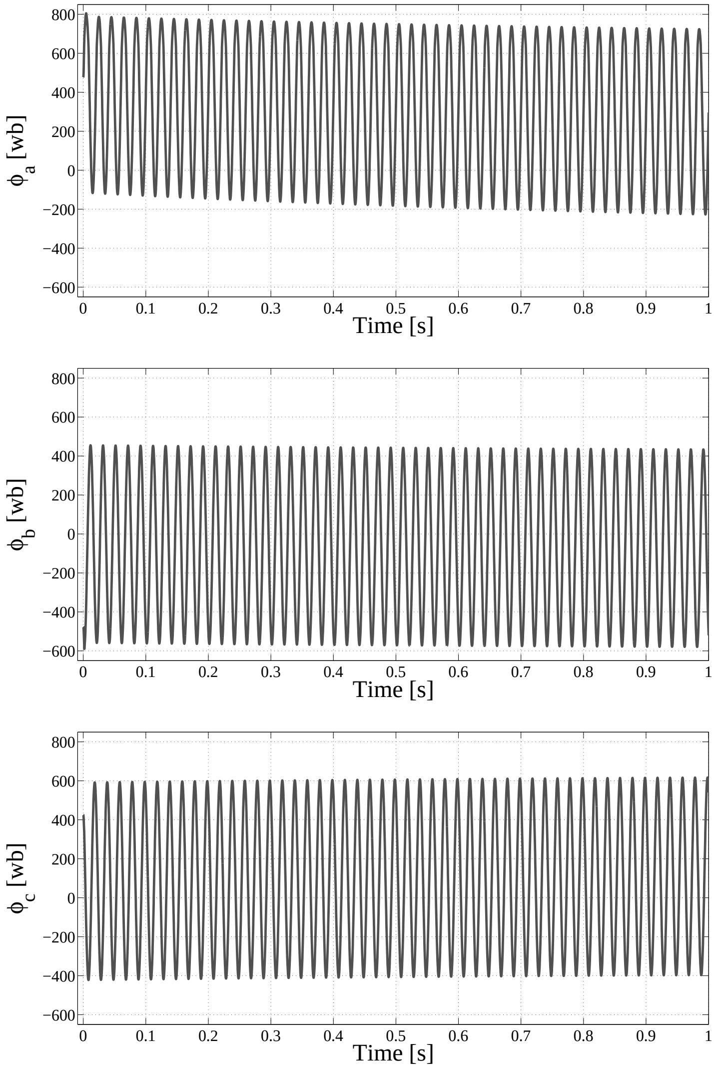

Figure 5.17: Total flux of transformer for each phase.

The currents of core loss, core saturation and excitation branches for each phase (i_{Rm}, i_{Lm} and i_{exc}) are represented in Figure 5.18. As shown, when the transformer is energized, the whole current passes through the core saturation branch, whereas a quite low current flows through the core loss branch. Therefore, the excitation current will be almost the same as the current of the core saturation branch. It should be noted that the flown current in the excitation branch can be neglected during the steady-state condition.

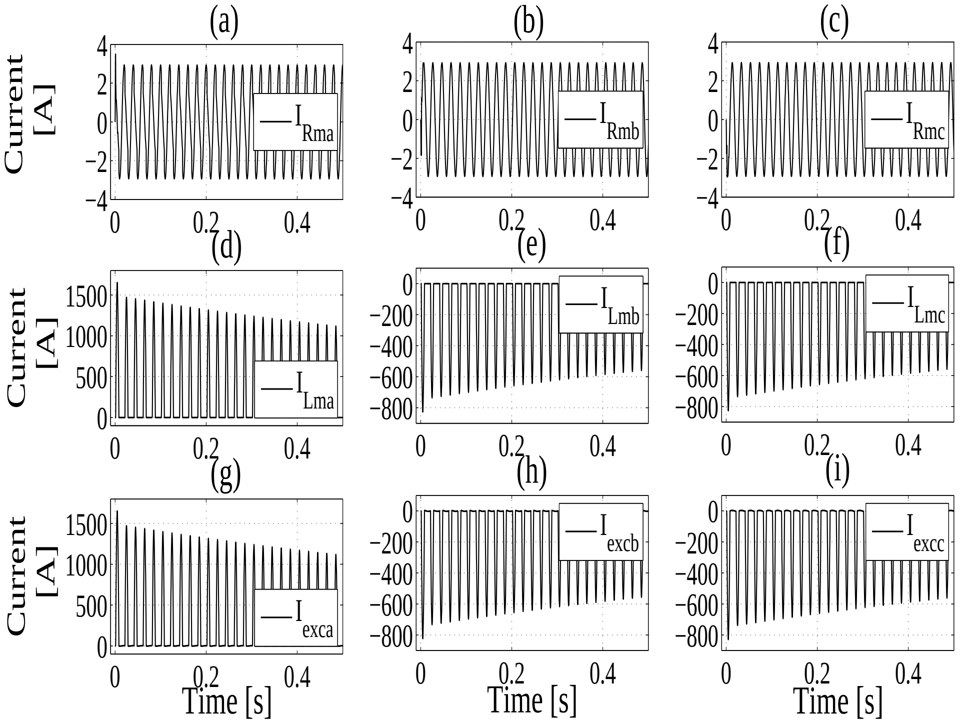

Figure 5.18: Currents of core loss, core saturation and excitation branches for each phase.

Since the windings of the transformer on the primary and secondary terminals are connected as $Y - \Delta$, third-harmonic currents circulate within the delta winding of the transformer. However, these currents, known as delta currents, are preventing the flowing in the supply line. Figure 5.19 shows a comparison between inrush and delta currents of an energizing transformer. The harmonic contents variations of the transformers transient inrush current with time for each phase are illustrated in Figure 5.20. The inrush current of transformer includes all the harmonic components such as fundamental, second, third, fourth, fifth, etc. and a DC component. These harmonic contents were obtained by means of a Discrete Time Fourier Transform (DTFT). Figure 5.20 shows that, the most significant harmonic components are fundamental and 2th order harmonics. For phase-a, their peak values are

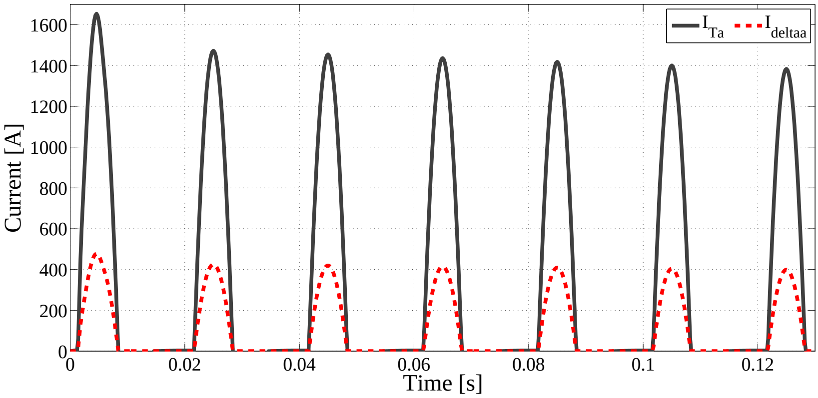

Figure 5.19: Comparison between inrush current of phase-a and delta current.

665 A and 452 A, respectively. The fifth harmonic current has a maximum value of nearly 61 A, nearly 7.5 times smaller than the second harmonic and nearly 10.5 times smaller than the fundamental component. These harmonics decay when the inrush current decays toward the steady-state mode. As shown in Figure 5.20, harmonics with higher orders of 3 have discontinuities. In other words, the peak values of these harmonics reduce to zero and then, increase again.

5.8 Summary

Transformer inrush current is a transient response to the magnetization that can exceed the nominal value of the transformer current and may be as intense as a short-circuit current. This transient inrush current, which is rich in terms of harmonics, has undesirable effects on the HVDC network. An important drawback of this inrush current in HVDC systems can be the disconnection of power converter, which can lead in turn to the interruption of the operation of the HVDC system. Consequently, the reduction of this current has become a main issue in the modern power industry.

Some technologies to limitat inrush current have been presented in this chapter. The application of these techniques in HVDC systems entails difficulties such as, requirement for the knowledge of residual flux, physical space requirements, low reliability and high costs. Therefore, this thesis will propose

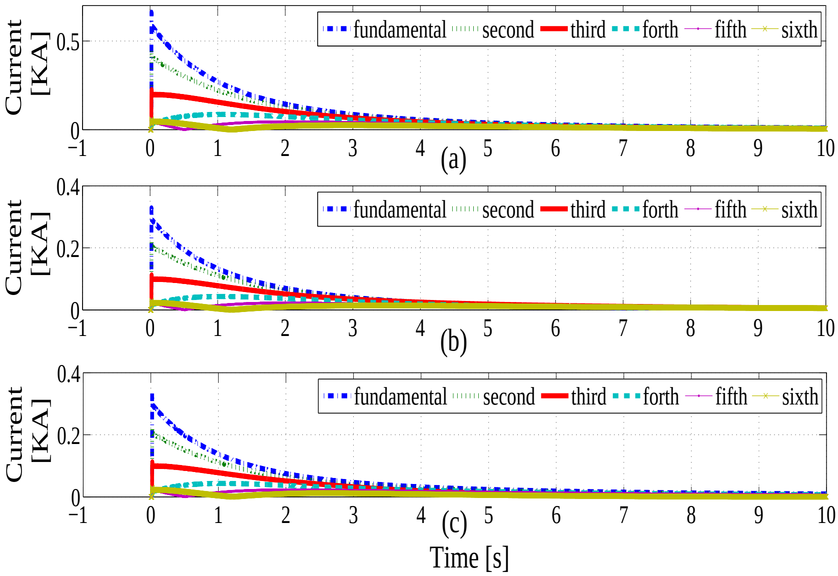

Figure 5.20: Harmonic content present in inrush current of: (a) Phase-a. (b) Phase-b. (c) Phase-c.

a novel approach in the next chapters which allows for the minimization of the inrush current of the transformer during the system start-up and restoration after fault clearance. Simulations have been carried out in order to show the worst-case scenario of inrush current.

Chapter 6

Energization inrush current reduction by proposed voltage ramping strategy during start-up and integration of offshore wind farm

The main scopes for this chapter are to develop a strategy for HVDC transformer inrush current reduction and control the offshore platform voltage, in order to provide a smooth start-up for offshore wind farm through the power converter of the HVDC transmission system. In addition, analysis of the start-up procedure of the offshore wind farm as well as a comparison between the performance of the proposed design and that of the system without the reduction approach can be mentioned as further objectives.

6.1 Introduction

The start-up of offshore wind farms through the HVDC systems in a stable and smooth mode is a significant issue. To achieve this target, there is the HVDC technology based on the Voltage Source Converter (VSC). In fact, the self-commutated VSC system can interconnect to the passive grid thanks to its black start capability and it can also generate a stable AC voltage at the offshore wind farm platform for start-up. This is due to the fact that the power electronic devices are utilized in VSCs. Therefore, VSC-based HVDC systems can facilitate the start-up of offshore wind farms and their integration into the onshore AC systems [95].

Furthermore, to coordinate the start-up of the VSC-HVDC system and the offshore wind farm system, a start-up procedure should be developed for the whole system. During the start-up process, transformers available in the power system, especially the HVDC transformer, will be switched-in and their energization often leads to the appearance of a large inrush current in the power grid. These currents containing harmonics can cause the dynamic overvoltages that lead to system instability. On the other hand, the voltage quality of Offshore Platform (OP) may be affected by the inrush current of the transformer in the HVDC system and the protection devices may be tripped. Hence, the existence of a method is essential for energization inrush current reduction of the transformer. A research work [19] has been carried out in the field of transformers inrush current minimization before the energization of doubly-fed induction generator offshore wind farms.

This chapter proposes a strategy, which is applied in the control system of offshore converter in the VSC-HVDC grid, to limit the inrush current during the transformer energization in the start-up process and also to improve voltage quality at offshore platform. This method is called Voltage Ramping Strategy (VRS) and is performed only for inrush current reduction of HVDC transformer.

This study is organized as follows: Section 6.2 describes the configuration of the offshore wind farm connected to the VSC-HVDC system, Section 6.3 analyzes the procedure of offshore system start-up and Section 6.4 introduces the proposed system. Simulation results are represented in Section 6.5 to prove the validity of the proposed method and finally, Section 6.6 draws the conclusions.

6.2 Analyzed system

The system under study contains a VSC-HVDC power converter interfaced with an offshore wind farm through an interface RLC filter and a power transformer in Y_g/Δ connection. The RLC filter composed of a series RL branch and a shunt capacitor (c_f) allows for the regulation of the HVDC transformer and offshore platform voltages. The power converter, called offshore converter, maintains stable voltage at the offshore platform. Figure 6.1 shows a simplified schematic diagram of the offshore wind farm connected to the offshore converter during the start-up condition.

The collection system for offshore wind farm is comprised several radial strings which collect wind turbines power and deliver it to the offshore platform. The radial strings are equipped with a number of wind turbines connected to each other by submarine cables and injecting the power into a 33 kV offshore feeder [96]. This chapter takes into account only four wind turbines from one string in order to facilitate the research on the offshore wind

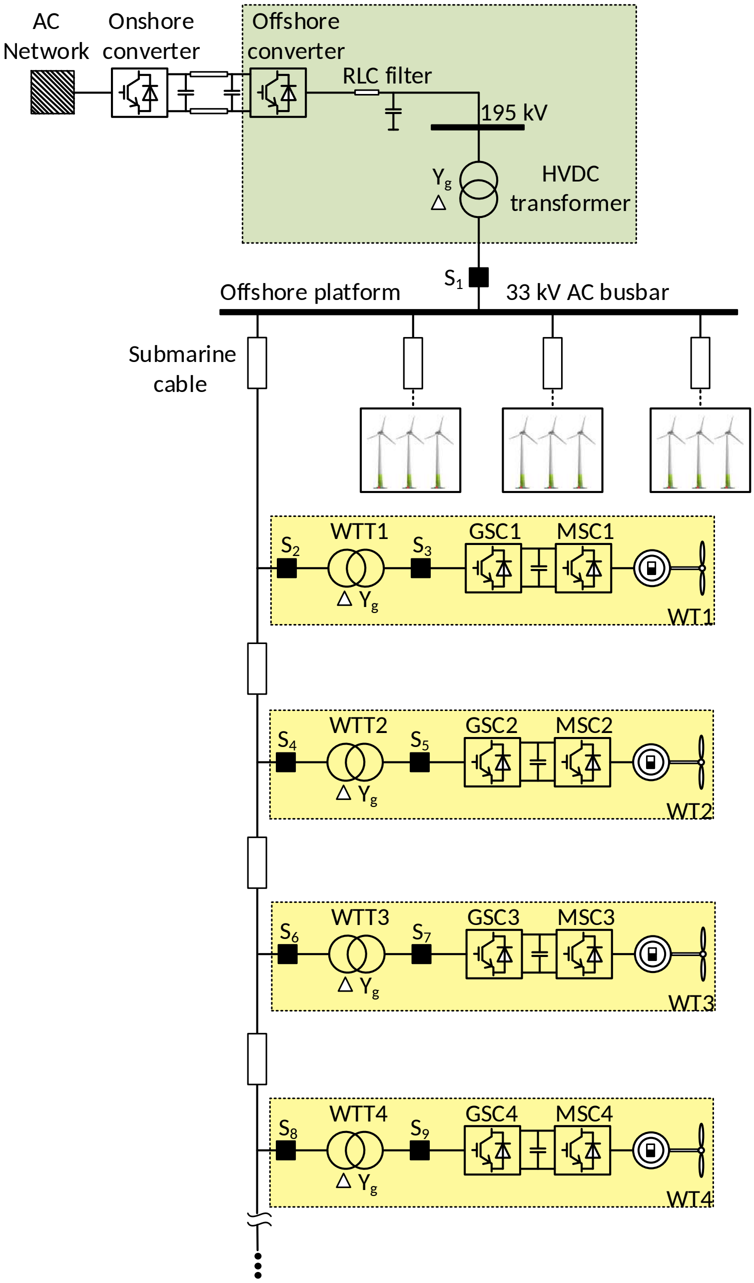

Figure 6.1: Single-line diagram of the system under study.

farm start-up.

Each wind turbine is presented as a Permanent Magnetic Synchronous Generator (PMSG, 5 MW) connected to a step-up transformer of 3.3/33 kV via the back-to-back converters (5.6 MVA). The wind turbines step-up transformer (WTT) is required to transform the generator voltage into the voltage of the offshore feeder. The back-to-back converters are employed to allow for the active power transmission under wind turbines start-up and normal operating conditions. The wind turbines converter that is confronted with the offshore grid is called Grid Side Converter (GSC) and the power converter faced with the electrical machine is called Machine Side Converter (MSC). The GSC is equipped with a DC-chopper that limits the DC voltage and dissipates the power that cannot be fed under AC fault condition [40].

6.3 Start-up procedure of an offshore wind farm along with inrush current reduction

The successful start-up of the offshore wind farm, its integration into an AC power network and the reduction of the HVDC transformer inrush current during the start-up can be achieved by means of the following process. Also, the flowchart of Figure 6.2 presents the sequential steps of this procedure.

6.3.1 Step 1: Start-up of offshore converter

To start-up the offshore wind farm and integrate it with AC grid, the energization of the offshore power converter in the HVDC transmission system is the first step. As the onshore converter is energized and the capacitors of DC link will be charged, the offshore converter will be able to operate under this DC voltage. Hence, the control system of offshore converter is activated to establish a stable nominal voltage at the HVDC transformer terminals as well as at the AC busbar of the offshore wind farm platform after closing switch S_1. The offshore converters controller actually provides the constant reference voltage in the AC busbar for energizing the offshore wind farm [95, 97].

In other words, when the offshore converter is energized in the beginning of the offshore grid start-up procedure, the converter AC side is faced with an open circuit and consequently, the active and reactive powers of the converter are close to zero [97]. In fact, the reason is that the offshore wind farm behaves like a passive load [98].

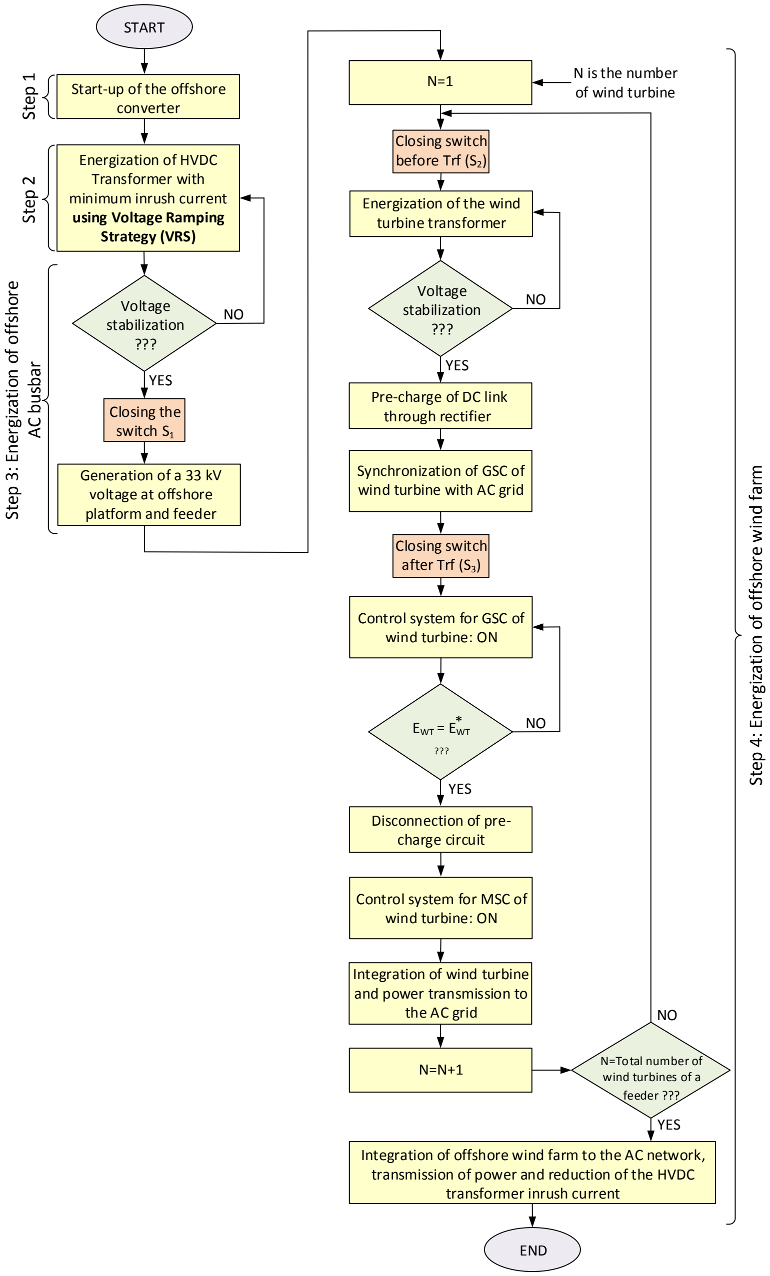

Figure 6.2: Flowchart of the offshore wind farm start-up procedure.

6.3.2 Step 2: Energization of HVDC transformer

The HVDC transformer is energized under no-load condition through the offshore converter. Once the offshore converter controller is activated, an abrupt voltage will induce across the high voltage terminal of HVDC transformer. This sudden increment of the transformer voltage may lead to transformer core saturation mode and consequently, the transformer will draw a large magnetizing current from the supplying network. This considerable current is named energization inrush current and its magnitude can reach several times the HVDC transformer rated current. Thus, the HVDC transformer connected to the offshore converter is started-up along with large inrush current, so that this current can affect the power quality of the offshore system and it also results in the inadvertent operation of protective devices. Thus, in order to energize the transformer with the minimum value of inrush current, a technique is required to design the control system of the offshore converter. For this reason, a new method, called Voltage Ramping Strategy (VRS), is introduced in this chapter (Section 6.4). The main objective of the proposed VRS is to restrict the HVDC transformer inrush transience before offshore wind farm start-up. Also, this strategy is employed only when the no-load transformer is being switched in.

6.3.3 Step 3: Energization of offshore AC busbar and feeder

After the transformer is energized and the voltage reaches the rated level, switch S_1 is closed to energize the AC busbar of the offshore wind farm platform. This implies that the offshore feeder will be switched on this way.

6.3.4 Step 4: Smooth start-up of the wind turbine

The first step of the wind turbine start-up is closing switch S_2 after the energization of the whole offshore feeder. Hence, the grid voltage suddenly exerted to the high voltage terminal of the transformer can lead to the saturation of the transformer core. Therefore, an inrush current can be drawn by means of the wind turbine transformer. The inrush current amplitude of the transformer is much lower than that of HVDC transformer. This indicates that the voltage level and reactance of the wind turbine transformer is lower in comparison with the HVDC transformer. After transformer energization and once the transformer voltage has reached the nominal level, the pre-charge of the wind turbines DC link can be started. This step is accomplished by a pre-charge circuit consisting of an uncontrolled diode rectifier in series with a resistor, R. The control block diagram of the aforementioned circuit is schematically illustrated in Figure 6.4. The operation procedure begins by closing switch S_{dc1}, followed by the connection of resistor, R, to the DC link in order to constrain the inrush current derived from pre-charging the DC link. The reason for using the resistor is that it is in charge of defining the DC link charge current and time constant. However, when the DC link is pre-charged and the DC voltage has reached the specified value, the resistor, R, is bypassed by closing S_{dc2} [99, 100].

With regard to the approach of DC voltage to the pre-defined threshold, the synchronization of the grid side converters voltage with the AC system voltage can take place. This synchronization is made by applying a PLL in the grid side converter system. Under such circumstance, the grid side converter system is oriented to the grid voltage. Once the synchronization is attained, the grid side converter can be connected to the wind turbine transformer by closing switch S_3. At this moment, the controller of the grid side converter will be automatically activated to govern the DC voltage and to ensure the power balance of the wind turbine system [101]. When the DC voltage is tuned to normal operational value, the circuit of the DC link precharge can be disconnected by opening switch S_{dc1} [99, 100]. During this operation mode, the grid side converter behaves as a rectifier and the power flowing is performed from the AC side to the DC side. In other words, no power can be transmitted to the AC grid until this step. Since the oscillations caused by the grid side converters connection to the grid disappear and the voltage of GSC is stabilized, the MSC is activated and then, power balancing in the DC link will take place. Therefore, the integration of the wind turbine into the AC grid is fully accomplished by connecting MSC to the system. As a consequence, the offshore converter can absorb the total power generated by the wind turbine and transmit it to the AC power system through the HVDC link. Further details regarding the control of the machine and grid side converters of the wind turbine can be found in Chapter 4.

In the start-up sequence of an offshore wind farm, the energization of each wind turbine is carried out only when the switching on and integration of the previous wind turbine is finished. In other words, when the first wind turbine (N=1) is started-up, the energization process of the second wind turbine (N=N+1) begins in a way similar to that of the previous wind turbine. This cycle continues to energize the entire wind turbines of one feeder. Therefore, in this case, the offshore wind farm is integrated into the AC grid and the active power generated by the wind farm is transmitted to the AC power network [98]. Finally, the offshore wind farm start-up and the minimization of HVDC transformer inrush current can be achieved by means of the foregoing procedure, as shown in Figure 6.2. Also, it should be mentioned that the DC link voltage of the wind turbine, in this study, is assumed to be charged.

6.4 Proposed Voltage Ramping Strategy (VRS) for inrush current decrement

To limit inrush current when the no-load transformer is energized by the offshore converter, the voltage ramping strategy is proposed. This methodology is performed by gradual increment of voltage on the high voltage terminal of the HVDC transformer from zero to nominal level. In fact, the inrush current reduction of the HVDC transformer is achieved by means of the generation of a ramp in the transformer voltage amplitude. Hence, this implies that the flux of the transformer being energized will not exceed the saturated knee-point of $(\phi - I)$ curve discussed in Chapter 5. Therefore, using this strategy, the peak inrush current can be minimized depending on the duration of the voltage ramp or the slopes value of the voltage ramp. Actually, enhancement of the period of ramp or reduction of voltage ramp slope can decrease the transformer inrush current amplitude.

The estimation of the ramp slope rate S_{VRS} is obtained based on the division of deviation of the transformer peak voltage amplitude $(v_T = v_{Tm})$ from its initial value $(v_T = 0)$ to the desired duration for ramp t_{ramp}. Namely, the calculation of voltage ramp can be achieved based on Equation (6.1).

$$S_{VRS} = \frac{\Delta v_T}{t_{ramp}} = \frac{v_{Tm} - 0}{t_{end} - t_{start}} \tag{6.1}$$

where t_{start} and t_{end} are instants of the ramp starting and finishing, respectively. Also, the characteristic curve of voltage ramp is illustrated in Figure 6.3.

Figure 6.4 depicts a VRS-based control structure for the offshore converter system that largely overcomes the aforementioned difficulties during the offshore grid start-up. Figure 6.4 shows that the assumption adopted in this method is $(v^*_{Tq}, v^*_{Td}) = (v^*_{Tq}, 0)$, where VRS is implemented for the $q-$axis component of the transformer reference voltage, v^*_{Tq}. Hence, v^*_{Tq} is adjusted based on the given ramp to ensure the reduction of the current. The control system of the offshore converter in Figure 6.4, as outlined in Chapter 3, comprises an inner current control loop and an outer voltage control loop. To perform the diminution of the peak inrush current under the transformer energization condition as well as to regulate the amplitude, frequency and

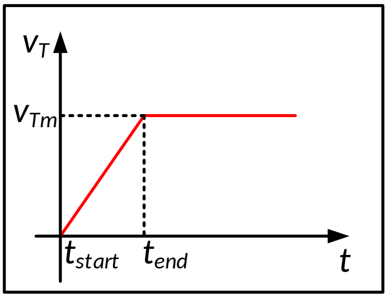

Figure 6.3: Transformer voltage ramp characteristic curve.

phase angle of the transformer voltage after the switching-in, Equations (6.2) and (6.3) are utilized for outer voltage loop.

$$i_{cq}^* = k_{olq}(s)(v_{Tq}^* - v_{Tq}) - \omega c_f v_{Td} + i_{Tq} \tag{6.2}$$

$$i_{cd}^* = k_{old}(s)(v_{Td}^* - v_{Td}) + \omega c_f v_{Tq} + i_{Td} \tag{6.3}$$

where i_{cqd}^* represents the qd-axis components of the reference current for the offshore converter, v_{Tqd}^* shows the qd-axis reference voltage components of the transformer, i_{Tqd} and v_{Tqd} denote the qd-axis components of the AC current and voltage at high voltage side of HVDC transformer.
Based on Equations (6.2) and (6.3), the transformer voltage in the qd frame is compared to the output signals of VRS, then the error signal is processed by compensators in qd frame, $k_{olqd}(s)$. Finally, with adding voltage decoupling feed-forward compensations ($\omega c_f v_{Td}$ and $\omega c_f v_{Tq}$) and current feed-forward compensations (i_{Tq} and i_{Td}), the command of current in qd frame (i_{cq}^* and i_{cd}^*) is issued for the corresponding $q-$ and $d-$axes current control loop. Thus, the two outputs of the inner current control loop, as shown in Figure 6.4, can control i_{cq}^* and i_{cd}^* according to

$$v_{cq} = k_{ilq}(s)(i_{cq}^* - i_{cq}) - \omega L i_{cd} + v_{Tq} \tag{6.4}$$

$$v_{cd} = k_{ild}(s)(i_{cd}^* - i_{cd}) + \omega L i_{cq} + v_{Td} \tag{6.5}$$

where v_{cqd} is voltage at the offshore converter AC side, k_{ilqd} presents two simple proportional-integral regulators and i_{cqd} is the qd-axis current components of offshore converter.

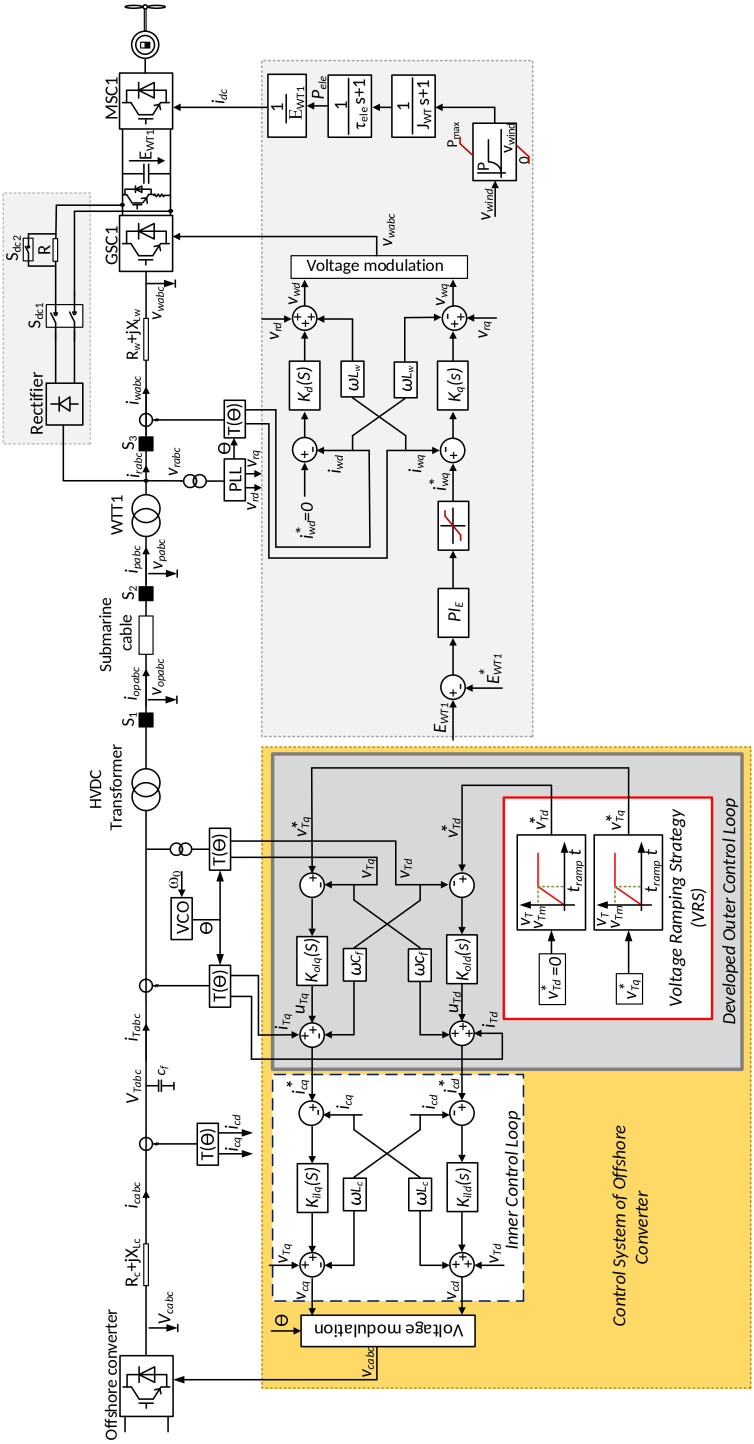

Figure 6.4: Proposed control structure for the offshore converter.

6.4.1 Advantages of the proposed voltage ramping strategy

The most significant benefits of the proposed technique are the considerable decrement of transformer inrush current, accurate operation of HVDC converter during energizing condition and high power quality. In addition, this strategy ensures much lower inrush currents for slower ramps. The other advantages of this method are cost-effective and straightforward implementation in the voltage regulator of offshore converter connected to transformer.

6.5 Simulation

In order to validate the proposed reduction strategy and perform the start-up of offshore grid, two case studies have been simulated using MATLAB/ Simulink package. The system comprises an offshore wind farm of four wind turbines and a voltage source converter of HVDC transmission system. Wind turbines based on PMSG are supposed to encounter the same wind profile. Transformers are modeled according to the T-equivalent circuit.

The first case simulates the HVDC transformers behavior during energization without applying the voltage ramping strategy for inrush current restriction. This will imply, in turn, that there is a high peak of current in the high voltage side of the transformer. The second case analyzes the effects of the proposed strategy on the inrush current of the HVDC transformer as well as the sequences of the start-up of the whole offshore system. The voltage ramp starts at t=0 s and its duration takes into account 100 s. The characteristic parameters utilized in the simulation are:

- HVDC transformer parameters: Y_g/Δ, 195/33 kV, S=350 MVA, R= 0.003 pu, L=0.14 pu, ϕ_r=(+0.94,-0.94,+0.84) pu, ϕ_{sat}=1.25 pu.

- Wind turbine transformer parameters: Δ/Y_g, 33/3.3 kV, S=5.56 MVA , R=0.006 pu, L=0.06 pu, ϕ_{sat}=1.1 pu, ϕ_r= (+0.8,-0.8,0) pu.

- PMSG parameters: V_n=3.3 kV, P_n=5.26 MW, PF_{grid}=0.9 inductive.

- Offshore HVDC converter parameters: V_{ac}=195 kV, S_n=350 MVA, R_c= 1.6296 Ω, L_c=51.9 mH, c_f=2.93 μF.

- Wind tubine parameters: ρ=1,225 Kg/m^3, R=58 m, $n_{nominal}$=14.8 min^{-1} , P_n=5 MW, E_{WT}=6 kV, c_{dc}=1400 μF, R_{WT}=0.0235 Ω, L_{WT}=0.75 mH, ϑ_{pitch}=0°, J_{WT}=1.7 s, τ_{ele}=0.01 s, c_1=0.5, c_2=116, c_3=0.4, c_4=0, c_5=0, c_6=5, c_7=21, c_8=0.08, c_9=0.035.

- Submarine cable parameters: R=0.06 Ω/km, L=0.36 mH/km, c= 0.26 μF/km, d=2.8 km.

6.5.1 Case study 1: HVDC transformer energization without the voltage ramping strategy

In this case, the HVDC transformer is switched in through an offshore power converter without employing the inrush transient reduction method, VRS. Therefore, as observed in Figure 6.5 (b), a high inrush current is drawn by the HVDC transformer, which is due to the sudden energizing by the offshore converter (shown in Figure 6.5 (a)). The amplitude of this inrush current for phases a, b and c is +1654.36 A, -824.55 A and -829.8 A, respectively. The value of peak inrush current for phase-a is 1.6 times higher than the nominal

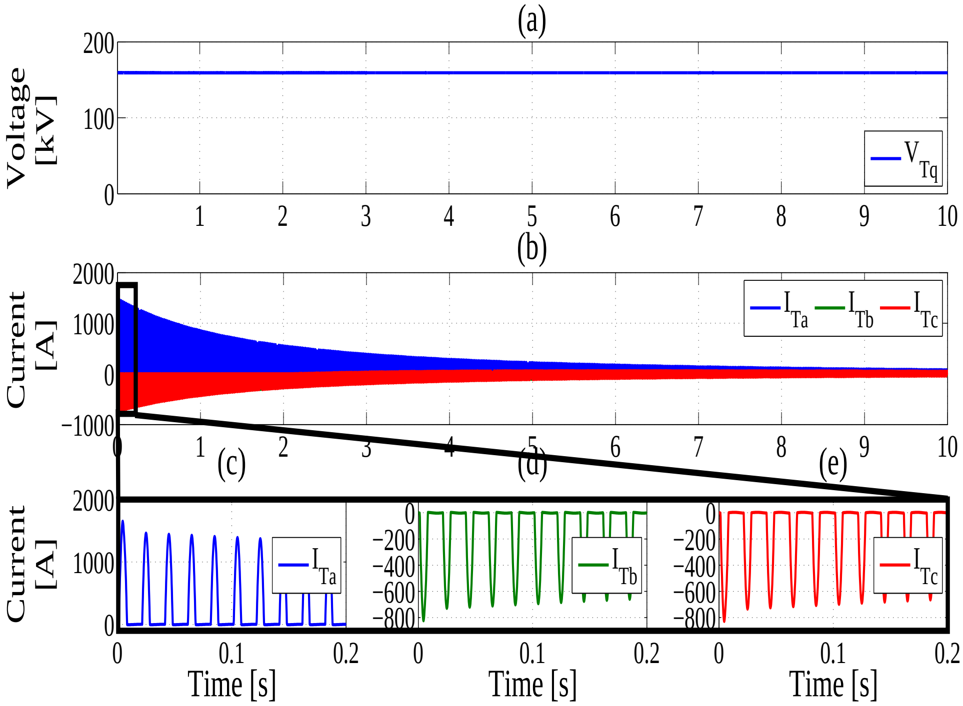

Figure 6.5: Simulation results of HVDC transformer switching-in without using voltage ramping strategy. (a) Voltage at the high voltage side of HVDC transformer. (b) Inrush current of transformer. (c) Zoomed of inrush current for phase-a. (d) Zoomed of inrush current for phase-b. (e) Zoomed of inrush current for phase-c.

current value of the transformer. Here, the offshore platform is not disconnected during transformer switching. However, as soon as the inrush current decays, the offshore platform is energized and consequently, the start-up of the offshore wind farm will begin. The worst case scenario of residual flux (+94%, -94%, +84%) was implemented in the transformer in order to be energized.

6.5.2 Case study 2: Decrement of HVDC transformer inrush current using VRS and start-up of the offshore grid

A. Energizing of the HVDC transformer by VRS:

This mode simulates the start-up of the HVDC transformer with the implementation of the voltage ramping strategy in the offshore converter. In this case, the voltage is ramped up from zero to the peak value (159.22 kV) with a ramping time (t_{ramp}) of 100 s, as shown in Figure 6.6 (a). Depending on the duration of the ramp, the reduction amount of inrush current changes. As illustrated in Figure 6.6 (b), the inrush current, corresponding to t_{ramp}=100 s, is considerably decreased.
The comparison between the values of the peak inrush current magnitude of the transformer in energization cases with and without using the proposed strategy will reveal the significant influence of this method, as it can be seen in Figures 6.6 (c)-(e) as well as in Table 6.1.

Table 6.1: Comparison of peak inrush currents for two cases.

Magnitude of inrush current	Phase-A (A)	Phase-B (A)	Phase-C (A)
Without VRS	1654.34	824.55	829.8
With VRS	100.423	125.1	169.3

The results obtained from Table 6.1 show that the largest decrease in the transformers inrush current appears in phase-a. On the other hand, the degradation of current for phases a, b and c is nearly 93.93%, 84.83%, 79.6%. Moreover, it can be observed in Figures 6.6 (b)-(d) that the steady-state case

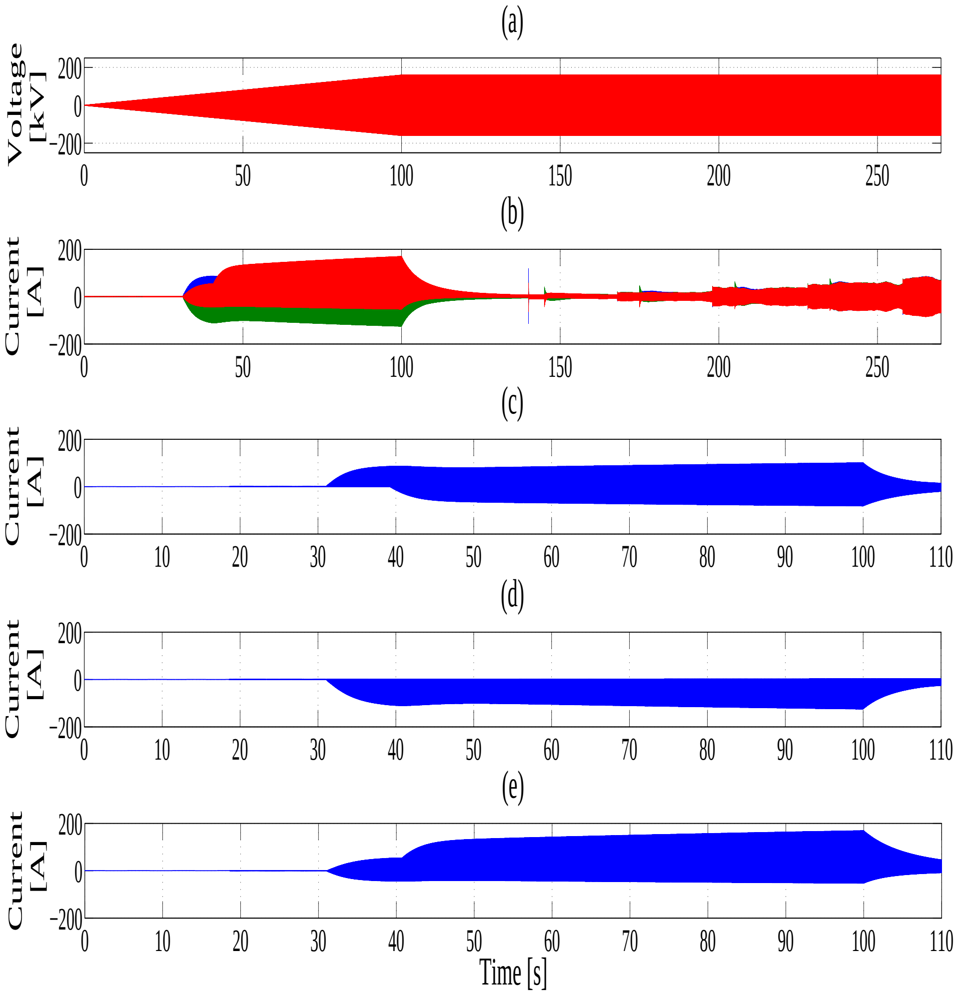

Figure 6.6: Simulation results of HVDC transformer energization with using voltage ramping strategy. (a) AC voltage of transformers high voltage side. (b) Inrush current of transformer. (c) Zoomed of inrush current for phase-a. (d) Zoomed of inrush current for phase-b. (e) Zoomed of inrush current for phase-c.

of the transformer is almost reached at t=140 s and the switching operation of offshore platform is accomplished by closing S_1 at this moment. Thereafter, the wind turbines prior connected to the switching into the offshore grid establish small effects on the steady-state condition of HVDC transformer.

Figure 6.7 shows the reduction of the peak inrush current for different phases of the HVDC transformer when the duration of the voltage ramp (t_{ramp}) is increasing. As can be observed in Figure 6.7, in the beginning, the transformer is excited in the instant t=0 s and the phase-a of the transformer has the highest value of peak inrush current (1654.34 A). Afterwards, the transformer is switched on by the voltage ramping strategy, and t_{ramp} is considered as 10 seconds. This time becomes identical to the slope of the voltage ramp, S_{VRS} = 15.922 kV/s. In Figure 6.7, it can be observed that the ramp time increases to 100 seconds or the slope is decreased to a lower value, S_{VRS} = 1.5922 kV/s. Therefore, as illustrated in Figure 6.7, increasing the duration or decreasing the slope of the voltage ramp leads effectively to a peak current reduction. In fact, the proposed voltage ramping strategy provides a more appropriate response in case of voltage ramps with slower slope. Hence, the optimal selection of the voltage ramp slope can significantly decrease peak magnetizing currents. In addition, the peak inrush current reduction for phases b and c are represented in Figure 6.7.

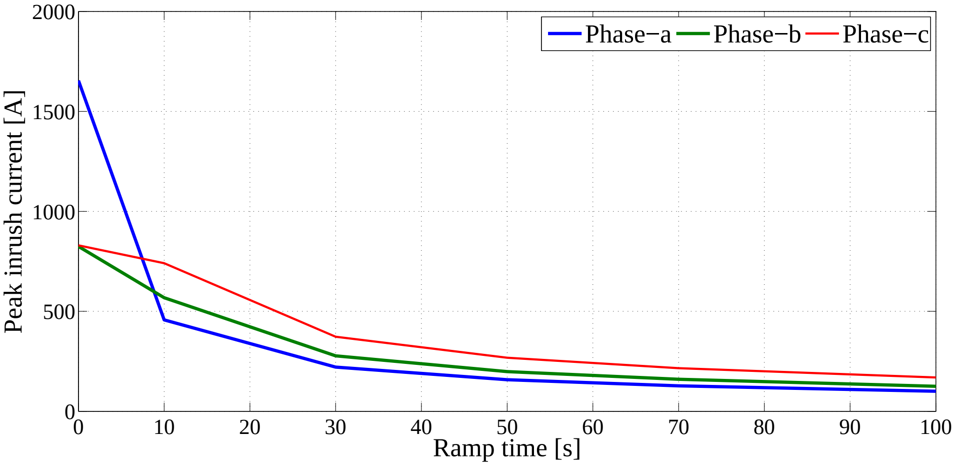

Figure 6.7: Peak inrush current reduction versus the different ramp times (for phase-a,b and c).

B. Start-up of the offshore platform and feeder:

Figure 6.8 indicates the voltage and current of the offshore platform during offshore grids start-up. As it can be seen, points (1) to (5) are the main operation steps. Actually, point (1) shows the energizing of the offshore platform and feeder by means of the power converter and closing switch S_1 at t=140 s. However, in this mode, a 33 kV voltage is provided at the offshore platform (AC busbar) and the entire feeder composed of three parallel submarine cables, the value of current is almost zero. When the voltage becomes entirely stable, the consecutive start-up and integration of each of the four first wind turbines can be performed corresponding to points (2) to (5). These points show the performance of the first wind turbine from the feeder till the last one, respectively.

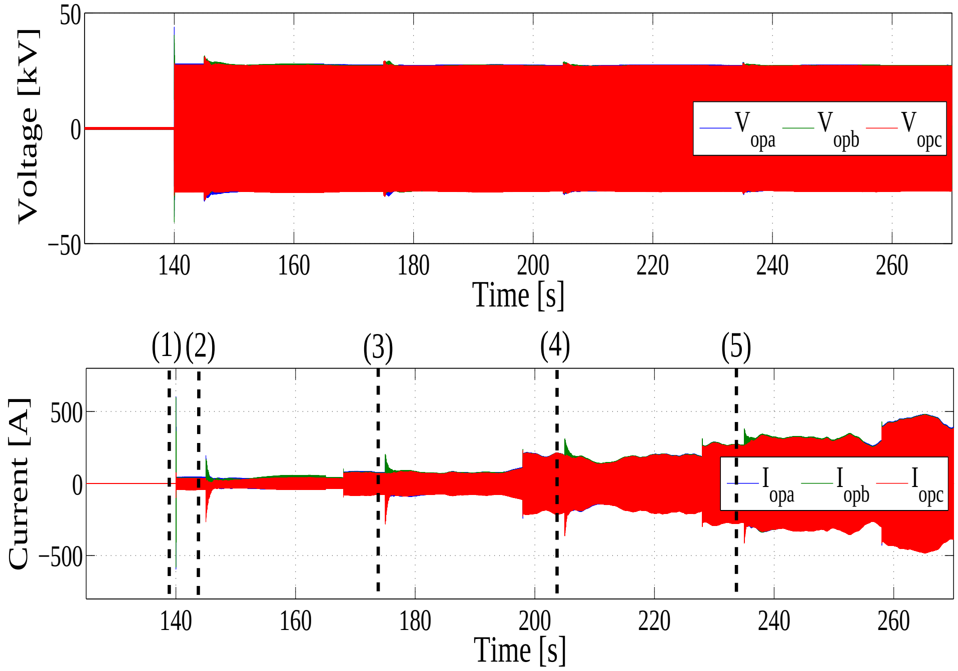

Figure 6.8: Simulation results for offshore platform during the wind turbines start-up process.

As shown in Figure 6.8, in spite of the inrush transient existence in the current of the offshore feeder, slight deviations from sinusoidal waveform of voltage are observed. These are due to the harmonics generated by wind turbines transformers. Furthermore, an enhancement in peak inrush currents at the moment of wind turbines transformer energization can be seen in the total current of the offshore feeder which entirely conflicts with the values of the peak inrush currents of each wind turbine. This is due to the fact that the current of the offshore feeder results from the sum of the currents of the whole wind turbines. Figure 6.9 represents the current of the offshore feeder for different phases a, b and c.

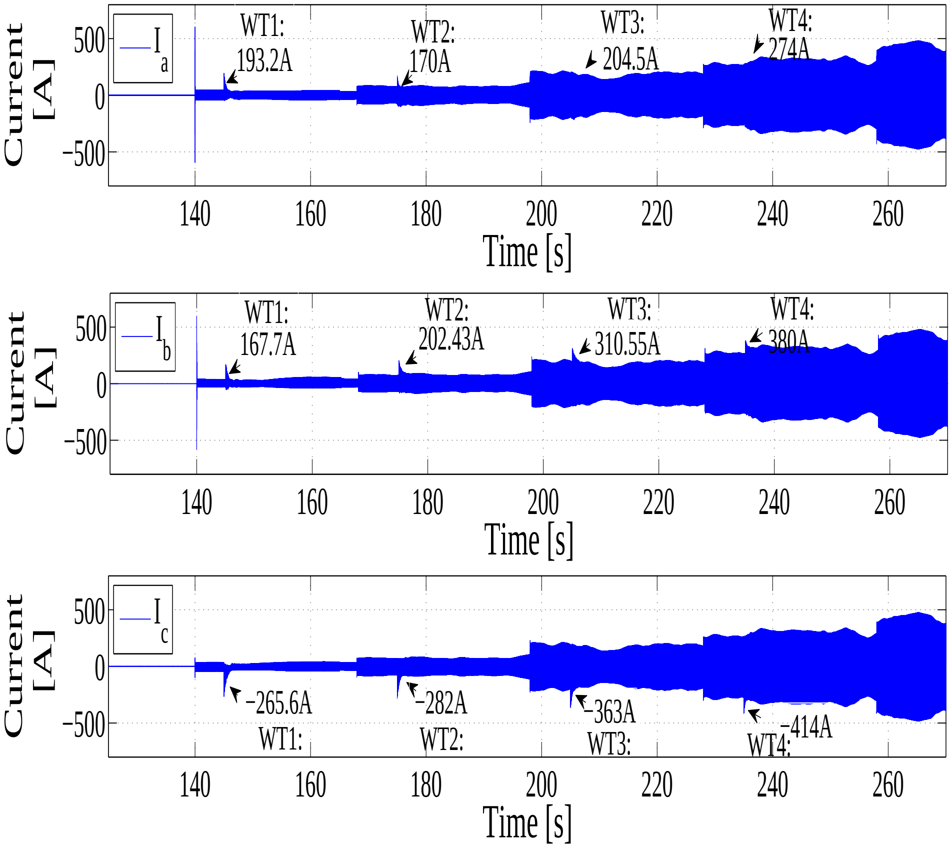

Figure 6.9: AC current of offshore feeder for phases-a, b and c.

Maximum AC overvoltage due to transformer energization in each wind turbine is presented in Table 6.2.

Table 6.2: The value of overvoltage at transformer high voltage side of each wind turbine.

Wind turbine	1	2	3	4
Overvoltage (%)	16.54	8.64	7.3	6.1

C. Start-up of the first offshore wind turbine:

At the beginning of the first wind turbine start-up, all converters of the wind turbine (GSC_1 and MSC_1) are blocked and there is voltage stability at the offshore platform. Nevertheless, there are no voltages at the wind turbine and DC link of converters. When the first wind turbine (WT_1) based on PMSG is started-up by closing S_2 at the moment of $t = 145$ s, a 33 kV

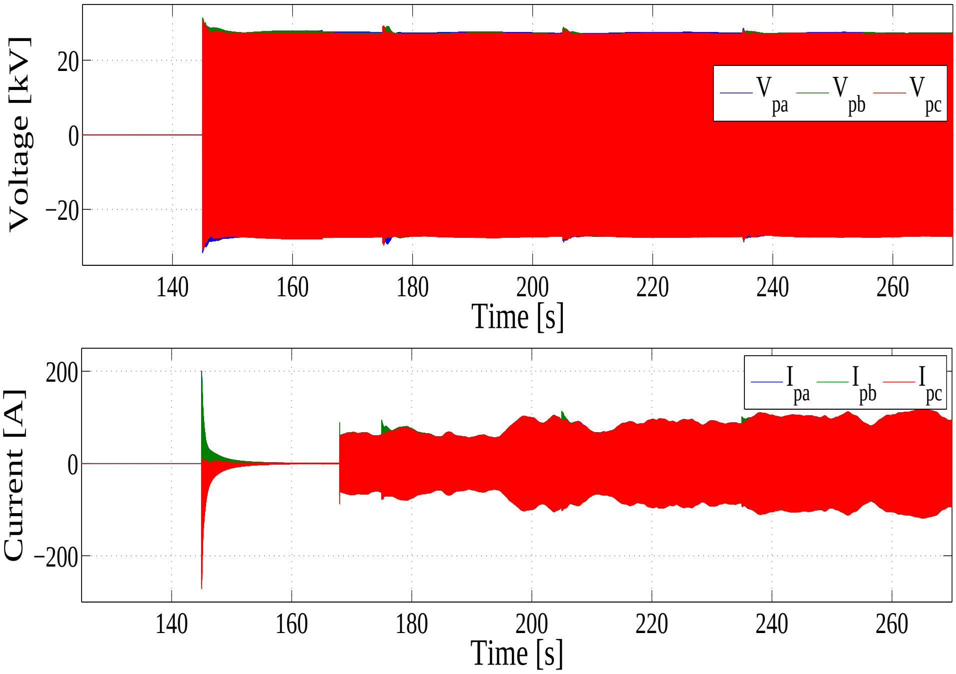

Figure 6.10: Voltage and current of MV side of WTT_1 during start-up procedure of the offshore grid.

voltage is generated across the MV and LV terminals of the transformer. On the other hand, this voltage in turn results in the inrush current occurrence at the transformer MV side, as indicated in Figure 6.10, and this current is damped around $t = 163$ s. In addition, it can be noticed in Figure 6.10 that this inrush current including harmonics leads to the overvoltage phenomena in the 33 kV voltage of the transformer and the offshore feeder during the energizing of the transformer.

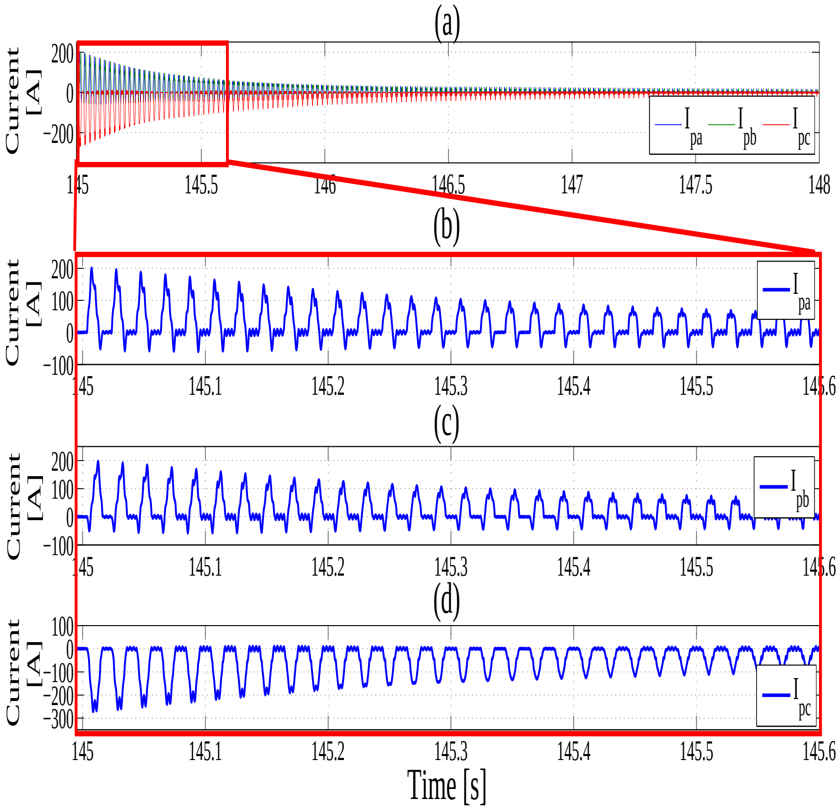

Figure 6.11: Inrush current of the first wind turbines transformer during energization. (a) Three-phase inrush current. (b) The simulated inrush current of phase-a. (c) The simulated inrush current of phase-b. (d) The simulated inrush current of phase-c.

The simulation result for the transformer inrush current of the wind turbine at the beginning of the feeder and also zoomed current for each of the phases are shown in Figure 6.11. The peak current magnitude for phases a, b and c are +200.4 A, +196.6 A, -271.4 A, respectively. Furthermore, in Figure 6.11, the decrement of inrush current cannot be seen, since no approach is applied for the reduction of this phenomenon.

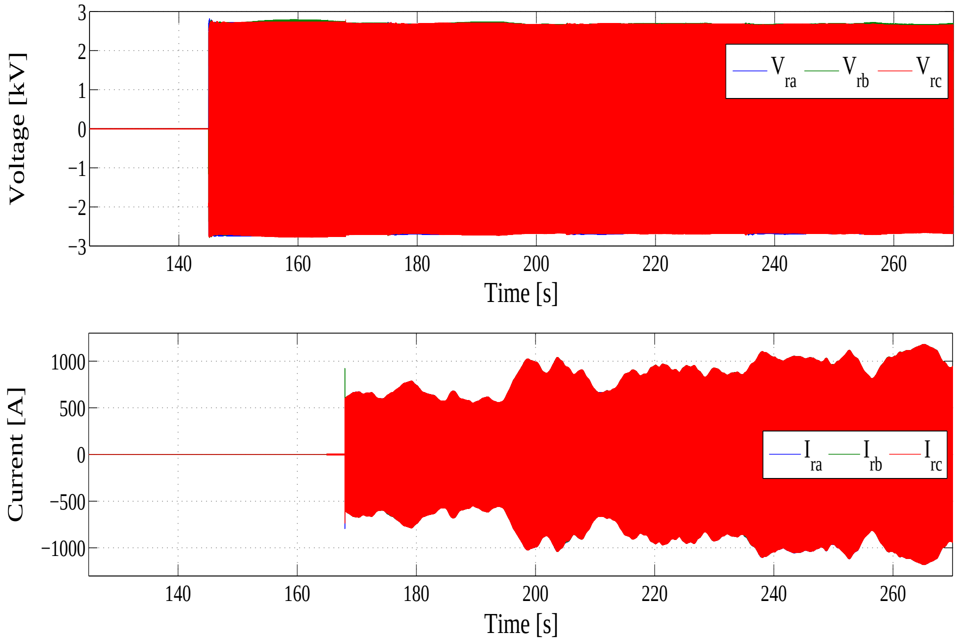

Figure 6.12: Voltage and current of WTT_1 LV side during start-up procedure of the offshore grid.

It can be clearly observed from Figure 6.12 that the voltage of the offshore network has been reduced by the transformer from a value of 33 kV to 3.3 kV, but the currents value on the transformer LV side is also zero. This is due to the fact that the transformer is energized in the no-load condition and the inrush transient only occurs at the MV terminal of transformer. When the inrush current decays and voltage of DC link is pre-charged, the synchronization of GSC_1 is conducted by PLL. In fact, the voltage of GSC_1 is tuned to match the voltage on the transformer LV side. Finally, once the synchronization operation is carried out, the switch S_3 is closed at the instant of t=165 s and the control mode for GSC1 is switched to DC voltage regulation. Figure 6.13 illustrates the integration of WT1 to the offshore grid that has been obtained by means of the activation of the machine side converter (MSC).

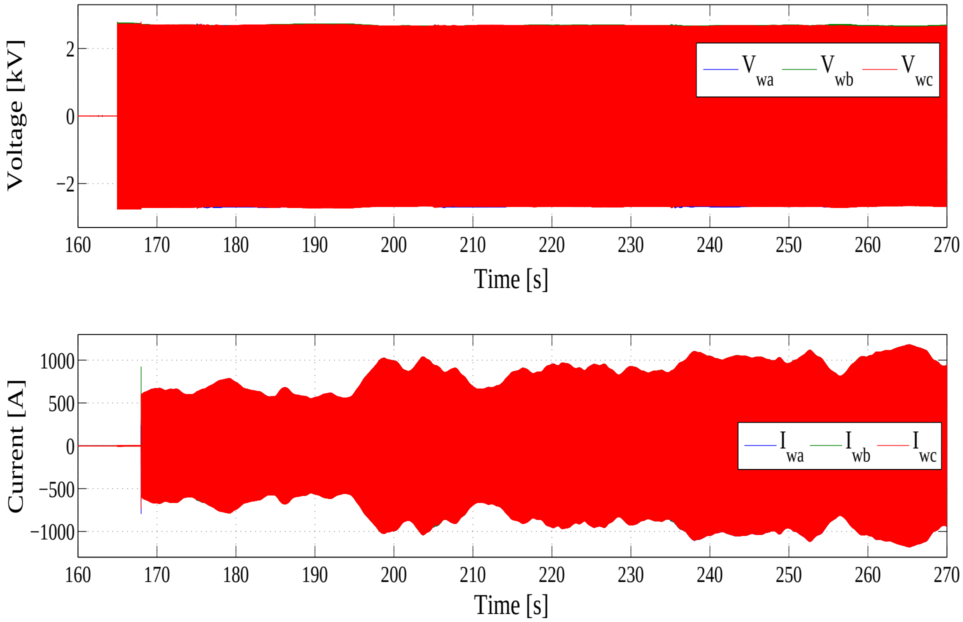

Figure 6.13: Voltage and current of grid side converter (GSC1) in the first wind turbine (WT_1) after closing switch S_3

6.6 Summary

A voltage ramping strategy for inrush current reduction of the HVDC transformer during the energization in the system in which a large offshore wind farm is started-up by means of a power converter of HVDC transmission system has been presented. Furthermore, a procedure has been applied to smooth offshore wind farms start-up. The VRS used in the control system of power converter ramps up the reference voltage in order to ensure the minimum current. Although the considered strategy needs longer duration, it has advantages, since it significantly reduces high inrush current in the system and prevents the malfunction of the protection devices. Dynamic simulations were taken into consideration to highlight the considerable impact of the proposed scheme on the inrush current decrement during the energizing of the HVDC transformer. The simulation results showed that the value of inrush current due to the transformer switching operation is much lower than the rated current value of the transformer and that the smooth start-up of the offshore grid has been performed as designed.

Chapter 7

Recovery inrush current reduction of offshore transformers using proposed voltage ramping strategy

This chapter analyzes the recovery inrush current reduction procedure of transformers in offshore grids and designs a new control system in order to minimize inrush currents under fault recovery condition. The design of this control system is based on the voltage ramping strategy. Moreover, to validate the proposed system, a comparison between the operation of the proposed controller and that of the control system without the reduction strategy has been carried out.

7.1 Introduction

This chapter presents a recovery inrush current reduction technique for all the transformers available in the offshore grid, including HVDC and wind farm transformers. These transformers are exposed to AC faults. The most severe AC fault is a symmetrical three-phase short circuit that leads to the appearance of voltage sags on the power grids, which results in power quality problems. Voltage sags are short duration voltage drops [102] that can cause magnetic flux deviations in the core of transformers. Therefore, transformers will have a DC component of magnetic flux, called flux offset, during the voltage sag period [103, 104, 105].

When the system fault is cleared and the voltage will rapidly restore to its nominal level, the total magnetic flux of the transformer becomes higher than the flux value in the steady-state condition. This fact is due to the same flux offset available in the transformer core. Hence, this over flux in the core may provoke that the transformer in the offshore grid is driven into the saturation mode and consequently, it will lead to high non-sinusoidal excitation current occurrence in the high voltage side of transformers in the offshore grid [103, 104, 106]. The probability of such inrush transients is high during voltage recovery due to the slow decay of magnetic flux deviations [107]. Therefore, transformer inrush currents resulting from voltage recovery after fault occurrence can be introduced as one of the challenges concerning power quality.

These recovery inrush currents can have adverse effects on the functioning of the offshore power systems and its components, such as: mechanical and electrical stress on the transformer, bad operation of protection systems, harmonic overvoltages and instability issues [106].

In addition, the performance of offshore grid converters can be affected by saturation characteristics of transformers under fault and recovery conditions. On the other hand, the converter might be tripped by this type of current and consequently, the operation of HVDC transmission system and offshore wind farm can be disturbed. Hereby, the reduction of these inrush currents has been a serious concern.

Therefore, a Voltage Ramping Strategy (VRS) in which voltage is gradually ramped up from the voltage sag level to the nominal value is introduced in this chapter. This reduction method assures the decrement of transformers inrush currents during the recovery of grids voltage. The verification of the operation of the referred approach is also shown in some simulations.

7.2 Effect of the voltage sag on the grid side converter of offshore wind turbine

The main objective of the control system in the grid side converter of each offshore wind turbine is to inject the generated power into the grid. To achieve this purpose, it is necessary to keep the DC voltage nearly stable, by means of a DC voltage regulator. When a three-phase short circuit fault occurs in the AC grid, it results in the serve voltage sags on the AC terminals of the power converters in each wind turbine. Under these circumstances, the current limitation imposed by the thermal characteristics of the converter is reached and therefore, the incoming power which can be transmitted from one side to the other is restricted in proportion to the AC voltage sag [108]. Thereby, the DC capacitor will be charged by the surplus power and then the DC voltage will increase rapidly which may lead to the activation of the overvoltage protection. On the other hand, the increment of DC voltage can reflect the power imbalance of the DC link [109, 37].

In order to mitigate the DC overvoltage at the DC bus as well as avoid the disconnection of the protection devices of the converters in the grid, a DC chopper where the excess of power is dissipated is employed at the DC side of converters in the wind power system. Namely, the DC voltage exceeding the maximum permitted voltage is reduced to ensure balanced power. The power reduction achieved by means of the DC Chopper can be analytically described as [40]

$$P_{wind}^{red} = P_{wind}(1 + k_r(E_{DC} - E_{min}^{WT})) \tag{7.1}$$

where P_{wind} is the wind turbine power, P_{wind}^{red} is the reduced wind turbine power, E_{DC} is DC voltage and k_r can be selected as

$$k_r = \frac{1}{E_{max}^{WT} - E_{min}^{WT}} \tag{7.2}$$

where E_{max}^{WT} and E_{min}^{WT} indicate the upper and lower thresholds of DC voltage in terminals of the wind turbine converters. The control action $k_r(E_{DC} - E_{min}^{WT})$ is saturated in order not to exceed the power.

Grid side converters in wind turbines are also responsible for grid voltage support using AC voltage controllers during the grid fault. However, when a wind farm is integrated with an AC grid through HVDC transmission systems, it is better to devitalize the AC voltage support in the grid side converters of the wind turbines. The reason for this is to avoid control confluence with the offshore HVDC converter [37].

Finally, as the fault is cleared and the system voltage is restored to the pre-fault level, the incoming power transmission to the AC grid will increase. Hence, the power system is brought back to the normal condition.

7.3 Recovery inrush current reduction process of transformers

When an AC fault takes place in the offshore grid, a voltage sag appears in system. After a defined duration, the fault is cleared and the voltage of the power system increases suddenly to its nominal value. Then, this abrupt change leads to the appearance of high inrush currents in all the transformers available in the offshore grid. The presence of these currents can result in severe drawbacks in the offshore grids. Therefore, the decrement of transformer inrush current is essential for the optimal performance of the system. Thereby, a framework is considered to restore the grid voltage by means of the proposed approach and to reduce inrush transient of transformers, as shown in Figure 7.1. Thus, several functions associated with the determination of the fault occurrence instant and the fault clearance time, the definition of the voltage sag magnitude as well as the evaluation of the fault ride-through have been addressed in this flowchart to achieve the referred objectives. Further details regarding all these steps are presented in the following subsections.

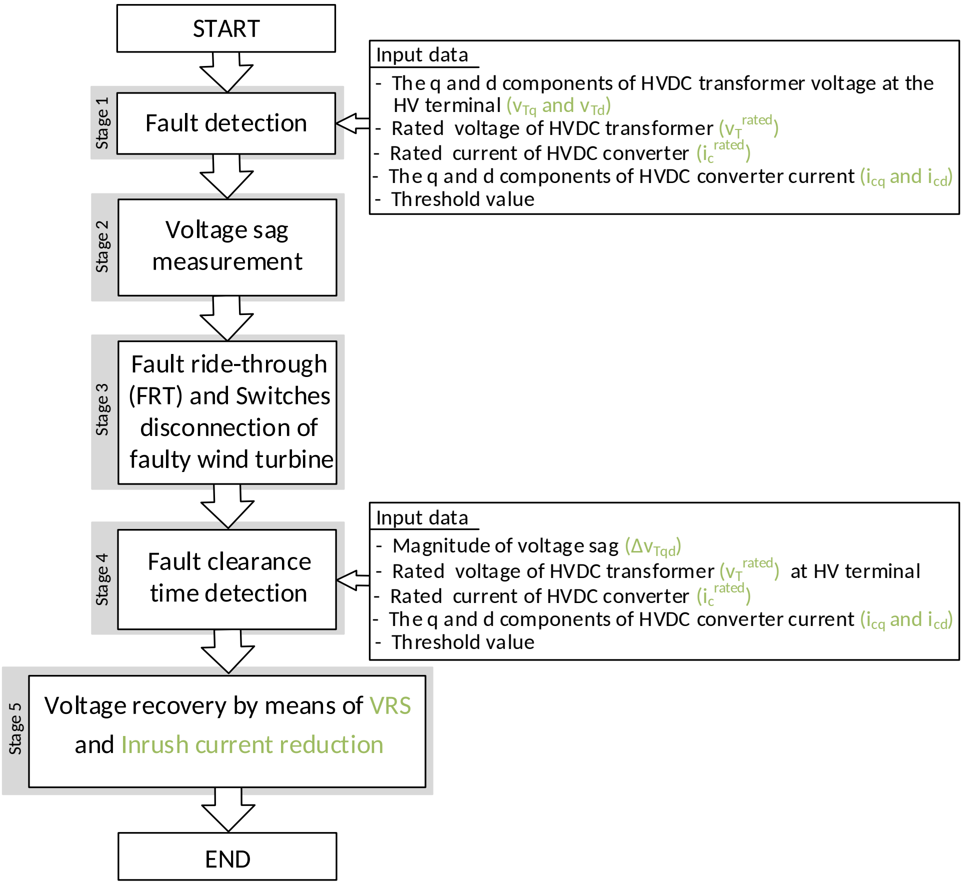

Figure 7.1: Flowchart of the voltage recovery procedure and reduction of transformer inrush current.

7.3.1 Stage 1: Detection of the fault occurrence time (t_i)

The first step in the procedure of voltage restoration and transformer inrush current reduction is to gain the instant in which the fault happens in the offshore wind farm integrated with a HVDC converter. Figure 7.2 illustrates a block diagram of the fault detection scheme. Figure 7.2 shows that the function of fault detection is obtained from the comparison of the voltage amplitude at the high-voltage terminal of the HVDC transformer (v_T) with a threshold (around 90% of its corresponding rated value (v_T^{rated})), as well as from the comparison of the magnitude of the current in the AC terminal of the HVDC converter (i_c) with a threshold (around 90% of rated current (i_c^{rated})). Thus, whenever the value of v_T is less than the threshold and the amplitude of i_c is higher than its threshold, the AC fault is indicated and a signal 1 (or signal of Fault Detection (s_{FD})) is issued. In this thesis, the voltage and current thresholds are considered to be 90%.
Moreover, to compute v_T and i_c, which contain the q and d components of voltage and current, the equations ($\sqrt{v_{Tq}^2 + v_{Td}^2}$) and ($\sqrt{i_{cq}^2 + i_{cd}^2}$) are applied, respectively.

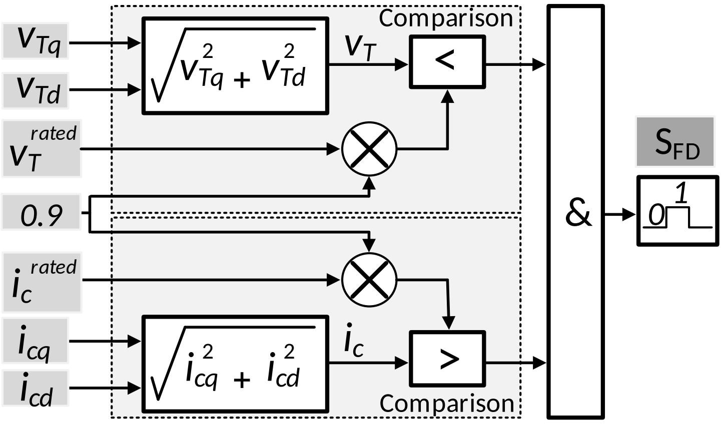

Figure 7.2: Block diagram of fault detection.

7.3.2 Stage 2: Computation of the voltage sag magnitude

When the fault incidence is detected as explained in the previous subsection, the amplitude of the voltage which drops to the lower levels is evaluated. In fact, each component of v_{Tqd} is separately compared with that of the saturation limit and then, the obtained signal is filtered by the zero-order hold and moving average functions, as it can be seen in Figure 7.3. These functions are used to obtain the voltage drop during the fault interval.

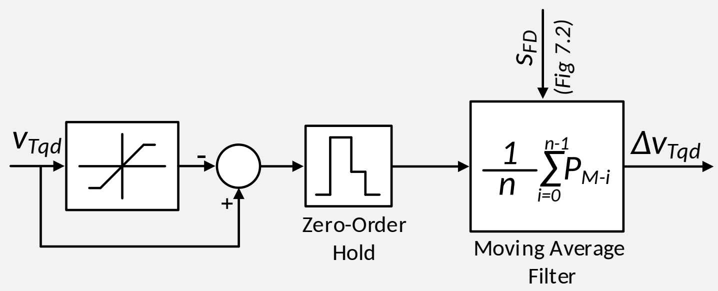

Figure 7.3: Block diagram of measurement system of voltage sag.

7.3.3 Stage 3: Fault ride-through and operation of protection devices

If the measured voltage level meets the Fault Ride Through (FRT) requirements of the wind turbine [110], the wind turbine stays connected to the offshore system for a specific period of time under grid fault. Otherwise, the faulty wind turbine can be disconnected from the power system because of the tripping of the protection devices and hereupon, the isolation of the fault from the grid will take place. The instant in which the fault is cleared by means of the switch disconnection is also called t_f.
Furthermore, in the case of AC fault at a wind turbine, the other wind turbines will experience a sudden voltage drop. However, these wind turbines and their generators also remain connected to the power system. It is worth emphasizing that the generators of the wind turbines are under the load in these circumstances.

7.3.4 Stage 4: Detection of the fault clearance time (t_f)

Figure 7.4 depicts the block diagram of the fault clearance time detection. This block compares the amplitude of the AC current of the HVDC converter (i_c), calculated according to equation $\sqrt{i_{cq}^2 + i_{cd}^2}$, with its threshold (90% of i_c^{rated}) and also, a comparison between the absolute value of voltage sag magnitude ($|\Delta v_{Tqd}|$) with the threshold of the HVDC transformer voltage at the high voltage terminal (10% of v_T^{rated}), as well as with the nominal value of the HVDC transformer voltage (v_T^{rated}) will accomplish. Once the i_c is smaller than the threshold and the absolute value of Δv_{Tqd} is higher than the threshold of v_T^{rated} and smaller than v_T^{rated}, namely $0.1v_T^{rated} < |\Delta v_{Tqd}| \leq v_T^{rated}$, the instant of fault removal is determined and a signal 1 (or signal of the Fault Clearance Time Detection (s_{FCTD})) is generated.

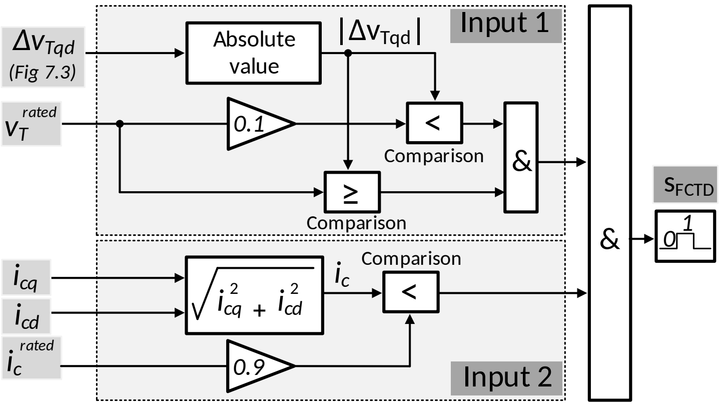

Figure 7.4: Block diagram of fault clearance time detection.

7.3.5 Stage 5: Voltage recovery and inrush current diminution

When the protection devices operate and the three-phase switches of the faulty section are opened for isolation (at instant t_f), the voltage recovery will take place and the AC grid voltage will return to its nominal level.

In the new grid formed after the isolation of the faulty wind turbine, the voltage restoration of all the wind turbines will be accomplished at the same time. This implies that all the transformers which increase the low-level voltages generated at the wind turbine to the medium voltage used in the collection grid of the wind farm are simultaneously recovered with the HVDC transformer, which enhances the collection grid voltage to the transmission-level voltage.

In addition, the voltage recovery of transformers generates huge inrush currents at the instant of their restoration to the grid, due to the transformer core saturation. Thus, in order to reduce these transformer inrush transients during fault recovery, a soft recovery method of voltage is required. Thereby, this chapter proposes a voltage control system based on the Voltage Ramping Strategy to ensure the inrush current decrement as well as to guarantee the simultaneous restoration of all the transformers available in the offshore grid after fault removal. The advanced control system is handled in the offshore HVDC converter system and further details will be presented in Section 7.4.

7.4 Proposed control system based on VRS

The purpose of the proposed control system is to regulate voltage amplitude and frequency under normal operation, as well as to restore the voltage to the nominal level under grid recovery condition so as to ensure the reduction of inrush transients and the stability of the system. The design of the proposed controller for the HVDC converter is illustrated in Figure 7.5.

As shown in Figure 7.5, the control structure for the HVDC converter is based on the vector control method including a lower level control (inner loop) and an upper level control (AC voltage loop). The inner loop is responsible for the regulation of the qd components of the current via the coupling filter and the voltage loop is in charge of the control of the AC voltage amplitude at the high voltage side of the transformer. The control is almost similar to the one utilized in the power injection system for the offshore load [51] but it allows for the control of i_{cd}^* by $(v_{Td}^* + \hat{v}_{Td} - v_{Td})$ and i_{cq}^* by $(v_{Tq}^* + \hat{v}_{Tq} - v_{Tq})$, as shown in Figure 7.5. Therefore, the performance of this developed voltage loop not only depends on the amplitudes of the transformer voltage, v_{Tqd}, and HVDC transformers current, i_{Tqd}, but also depends on the amount of voltage sag and the ramp rate imposed to obtain the minimum inrush current. As a matter of fact, the qd components value of the voltage drop including the ramp at the fault clearance instant is $\hat{v}_{Tqd}$. With regard to Figure 7.5, the qd components of the HVDC converter current reference, i_{cq}^* and i_{cd}^*, are determined as

$$i_{cq}^* = i_{Tq} - \omega c_f v_{Td} + k_{olq}(s)(v_{Tq}^* + \hat{v}_{Tq} - v_{Tq}) \tag{7.3}$$

$$i_{cd}^* = i_{Td} + \omega c_f v_{Tq} + k_{old}(s)(v_{Td}^* + \hat{v}_{Td} - v_{Td}) \tag{7.4}$$

where $\hat{v}_{Tq}$ and $\hat{v}_{Td}$ are the two new control inputs.

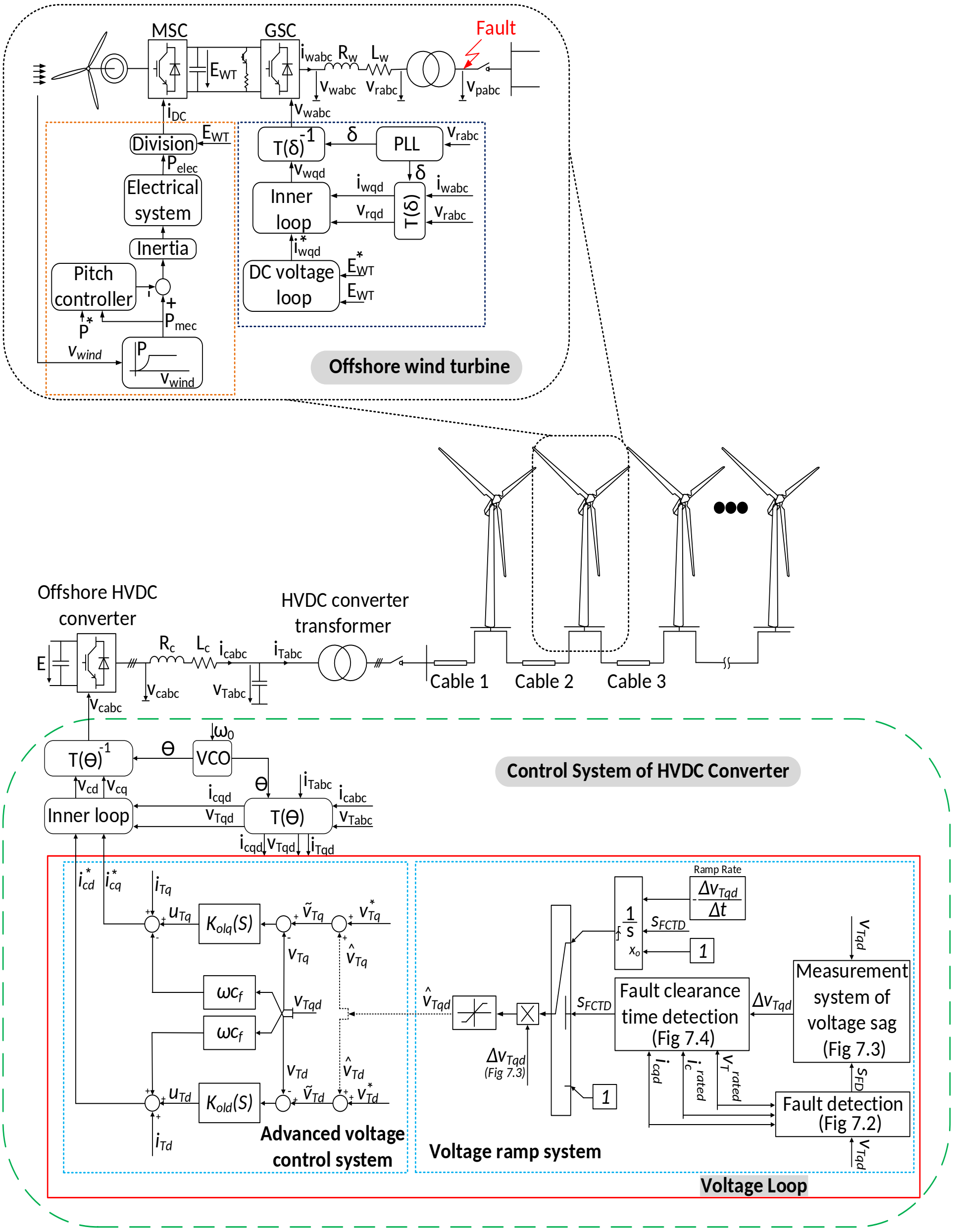

Figure 7.5: The proposed control block diagram of offshore HVDC converter for recovery inrush current reduction.

As the fault takes place, these components, $\hat{v}_{Tq}$ and $\hat{v}_{Td}$, can change the set-points of voltage, v^*_{Tq} and v^*_{Td}, and also construct a voltage ramp at the instant in which the fault is cleared, t_f.

To perform set-points variations, the magnitude of the voltage sag, namely Δv_{Tqd}, is immediately calculated after fault detection, as described in Subsection 7.3.2. Thus, the obtained content, Δv_{Tqd}, is gradually ramped up to zero at the moment in which the fault clearance is indicated by the signal of the Fault Clearance Time Detection, s_{FCTD}, as shown in Figure 7.5. The voltage ramp rate is commonly tuned according to the division of the voltage sag value, Δv_{Tqd}, into the voltage recovery duration, $\Delta t = t_r - t_f$, so as to achieve the lowest inrush currents. It should be noted that the t_r is the time at which the initial condition is reached.

The conclusion of this analysis is the new inputs of the voltage control system, $\hat{v}_{Tqd}$. Moreover, Figure 7.5 shows that u_{Tq} and u_{Td} are the output of two independent compensators. Namely,

$$u_{Tq} = k_{olq}(s)(\widetilde{v}_{Tq} - v_{Tq}) \tag{7.5}$$

$$u_{Td} = k_{old}(s)(\widetilde{v}_{Td} - v_{Td}) \tag{7.6}$$

where $\widetilde{v}_{Tq} = v^*_{Tq} + \hat{v}_{Tq}$ and $\widetilde{v}_{Td} = v^*_{Td} + \hat{v}_{Td}$. The compensators $k_{olq}(s)$ and $k_{old}(s)$, are obtained on the basis of the LQG optimization procedure discussed in Chapter 3. When the control signals u_{Tq} and u_{Td} are provided, the components i^*_{cq} and i^*_{cd} are built according to Equations (7.3) and (7.4) and rendered to the corresponding inner loop controllers.

The most significant advantages of the aforementioned method are recovery inrush current reduction, system stability and the avoidance of the trip of the HVDC converter and protection relays of the transformer.

7.5 Simulation results

In this section, simulation studies have been carried out to evaluate the performance of the advanced control system under symmetrical three-phase fault condition and voltage recovery process with MATLAB/Simulink. The studied system consists of a HVDC converter connected to a cluster of wind turbines, as illustrated in Figure 7.6. In this section, simulation results for the first three wind turbines of the cluster are analyzed. Three different scenarios have been considered. The first one analyzes the inrush currents of

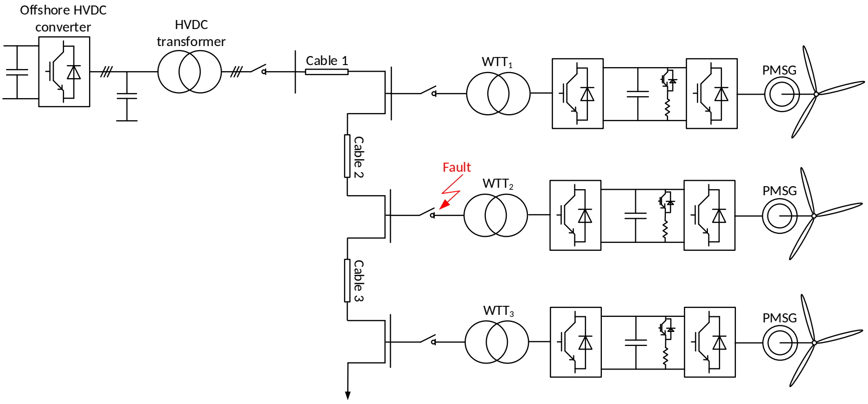

Figure 7.6: Schematic diagram of the simulated offshore grid during the voltage recovery.

all the transformers available in the power system without implementing the developed method. The second one simulates the behavior of all the transformers using the proposed technique which has considerable impact on the reduction of inrush currents magnitude. The third one analyzes the effect of different durations of voltage ramp on the transformer inrush transients.

In the referred cases, an approximately 85% voltage sag with a duration of 300 ms is applied at the middle point between connection of the second wind turbine transformer and offshore gird at instant $t = 150$ s. Figure 7.6 illustrates the schematic diagram of the simulated network. The parameters have been summarized in Table 7.1. It should be noted that in system operation under the recovery process, WT_1 and WT_3 remain also connected to the offshore grid, whereas the second turbine WT_2 is disconnected at the instant of fault clearance, $t = 150.3$ s.

Table 7.1: Parameters of the simulated scenarios

parameter	value	unit
PMSG nominal power (P_n)	5	[MW]
PMSG nominal voltage (V_n)	3.3	[kV]
WT inertia time constant (J_{WT})	1.7	[s]
WT electrical time constant (τ_{ele})	0.01	[s]
WT pitch time constant (τ_{pitch})	0.17	[s]
WT nominal DC voltage (E_{WT})	± 3	[kV]
WT lower DC voltage level (E_{WT}^{min})	6.18	[kV]
WT upper DC voltage level (E_{WT}^{max})	6.48	[kV]
WT DC capacitor (C_{WT})	1.4	[mF]
WT transformers (Δ/Y_g) nominal power (P_n)	5.56	[MVA]
WT transformers nominal voltage (V_p/V_s)	33/3.3	[kV]
WT transformers resistance/inductance (R/L)	0.006/0.06	[pu]
WT transformers magnetization resistance (R_m)	500	[pu]
WT transformers saturation flux (Φ_{sat})	1.1	[pu]
WT transformers residual flux (Φ_{rj})	(+0.8,-0.8,0)	[pu]
Submarine cable resistance (R_{CS})	0.06	[Ω/km]
Submarine cable inductance (L_{CS})	0.36	[mH/km]
Submarine cable capacitor (C_{CS})	0.26	[μF/km]
Submarine cable 1 length	1	[km]
Submarine cable 2 length	0.7	[km]
Submarine cable 3 length	0.7	[km]
HVDC transformers (Y_g/Δ) nominal power (P_n)	350	[MVA]
HVDC transformers nominal voltage (V_{HV}/V_{LV})	195/33	[kV]
HVDC transformers resistance/inductance (R/L)	0.003/0.14	[pu]
HVDC transformers magnetization resistance (R_m)	500	[pu]
HVDC transformers saturation flux (Φ_{sat})	1.25	[pu]
HVDC transformers residual flux (Φ_{rj})	(+0.94,-0.94,+0.84)	[pu]
HVDC converters nominal power (P_n)	350	[MVA]
HVDC converters nominal voltage (V_n)	195	[kV]
(X/R)	10	[pu]

7.5.1 Recovery of transformers without using VRS

In this case, there is no reduction technique for recovery inrush currents, i.e., the transformer inrush current is considerable and can affect the operation of protection devices. The voltage and current of the HVDC transformer before, during and after the fault are shown in Figure 7.7. From Figure 7.7, it can be deduced that fault causes a voltage sag of around 64% in the voltage of the transformer primary side at $t = 150$ s. It is worth noting that an overcurrent is generated due to the fault occurrence and thereafter it is limited by the HVDC converter.

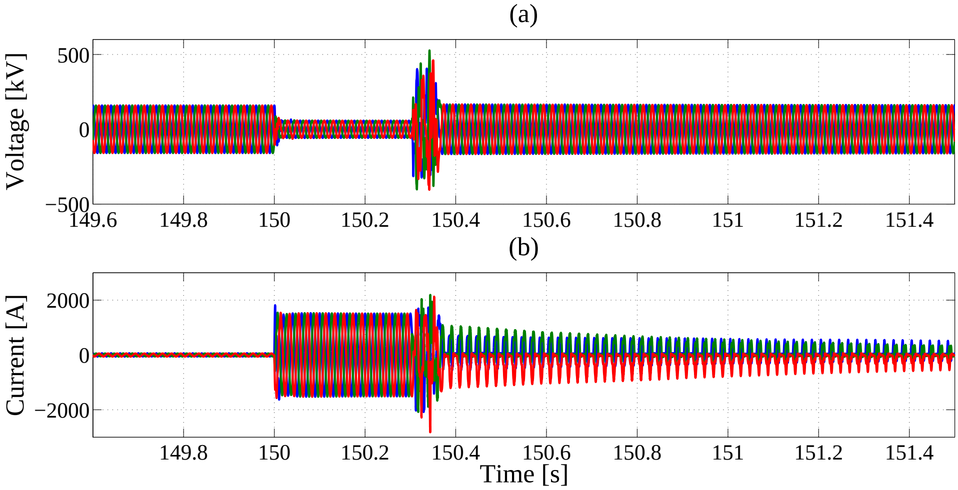

Figure 7.7: Influence of the fault and voltage recovery on HVDC transformers behavior. (a) Primary side voltage. (b) Inrush current.

As shown in Figure 7.7 (a), the voltage is recovered to the nominal value, i.e., there is no time delay for the voltage restoration to this level after three-phase fault removal. In other words, according to Figure 7.7 (b), a large transient current is drawn by the transformer at the instant of fault removal, which is a consequence of the transformer core saturation caused by the sudden voltage increment.

The inrush currents of the different phases of the HVDC transformer in the system without VRS are shown in Figures 7.8 (a), (c) and (e) and zoomed at the voltage recovery instant in Figures 7.8 (b), (d) and (f). As it can be concluded from these figures, the inrush current magnitude in phase-c for the HVDC transformer is higher than those in the two other phases. In other words, the maximum inrush current of phases a, b and c are +715 A, +1090 A, -1325 A, respectively.

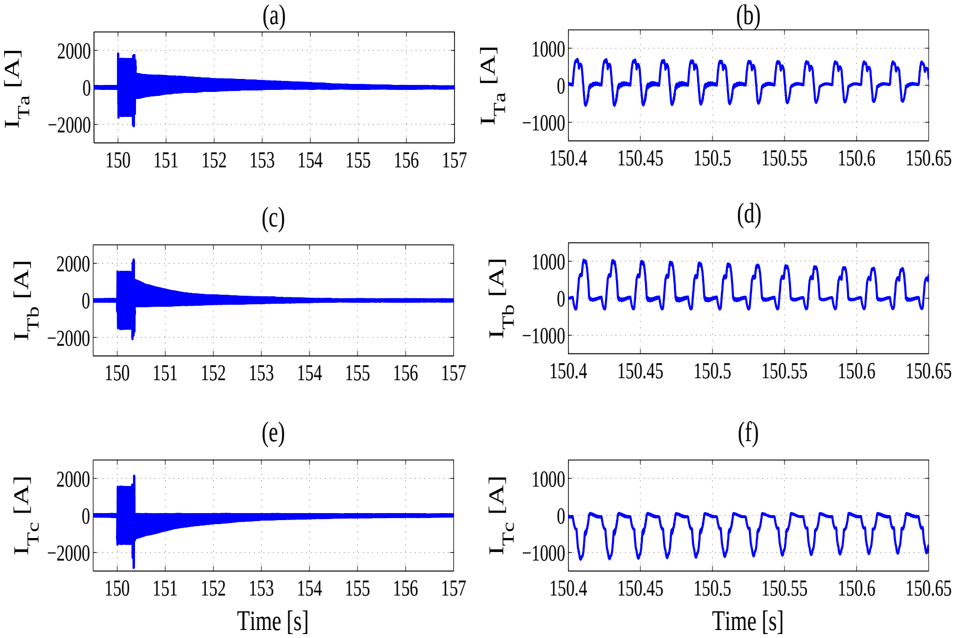

Figure 7.8: Inrush current of different phases of HVDC transformer during fault and voltage recovery cases in system without VRS.

Figures 7.9, 7.10 and 7.11 (a) indicate that the primary voltage of each wind turbine transformer drops when the three-phase fault occurs at the second wind turbine. Thereby, the amount of each voltage sag is nearly 85%. After that, fault removal is performed by means of the disconnection of the faulty wind turbine from the offshore grid at t = 150.3 s. In this case, the other wind turbines keep also connected to the offshore system.

In Figure 7.10 (a), it can be clearly observed that the transformer primary voltage of the second wind turbine will be zero after fault removal whereas the voltages of the two other wind turbine transformers are quickly restored to the nominal value, $v_{pn} = 33$ kV, as seen in Figures 7.9 and 7.11 (a).

Consequently, from Figures 7.9, 7.10 and 7.11 (b), it can be deduced that transformers of WT_1 and WT_3 experience high inrush currents due to the transformer core saturation. Transformer inrush currents of the first and third wind turbines in phases a, b and c have the values -340 A, +466 A and +282 A, respectively. It should be also noted that the current under the

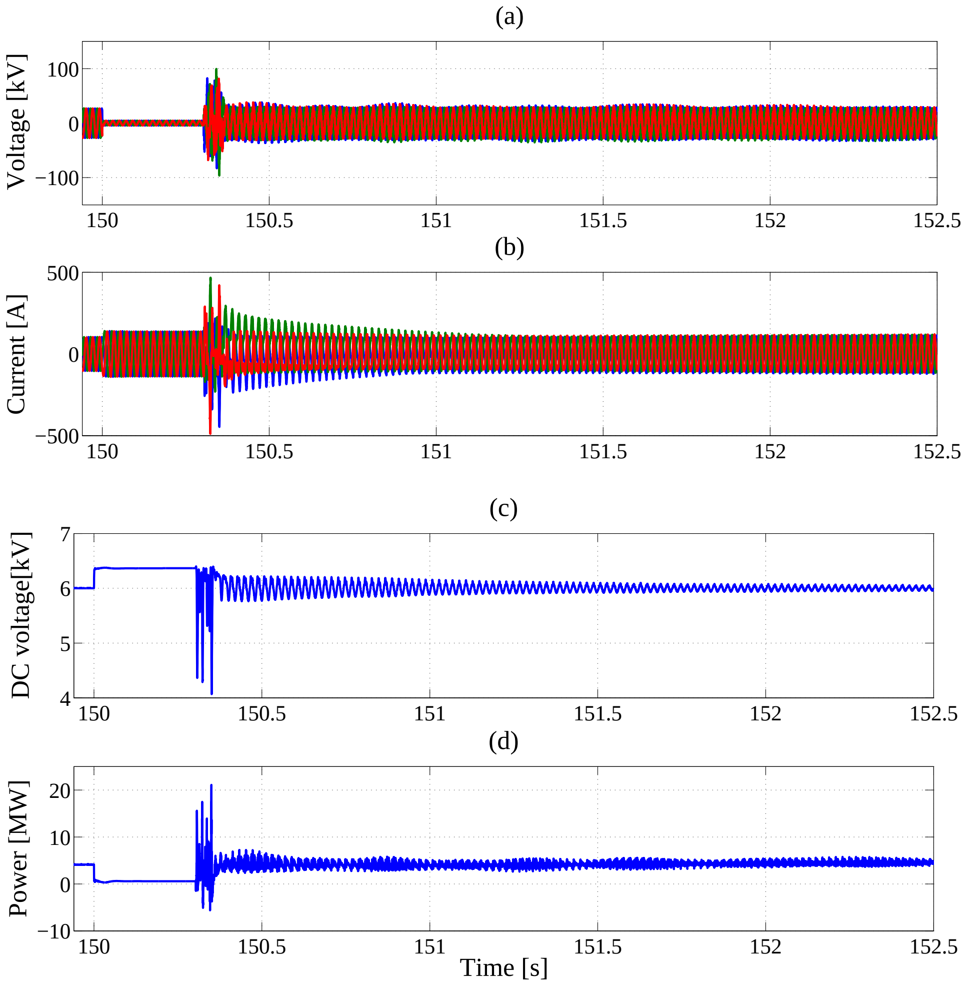

Figure 7.9: Simulation results for wind turbine 1 under fault and recovery conditions. (a): Transformers primary voltage of the wind turbine. (b): Transformers primary current waveform of the wind turbine. (c): DC voltage of the wind turbnine. (d): Active power injection of the wind turine.

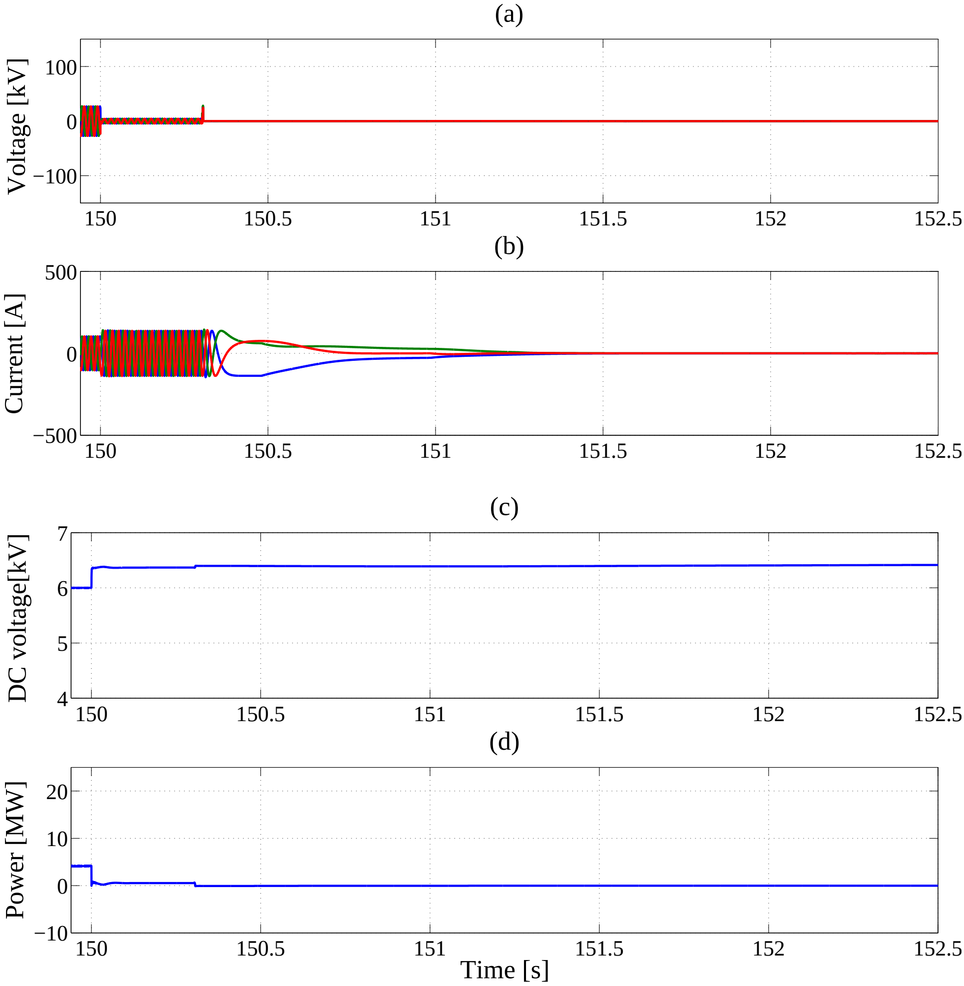

Figure 7.10: Simulation results for wind turbine 2 under fault and recovery conditions. (a): Transformers primary voltage of the wind turbine. (b): Transformers primary current waveform of the wind turbine. (c): DC voltage of the wind turbnine. (d): Active power injection of the wind turine.

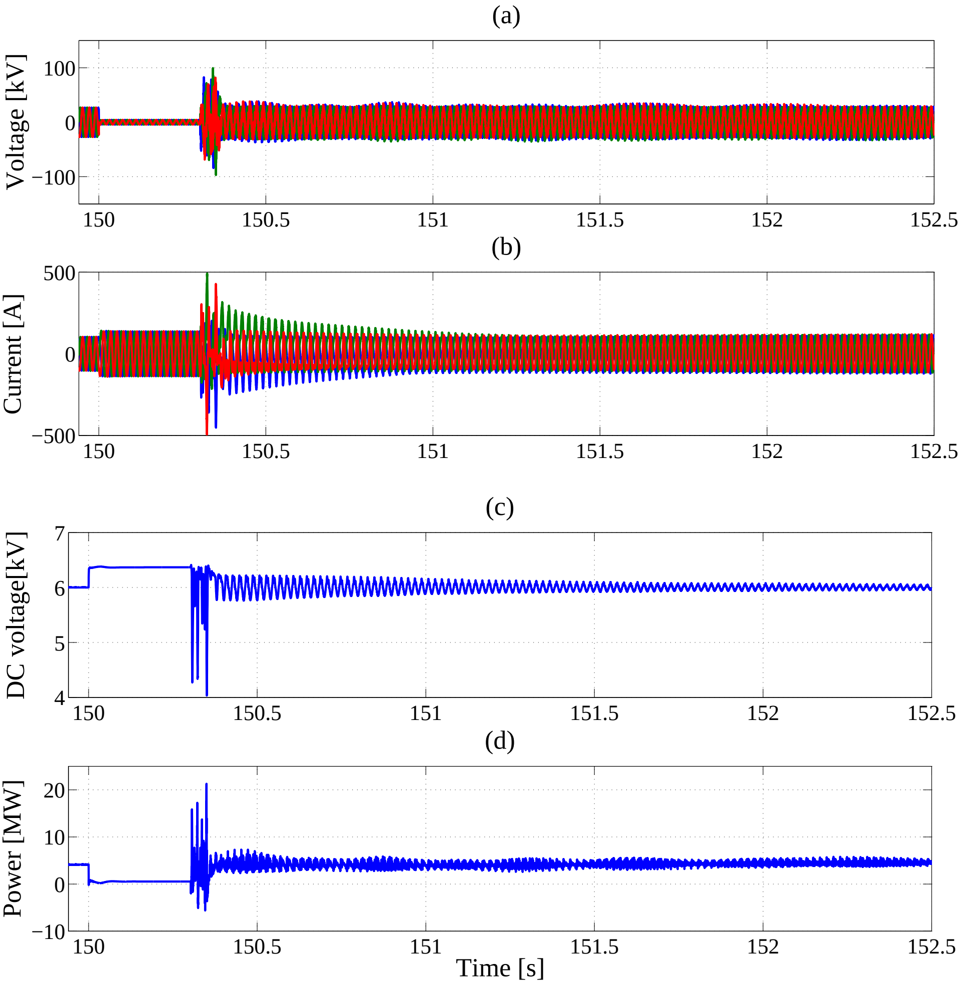

Figure 7.11: Simulation results for wind turbine 3 under fault and recovery conditions. (a): Transformers primary voltage of the wind turbine. (b): Transformers primary current waveform of the wind turbine. (c): DC voltage of the wind turbnine. (d): Active power injection of the wind turine.

fault condition is equal to the rated current of each wind turbines converter. As shown in Figures 7.9, 7.10 and 7.11 (c) and (d), during the fault, the active power cannot be completely injected into the offshore grid by each wind turbine, in which results in the increment of the DC link voltage. On the other hand, the DC voltage exceeds the specified threshold during the fault and therefore, the DC chopper is activated to reduce this voltage and also ensure an adequate power reduction. After fault removal, the DC voltage returns to the nominal level and active power is restored quickly. As illustrated, the DC voltage and active power experience oscillations during voltage recovery.

7.5.2 Recovery of transformers using VRS

In order to alleviate inrush currents, a VRS for recovery after fault has been implemented in the voltage control system of the HVDC converter. A similar three-phase AC fault of 300 s duration is applied to the second wind turbine as in the previous case. In this method, as soon as the fault is removed, the voltage of the offshore grid gradually ramps up to the nominal value to be able to reduce high currents. Therefore, this voltage ramping technique does not allow for the voltage to return to normal condition suddenly and decreases the saturation probability of transformers core. The method has been simulated and the results are presented below.

Figure 7.12 shows the three-phase voltage and current of HVDC transformer for a system with VRS. From this Figure, it can be deduced that a 15 s delay has been taken into account for the voltage to be recovered to the rated value after fault clearance. Therefore, currents variations in the HVDC transformer, as observed in Figure 7.12 (b), are associated with this ramp for voltage recovery.

In this case study, the recovery of voltage is slower than in the case without VRS, as illustrated in Figure 7.12 (a), regardless of the magnitude of voltage sag. On the other hand, in accordance with Figure 7.12 (a), it takes longer time for voltages of different phases to attain nominal values whereas in Figure 7.7 (a), the voltages are restored very quickly. Also, comparison of Figure 7.12 (b) and Figure 7.7 (b) indicates that inrush currents of the HVDC transformer in a system with VRS are much lower than those in a system without VRS. Thus, it can be mentioned that the VRS with $t_{ramp} = 15$ s can reduce the inrush current to nearly 1/3 of the value of inrush currents in the system without VRS during voltage recovery.

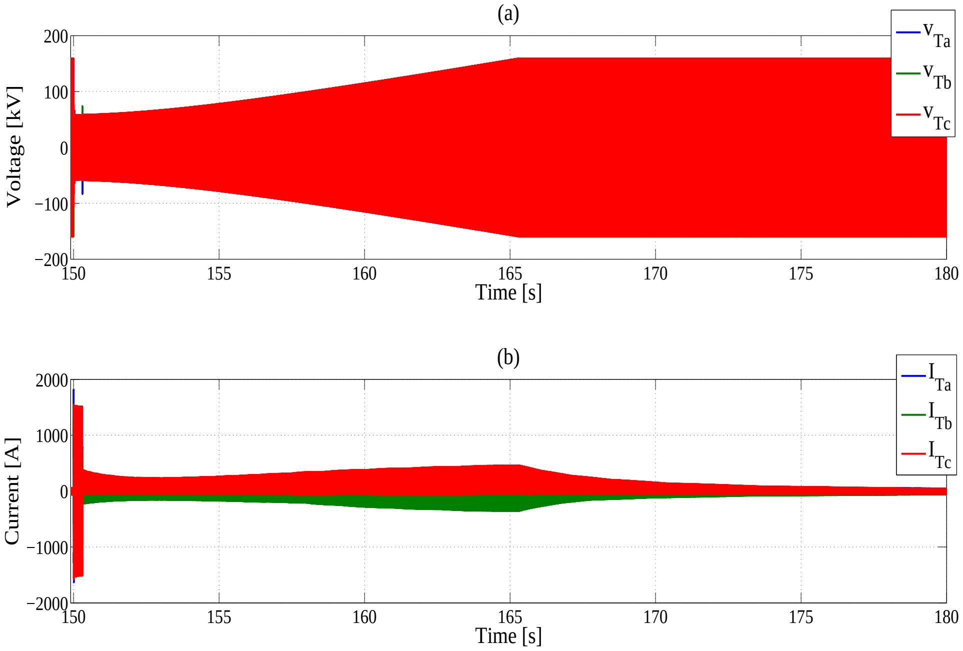

Figure 7.12: Voltage and current at high voltage terminal of HVDC transformer (t_{ramp} =15 s)

The inrush current waveforms of the HVDC transformer for different phases, a, b and c are shown in Figures 7.13 (a), (c) and (e) and zoomed in Figures 7.13 (b), (d) and (f). With regard to t_{ramp} = 15 s, the inrush currents for phase a, b and c are +228 A, -356.5 A and +460.5 A, respectively. Consequently, it is clear that the voltage recovery with VRS will generate smaller currents.

Figure 7.14 (a)-(f) depicts the voltage and current of the transformer for each wind turbine. As shown in Figure 7.14 (a)-(c), during voltage recovery, AC voltages corresponding to the transformer primary side of WT_1 and WT_2 increase slowly to the nominal level, 33 kV. However, the transformer voltage of the second wind turbine, WT_2, is kept zero due to the disconnection of the faulty section from offshore grid at the instant of fault removal. For the sake of the simultaneous recovery of all the transformers, including the transformers of wind turbines and the HVDC transformer, the transformer inrush current magnitude of the wind turbines is reduced using VRS available in the AC voltage control system of the HVDC converter, as illustrated in Figure 7.14 (d)-(f).

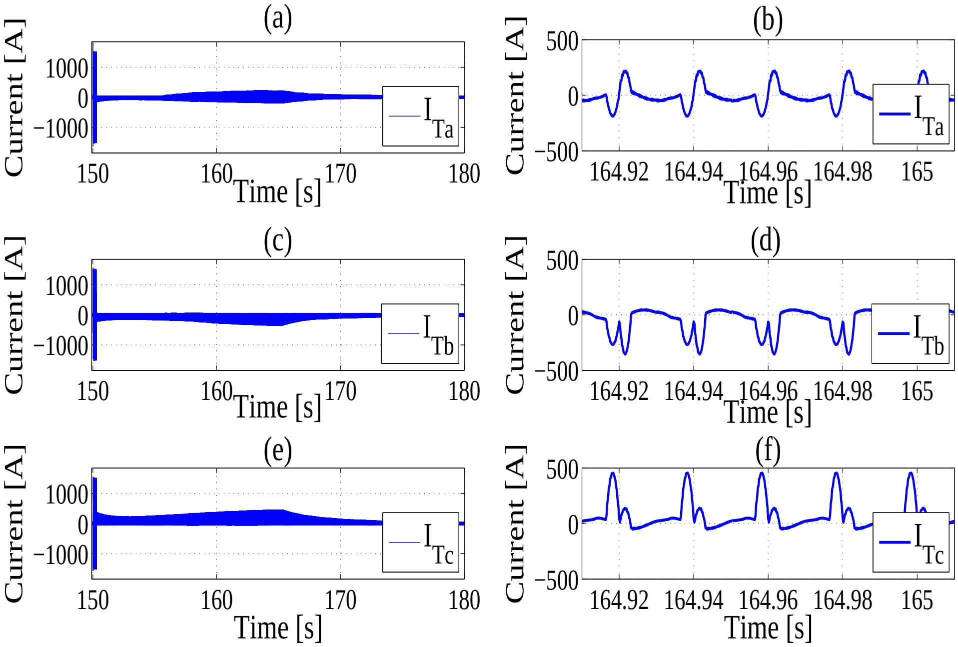

Figure 7.13: Inrush current of different phases for HVDC transformer $t_{ramp} = 15$ s

By comparing the case with VRS and the previous one without VRS (i.e., Figures 7.14 (d) and (f) with Figures 7.9 and 7.11 (b)), it can be observed that the transformer inrush current of each of the wind turbines in the different phases, a, b and c was reduced by 53.2%, 64% and 48.3%, respectively.
The dynamic performance of the active power and DC voltage in the first wind turbine (WT_1) under fault and voltage recovery conditions is sketched in Figure 7.15 (b) and (d). In order to better realize these shapes, the plots of AC voltage and current of the grid side converter are also shown in Figures 7.15 (a) and (c).
When the fault is simulated at the second offshore wind turbine, the DC chopper of the wind turbine is activated to control the DC voltage and to reduce the active power injection, as observed in Figure 7.15 (b) and (d). The operation of the DC chopper protection is included based on the overvoltage of the DC link capacitor of the wind turbine.

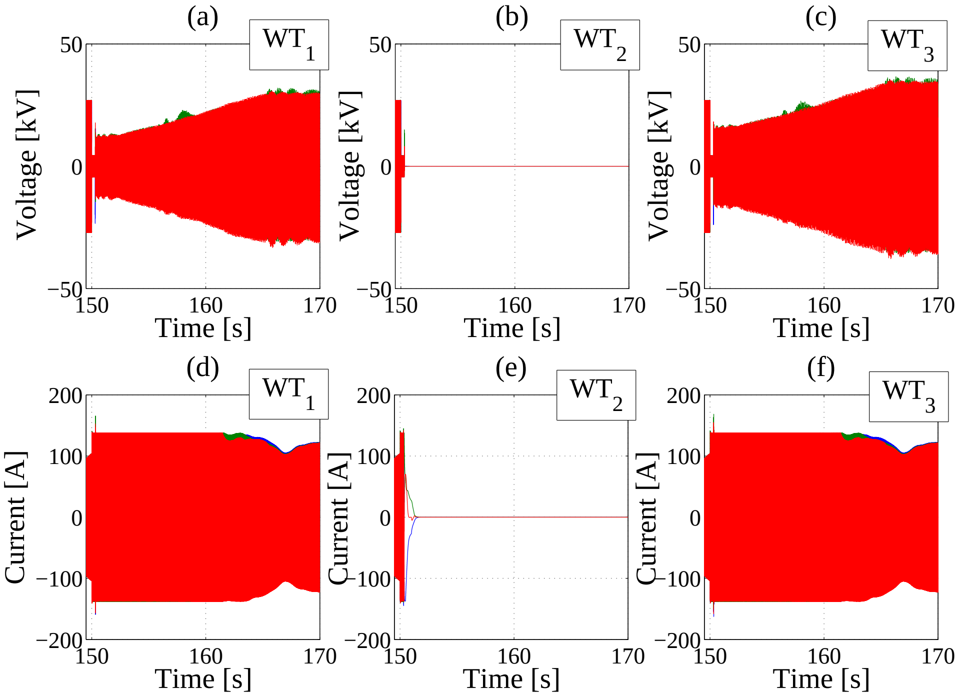

Figure 7.14: Primary voltage and inrush current of transformer in each wind turbine under fault and recovery conditions

Once the system is restored and the DC overvoltage of the full power converter wind turbine comes back to the nominal level, all the power injection is also recovered. It is worth emphasizing that these restorations to the normal conditions are accomplished through a ramp, as can be seen in Figures 7.15 (b) and (d).

Finally, Figure 7.16 shows the reduction of the peak recovery inrush current of the HVDC transformer (in phase-a) for different time periods of ramp.

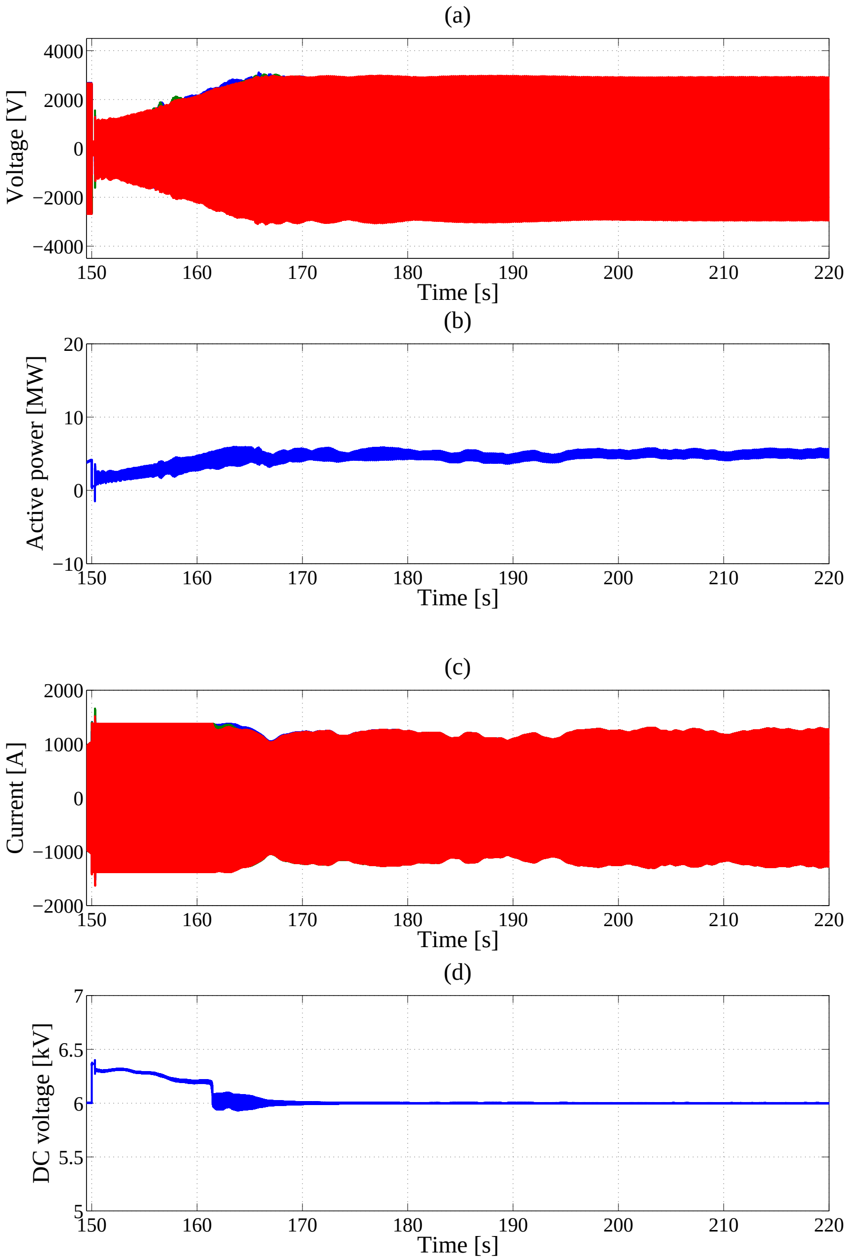

Figure 7.15: AC and DC voltages, active power and current of the first wind turbines converter during fault and recovery conditions

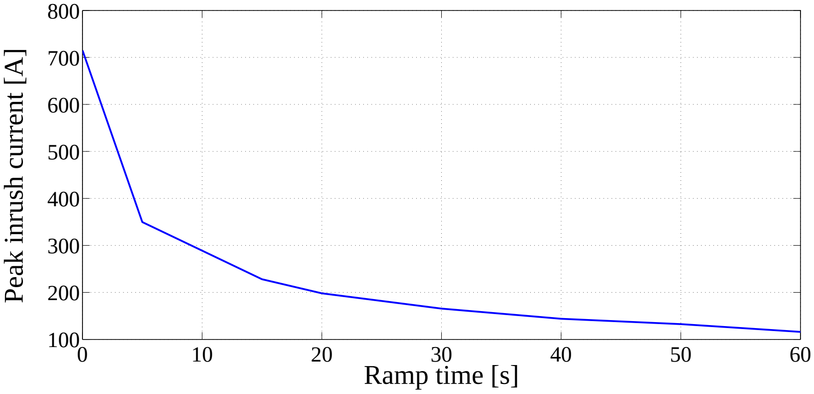

Figure 7.16: Variation of the peak inrush current of the HVDC transformer versus different time periods of ramp (for phase-a)

7.6 Summary

This chapter has introduced an inrush current reduction technique for offshore transformers during system recovery. This voltage ramping strategy can be designed to guarantee the inrush current decline of transformers available in the offshore grid, including HVDC and wind turbines transformers, under system restoration mode and to ensure a robust stability. The proposed method can be implemented in the AC voltage control system of the HVDC converter which is based on a conventional vector control system and can gradually increase the grid voltage to the nominal level. The method has been tested under three scenarios, the simulation results of which show the validity of this approach for recovery inrush current reduction.

Chapter 8

Conclusions

Several studies to improve the operation of offshore grids under inrush transient condition of the transformer have been presented in this thesis. This chapter explains the main conclusions drawn throughout the thesis and it also contains lines of research for future work.

8.1 Contributions

The contributions are detailed per chapter.

- **Chapter 2** analyzed the structure of an offshore grid and the existence of different configurations in offshore wind farms as well as different types of wind turbines, power converters and HVDC transmission systems. This structure makes voltage control of the offshore wind farm grid possible through the HVDC converter and also the accurate analysis of the models and controllers used for each of the offshore components in the next chapters.

- **Chapter 3** addressed the dynamic model and different control schemes for the voltage source converter of the HVDC transmission system. The design of the control systems has been produced considering the dynamics of the AC and DC grids of the converter, the current and the voltage control loops, PLL and VCO. Once the HVDC converter is connected to the offshore wind farm, by applying the voltage and current control mechanisms, HVDC system stability and power balance under different operating conditions can be achieved.

- **Chapter 4** presented the simplified model and the control design for the variable-speed wind turbine. The generator of the wind turbine is totally decoupled from the offshore wind turbine grid through full power converters. The scheme of the control system is based on the basic vector control method. The model applied has been tested through simulations and the results have proved the ability of the model to reflect variations in the power extracted by the turbine dependent on the alterations in the incoming wind. The wind turbine model can be used in offshore transformer inrush current reduction studies and it can provide a highly accurate estimate of the wind turbine dynamic response.

- **Chapter 5** analyzed extensively the inrush transient phenomenon during transformers energization in offshore HVDC grids. Under inrush current condition, the HVDC converter might be tripped and the performance of HVDC transmission grid might be disturbed. Thus, the inrush current reduction of the transformer in offshore HVDC systems is an important issue. Several techniques to decrease the inrush transient of the transformer in a power system have been presented. The analyzed strategies cannot ensure the correct performance of HVDC grids in case of inrush transient due to their complexity, high losses and costs, the requirement for residual flux information and bigger physical spaces. Therefore, a new method has been proposed in this thesis which allows to minimize high inrush currents and to operate correctly the HVDC converter under such condition. The transformer model has been designed to estimate the dynamic behavior of transformers whenever the transformer core is driven into saturation mode. The representation of the transformer has been tested through simulations.

- **Chapter 6** proposed a voltage ramping strategy to reduce the energization inrush current of the HVDC transformer during the process of offshore wind farms start-up and integration into the onshore AC grid. This method is based on the ramping of the voltage in the high voltage terminal of the transformer connected to the HVDC converter. The ramped voltage ensures minimum energization inrush current in the offshore grid. The proposed strategy can provide much lower inrush currents when the voltage ramp slope is slower. The other advantages of the considered technique are no tripping of the HVDC converter under the transformer energization mode, simplicity, cost-effective and easy implementation in the HVDC converters control system. The performance of this methodology has been validated by means of dynamic simulations.

- Finally, **Chapter 7** proposed a voltage control system based on VRS for the HVDC converter to restore all the transformers in the offshore grid after fault recovery with minimum inrush currents. The considered control system has been developed on the basis of the conventional vector control system and has made the grid voltage to increase according to a ramp. For this reason, a system voltage recovery procedure has been presented in order to achieve the voltage sag derived from the fault occurrence and to then implement a desired voltage ramp for the restoration of the grid voltage. The selection of lower voltage ramp slopes can lead to the appearance of smaller inrush currents in the offshore grid. The control system proposed can ensure the safe operation of the converters available in the HVDC system and in wind turbines and consequently, the stability of the offshore grid. The validation of the concept has been confirmed by means of simulations and the performance of the control system with and without the new strategy has been compared, this comparison showed that the proposed method can diminish inrush current.

8.2 Future Work

Inrush current under transformers energizing and recovery conditions is an important challenge in power grids. This transient in HVDC systems is a new topic and therefore, there is much research to do in the field of inrush current reduction in these grids. The work developed in this thesis has propounded several research lines for future work. Given this, the future research lines can be the following:

- Analysis of inrush current in MMC-HVDC systems.
- Study of the start-up and integration of the offshore wind farm into the onshore AC system through MMC converters.
- Practical implementation of the transformers energization inrush current reduction methodology explained in Chapter 6.
- Design a VRS-based controller in MMC converters of the offshore grid to reduce HVDC transformer inrush currents during the start-up procedure of offshore wind farms.

- Practical implementation of the VRS-based voltage control system of the HVDC converter under transformers voltage recovery condition explained in Chapter 7.
- Analysis of the control system based on the voltage ramping strategy to decrease transformers recovery inrush current in offshore grids including MMC converters.
- Comparison of the VRS strategy behavior in offshore grids with MMC converters and VSC converters.

Bibliography

[1] S. Abdulsalam and W. Xu, "A sequential phase energization method for transformer inrush current reduction part I: Transient performance and practical considerations," *IEEE Transactions on Power Delivery*, vol. 22, no. 1, pp. 208–216, Jan 2007. xvi, 71, 76, 172

[2] D. Taylor, J. Law, B. Johnson, and N. Fischer, "Single-phase transformer inrush current reduction using prefluxing," *IEEE Transactions on Power Delivery*, vol. 27, no. 1, pp. 245–252, Jan 2012. xvi, 77

[3] J. Faiz and S. Saffari, "Inrush current modeling in a single-phase transformer," *IEEE Transactions on Magnetics*, vol. 46, no. 2, pp. 578–581, Feb 2010. xvi, 80, 82, 84

[4] D. Van Hertem, O. Gomis-Bellmunt, and J. Liang, *HVDC Grids: For offshore and supergrid of the future.* John Wiley & Sons, 2016, vol. 51. 1, 2, 9, 10, 12, 13, 14, 15, 16, 17, 20, 21, 22, 23, 24, 25, 26, 58, 59

[5] J.G.Slootweg, "Wind power: Modelling and impact on power system dynamics," in *PhD thesis, Delft University of Technology*, 2003. 1

[6] European Commission, *Communication from the commission to the European Council and the European Parliament-An energy policy for Europe.* Commission of the European Communities, 2007. 1

[7] R. Swart, C. Coppens, H. Gordijn, M. Piek, P. Ruyssenaars, J. Schrander, P. de Smet, M. Hoogwijk, M. Papalexandrou, E. de Visser *et al.*, *Europe's onshore and offshore wind energy potential: An assessment of environmental and economic constraints.* European Environment Agency, 2009. 2, 9

[8] Energy Agency and Group of Eight, *Wind energy technology roadmap.* International Energy Agency, 2013. 2

[9] N. B. Negra, J. Todorovic, and T. Ackermann, "Loss evaluation of HVAC and HVDC transmission solutions for large offshore wind farms," *Electric power systems research*, vol. 76, no. 11, pp. 916–927, 2006. 2

[10] T. Halder, "Comparative study of HVDC and HVAC for a bulk power transmission," in *2013 International Conference on Power, Energy and Control (ICPEC)*, Feb 2013, pp. 139–144. 2

[11] P. Bresesti, W. L. Kling, R. L. Hendriks, and R. Vailati, "HVDC connection of offshore wind farms to the transmission system," *IEEE Transactions on Energy Conversion*, vol. 22, no. 1, pp. 37–43, March 2007. 2, 3

[12] T. Ackermann, "Transmission systems for offshore wind farms," *IEEE Power Engineering Review*, vol. 22, no. 12, pp. 23–27, Dec 2002. 2

[13] M. H. Okba, M. H. Saied, M. Z. Mostafa, and T. M. Abdel-Moneim, "High voltage direct current transmission - a review, part I," *2012 IEEE Energytech*, pp. 1–7, May 2012. 2

[14] T. Ackermann, "Transmission systems for offshore wind farms," *Wind Power in Power Systems*, pp. 479–504, 2005. 2

[15] O. Gomis-Bellmunt, J. Liang, J. Ekanayake, R. King, and N. Jenkins, "Topologies of multiterminal HVDC-VSC transmission for large offshore wind farms," *Electric Power Systems Research*, vol. 81, no. 2, pp. 271–281, 2011. 2, 3, 20, 26

[16] J. Liang, O. Gomis-Bellmunt, J. Ekanayake, and N. Jenkins, "Control of multi-terminal VSC-HVDC transmission for offshore wind power," in *2009 13th European Conference on Power Electronics and Applications*, Sept 2009, pp. 1–10. 3

[17] M. T. Hagh and M. Valizadeh, "Analysis and comparative study of transient inrush current reduction methods," in *2007 International Power Engineering Conference (IPEC 2007)*, 2007. 3, 67, 69, 74

[18] J. P. Bowles, "Overvoltages in HVDC transmission systems caused by transformer magnetizing inrush currents," *IEEE Transactions on Power Apparatus and Systems*, no. 2, pp. 487–495, 1974. 3, 69

[19] L. Cai and Z. Fan, "Doubly-fed induction generator offshore wind farm with VSC-HVDC grid connection: Start-up procedure," in *International Conference on Renewable Power Generation (RPG 2015)*, Oct 2015, pp. 1–6. 3, 68, 100

[20] EWEA, *The European Offshore Wind Industry–Key Trends and Statistics 2013*. European Wind Energy Association, 2014. 9

[21] Monica Aragues Penalba, "Operation and control of transmission systems for onshore wind power plants," in *PhD thesis, Universitat Politecnica de Catalunya,Barcelona*, February 2016. 10, 20, 21, 22, 23, 25

[22] J. Fortmann, *Modeling of Wind Turbines with Doubly Fed Generator System.* Springer, 2014. 13, 14

[23] M.Stiebler, *Wind Energy Systems for Electric Power Generation.* Springer, 2008. 13

[24] V. Vittal and R. Ayyanar, *Grid Integration and Dynamic Impact of Wind Energy.* Springer, 2012. 14, 15, 16

[25] T. Ackermann, *Wind power in power systems.* John Wiley & Sons, 2005. 15, 16

[26] E. Ahmed Masmoudi, Z. Zhu, and J. Hu, "Electrical machines and power-electronic systems for high-power wind energy generation applications: Part I–market penetration, current technology and advanced machine systems," *International journal for computation and mathematics in electrical and electronic engineering (COMPEL)*, vol. 32, no. 1, pp. 7–33, 2012. 16

[27] M. Sathyajith, *Wind Energy: Fundamentals, Resource Analysis and Economics.* Springer, 2006. 16

[28] Thomas Haugsten Hansen, "Offshore wind farm layouts: Performance comparison for a 540 MW offshore wind farm," in *Master thesis submitted to University of NTNU, Department of electric Power Engineering*, 2009. 16

[29] S. Lumbreras and A. Ramos, "Offshore wind farm electrical design: a review," *wind Energy*, vol. 16, no. 3, pp. 459–473, 2013. 16, 17

[30] A. Sannino, H. Breder, and E. K. Nielsen, "Reliability of collection grids for large offshore wind parks," in *2006 International Conference on Probabilistic Methods Applied to Power Systems*, June 2006, pp. 1–6. 17, 19

[31] M. Damen, P. Bauer, S. de Haan, and J. Pierik, "Steady state electrical design, power performance and economic modeling of offshore wind farms," *EPE Journal*, vol. 16, no. 4, pp. 44–49, 2006. 17, 19

[32] M. A. Parker and O. Anaya-Lara, “Cost and losses associated with offshore wind farm collection networks which centralise the turbine power electronic converters,” *IET Renewable Power Generation*, vol. 7, no. 4, pp. 390–400, July 2013. 19

[33] Roy Maclean, “Electrical system design for the proposed one gigawatt beatrice offshore wind farm,” in *Master thesis, University of Strathclyde*, 2004. 19, 20

[34] X. Zhang, C. Rehtanz, and B. Pal, *Flexible AC Transmission Systems: Modelling and Control.* Springer, 2012. 20

[35] M. P. Bahrman and B. K. Johnson, “The ABCs of HVDC transmission technologies,” *IEEE Power and Energy Magazine*, vol. 5, no. 2, pp. 32–44, March 2007. 20, 21

[36] Silvio Miguel Fragoso Rodrigues, “Dynamic modeling and control of VSC-based multi-terminal DC networks,” in *PhD thesis, Universidade Tecnica de Lisboa*, December 2011. 20, 43

[37] H. Liu and Z. Chen, “Fault ride-through and grid support of permanent magnet synchronous generator-based wind farms with HVAC and VSC-HVDC transmission systems,” in *2012 IEEE International Energy Conference and Exhibition (ENERGYCON)*, Sept 2012, pp. 769–773. 20, 62, 122, 123

[38] N. Flourentzou, V. G. Agelidis, and G. D. Demetriades, “VSC-based HVDC power transmission systems: An overview,” *IEEE Transactions on Power Electronics*, vol. 24, no. 3, pp. 592–602, March 2009. 20

[39] A. Egea-Alvarez, A. Junyent-Ferré, and O. Gomis-Bellmunt, “Active and reactive power control of grid connected distributed generation systems,” in *Modeling and control of sustainable power systems.* Springer, 2012, pp. 47–81. 29, 30, 39, 41, 42, 51

[40] Agusti. Egea- Alvarez, “Multiterminal HVDC transmission systems for offshore wind,” in *PhD thesis, Universitat Politecnica de Catalunya,Barcelona*, July 2014. 29, 60, 102, 123

[41] G. Zhang, Z. Xu, and Y. Cai, “An equivalent model for simulating VSC based HVDC,” in *2001 IEEE/PES Transmission and Distribution Conference and Exposition*, vol. 1, 2001, pp. 20–24. 30

[42] Christian Ismunandar, “Control of multi-terminal VSC-HVDC for offshore wind power integration,” in *PhD thesis, Delft University of Technology*, August 2010. 30, 43

[43] Silvio Miguel Fragoso Rodrigues, “Dynamic modeling and control of VSC-based multi-terminal DC networks,” in *PhD thesis, Universiidade Tecnica de Lisboa*, December 2011. 31

[44] E. Prieto-Araujo, A. Egea-Alvarez, S. Fekriasl, and O. Gomis-Bellmunt, “DC voltage droop control design for multi-terminal hvdc systems considering AC and DC grid dynamics,” in *2016 IEEE Power and Energy Society General Meeting (PESGM)*, July 2016, pp. 1–1. 33

[45] A. Lindberg and L. Lindberg, “Inner current loop for large voltage low switching frequency,” in *Fifth International Conference on Power Electronics and Variable-Speed Drives*, Oct 1994, pp. 217–222. 37

[46] S. Cole and R. Belmans, “A proposal for standard VSC-HVDC dynamic models in power system stability studies,” *Electric Power Systems Research*, vol. 81, no. 4, pp. 967–973, 2011. 37

[47] L. Zhang and H. P. Nee, “Multivariable feedback design of VSC-HVDC connected to weak ac systems,” *2009 IEEE Bucharest PowerTech*, pp. 1–8, June 2009. 37

[48] L. Harnefors and H. P. Nee, “Model-based current control of AC machines using the internal model control method,” *IEEE Transactions on Industry Applications*, vol. 34, no. 1, pp. 133–141, Jan 1998. 41

[49] J. Morren and S. W. H. de Haan, “Ridethrough of wind turbines with doubly-fed induction generator during a voltage dip,” *IEEE Transactions on Energy Conversion*, vol. 20, no. 2, pp. 435–441, June 2005. 41

[50] A. Yazdani and R. Iravani, *Voltage-sourced converters in power systems: modeling, control, and applications.* John Wiley & Sons, 2010. 44, 45, 46

[51] Z. Solhjoukhah, A. Egea-Alvarez, and O. Gomis-Bellmunt, “Voltage control of offshore load connected to a multi-terminal HVDC transmission system,” in *11th IET International Conference on AC and DC Power Transmission*, Feb 2015, pp. 1–9. 46, 128

[52] Q. b. Jin, S. b. Ren, and L. Quan, "LQG optimum controller design and simulation base on inter model control theory," in *2009 IEEE International Conference on Intelligent Computing and Intelligent Systems*, vol. 3, Nov 2009, pp. 62–65. 46

[53] E. Prieto-Araujo, F. D. Bianchi, A. Junyent-Ferre, and O. Gomis-Bellmunt, "Methodology for droop control dynamic analysis of multiterminal VSC-HVDC grids for offshore wind farms," *IEEE Transactions on Power Delivery*, vol. 26, no. 4, pp. 2476–2485, Oct 2011. 51

[54] C. Nentwig, J. Haubrock, R. H. Renner, and D. V. Hertem, "Application of DC choppers in HVDC grids," in *2016 IEEE International Energy Conference (ENERGYCON)*, April 2016, pp. 1–5. 53

[55] O. Gomis-Bellmunt, J. Liang, J. Ekanayake, and N. Jenkins, "Voltage–current characteristics of multiterminal HVDC-VSC for offshore wind farms," *Electric Power Systems Research*, vol. 81, no. 2, pp. 440–450, 2011. 54

[56] Abram Perdana, "Dynamic models of wind turbines," in *PhD thesis, Chalmers University of Technology*, May 2008. 58

[57] Adria Junyent-Ferre, "Control of power electronic converters for the operation of wind generation systems under grid disturbances," in *PhD thesis, Universitat Politecnica de Catalunya, Barcelona*, May 2011. 61

[58] L. Peng, W. Ye, W. Yuting, H. Haosheng, and Y. Yubo, "Characteristic and influence analysis on the inrush current of HVDC converter transformer," in *2014 International Conference on Power System Technology (POWERCON)*, Oct 2014, pp. 281–286. 67

[59] Z. Hong-yue, "Thinking of converter connection-transformer differential protection's magnetizing inrush current judgement," *Power System Protection and Control*, vol. 39, no. 20, pp. 151–154, 2011. 67

[60] R. Turner, K. S. Smith *et al.*, "Transformer inrush currents," *IEEE Industry Applications Magazine*, vol. 16, no. 5, pp. 14–19, 2010. 67, 70, 73, 82, 85, 171

[61] G. Ning, W. Aiyuan, W. Jie, L. Haitao, and R. Zhong, "Analysis and reduction of magnetizing inrush current for switch-on unloaded

transformer," in *2013 2nd International Symposium on Instrumentation and Measurement, Sensor Network and Automation (IMSNA)*, Dec 2013, pp. 1022–1026. 67

[62] M. Rahman and A. Gangopadhyay, "Digital simulation of magnetizing inrush currents in three-phase transformers," *IEEE Transactions on Power Delivery*, vol. 1, no. 4, pp. 235–242, Oct 1986. 67

[63] F. de Leon, A. Farazmand, and P. Joseph, "Comparing the T and *pi* equivalent circuits for the calculation of transformer inrush currents," *IEEE Transactions on Power Delivery*, vol. 27, no. 4, pp. 2390–2398, Oct 2012. 68, 78, 79

[64] N.Chiesa, Hoidalen, Lambert, and Martinez, "Calculation of inrush currents–benchmarking of transformer models," in *IPST Conference, Delft*, 2011. 68

[65] JR.M.Holmukhe and K.D.Deshpande, "Power transformer inrush currents and its effects on protective relays," *i-cost electronics cenference Proceeding*, 2011. 68, 70, 72

[66] S. Kumar, K. Kant, D. Tiwari, S. Bhil, S. Wagh *et al.*, "Prefluxing technique to mitigate inrush current of three-phase power transformer," in *Asia-Pacific International Symposium and Exhibition on Electromagnetic Compatibility: APEMC*, 2013, p. 207. 68, 69, 70, 74, 75, 77, 78

[67] R. Ekström, S. Apelfröjd, and M. Leijon, "Transformer magnetizing inrush currents using a directly coupled voltage-source inverter," *ISRN Electronics*, vol. 2013, 2013. 68, 70, 74

[68] S. D. Bole, "Mitigation of inrush current in transformer," *International Journal of Innovative Technology and Exploring Engineering (IJITEE)*, pp. 2278–3075. 68, 70, 74, 75, 174

[69] M. Wani, K. Kurundkar, and M. P. Bhawalkar, "Use of power electronic converters to suppress transformer inrush current," in *2012 IEEE International Conference on Power Electronics, Drives and Energy Systems (PEDES)*, Dec 2012, pp. 1–5. 68, 74, 75

[70] A. Rasic, G. Herold, and U. Krebs, "Fast connection /reconnection of the VSC to the power network," in *2007 European Conference on Power Electronics and Applications*, Sept 2007, pp. 1–8. 68, 74, 172

[71] Zoran Gajic, "Differential protection methodology for arbitrary three-phase power transformers," in *9th IET International Conference on Developments in Power System Protection (DPSP 2008)*, March 2008, pp. 44–49. 69, 72

[72] J. Holcomb, "Distribution transformer magnetizing inrush current," *Transactions of the American Institute of Electrical Engineers. Part III: Power Apparatus and Systems*, vol. 80, no. 3, pp. 697–702, April 1961. 69

[73] A. Tokit and G. tumberger, *Wind Farm Transformer Inrush Studies.* Manitoba HVDC Research Centre Inc. 69, 79, 82, 85, 175

[74] G. Wojtasiewicz, G. Komarzyniec, T. Janowski, S. Kozak, J. Kozak, M. Majka, and B. Kondratowicz-Kucewicz, "Inrush current of superconducting transformer," *IEEE Transactions on Applied Superconductivity*, vol. 23, no. 3, pp. 5 500 304–5 500 304, June 2013. 70, 174

[75] R. S. Girgis and E. G. Tenyenhuis, "Characteristics of inrush current of present designs of power transformers," in *2007 IEEE Power Engineering Society General Meeting*, June 2007, pp. 1–6. 70, 71, 72

[76] F. Asghar and K. Basu, "Reduction of three-phase transformer magnetizing inrush current by use of point-on-wave switching," in *2009 IEEE Student Conference on Research and Development (SCOReD)*, Nov 2009, pp. 368–370. 70

[77] Nilesh Deokar, Harpreet Singh, "Mitigation and analysis of three-phase transformer magnetizing inrush current by using point-on-wave switching method," *International Journal of Emerging Technology and Advanced Engineering*, vol. 4, 2014. 70

[78] N. Chiesa, B. Mork, and H. Hoidalen, "Transformer model for inrush current calculations: Simulations, measurements and sensitivity analysis," *IEEE Transactions on Power Delivery*, vol. 25, no. 4, pp. 2599–2608, Oct 2010. 70, 85, 86, 175

[79] M. Yazdani-Asrami, A. Yousefi-Talouki, and M. Mirzaie, "Assessment of inrush current for power transformers by three-dimensional representation," *Research Journal of Applied Sciences, Engineering and Technology*, vol. 4, no. 5, pp. 533–538, 2012. 70

[80] J. Wang and R. Hamilton, "Analysis of transformer inrush current and comparison of harmonic restraint methods in transformer protection," in *2008 61st Annual Conference for Protective Relay Engineers*, April 2008, pp. 142–169. 71, 72, 170, 171

[81] L. Blume, G. Camilli, S. Farnham, and H. Peterson, "Transformer magnetizing inrush currents and influence on system operation," *Transactions of the American Institute of Electrical Engineers*, vol. 63, no. 6, pp. 366–375, June 1944. 71, 73, 77

[82] S. K. Agasti, R. Naresh, and N. Ghosh, "Investigation of various affecting factors and reduction technique of transformer magnetizing inrush current," in *2016 International Conference on Computation of Power, Energy Information and Commuincation (ICCPEIC)*, April 2016, pp. 307–310. 73

[83] Aaliyaa Mohammad, Hadya Mohammad, "Modelling of an inrush current using matlab," *International Journal of Electrical Electronics Engineering Advanced Research*, vol. 1, 2013. 74

[84] Nicola Chiesa, "Power transformer modeling for inrush current calculation," in *PhD thesis, University of NTNU*, 2010. 74

[85] JINSHENG PENG, "Assessment of transformer energisation transients and their impacts on power systems," in *PhD thesis, University of Manchester*, 2013. 74

[86] A. Ebner, "Transient transformer inrush currents due to closing time- and residual flux measurement-deviations if controlled switching is used," *unpublished*, 2007. 75, 171, 172

[87] Sami G.Abdulsalam and Wilsun Xu, "Analytical study of transformer inrush current transients and its applications," in *International Conference on Power Systems Transients (IPST05)*, 2005, pp. 140–145. 76

[88] R. Yacamini and A. Abu-Nasser, "Transformer inrush currents and their associated overvoltages in HVDC schemes," *IEE Proceedings C - Generation, Transmission and Distribution*, vol. 133, no. 6, pp. 353–358, September 1986. 79

[89] G. Tsourakis, I. Milis, and J. Prousalidis, "Transformer sympathetic inrush: A case study," in *8th Mediterranean Conference on Pow-*

er Generation, Transmission, Distribution and Energy Conversion (MEDPOWER 2012), Oct 2012, pp. 1–5. 79

[90] S. Abdulsalam, W. Xu, W. Neves, and X. Liu, "Estimation of transformer saturation characteristics from inrush current waveforms," *IEEE Transactions on Power Delivery*, vol. 21, no. 1, pp. 170–177, Jan 2006. 79, 80, 81, 82, 83, 85, 88, 175

[91] S. Javadi, B. Vahidi, and S. H. Hosseinian, "Three phase transformer modeling with consideration the core effect," in *2008 International Conference on Electrical Machines and Systems*, Oct 2008, pp. 4375–4378. 79, 81, 82, 88

[92] A. Tokić, I. Uglešić, and G. Štumberger, "Simulations of transformer inrush current by using BDF-based numerical methods," *Mathematical Problems in Engineering*, vol. 2013, 2013. 81, 82, 86, 87

[93] G. Baoming, A. de Almeida, Z. Qionglin, and W. Xiangheng, "An equivalent instantaneous inductance-based technique for discrimination between inrush current and internal faults in power transformers," *IEEE Transactions on Power Delivery*, vol. 20, no. 4, pp. 2473–2482, Oct 2005. 83, 85, 86

[94] Shin-Der Chen and Ray-Lee Lin and Chih-Kun Cheng, "Magnetizing inrush model of transformers based on structure parameters," *IEEE Transactions on Power Delivery*, vol. 20, no. 3, pp. 1947–1954, July 2005. 85

[95] P. Wang, Z. Li, X. P. Zhang, and P. F. Coventry, "Start-up sequences of an offshore integrated MMC MTDC system," in *11th IET International Conference on AC and DC Power Transmission,*, Feb 2015, pp. 1–7. 99, 102

[96] I. Arana, A. Hernandez, G. Thumm, and J. Holboell, "Energization of wind turbine transformers with an auxiliary generator in a large offshore wind farm during islanded operation," *IEEE Transactions on Power Delivery*, vol. 26, no. 4, pp. 2792–2800, Oct 2011. 100

[97] L. Xiang and H. Min-xiao, "Direct virtual power control of VSC-HVDC for starting up of offshore wind farm," in *2013 IEEE PES Asia-Pacific Power and Energy Engineering Conference (APPEEC)*, Dec 2013, pp. 1–6. 102

[98] W. Li, Y. Kang, G. Tang, and M. Kong, “Start-up and integration of DFIG-based wind farm using modular multilevel VSC-HVDC transmission system,” in *2014 IEEE Applied Power Electronics Conference and Exposition (APEC 2014)*, March 2014, pp. 358–365. 102, 105

[99] J. A. Cortajarena, J. D. Marcos, P. Alvarez, F. J. Vicandi, and P. Alkorta, “Start up and control of a DFIG wind turbine test rig,” in *37th Annual Conference on IEEE Industrial Electronics Society*, Nov 2011, pp. 2030–2035. 105

[100] J. Da Silva, R. De Oliveira, S. Silva, B. Rabelo, W. Hofmann *et al.*, “A discussion about a start-up procedure of a doubly-fed induction generator system,” in *Nordic Workshop on Power and Industrial Electronics (NORPIE/2008).* Helsinki University of Technology, 2008. 105

[101] L. Xu, L. Yao, and C. Sasse, “Grid integration of large DFIG-based wind farms using VSC transmission,” *IEEE Transactions on Power Systems*, vol. 22, no. 3, pp. 976–984, Aug 2007. 105

[102] Mojtaba Khederzadeh, “Mitigation of the impact of transformer inrush current on voltage sag by TCSC,” *Electric Power Systems Research*, vol. 80, no. 9, pp. 1049–1055, 2010. 121

[103] J. Pedra, L. Sainz, F. Corcoles, and L. Guasch, “Symmetrical and unsymmetrical voltage sag effects on three-phase transformers,” *IEEE Transactions on Power Delivery*, vol. 20, no. 2, pp. 1683–1691, April 2005. 121, 122, 179, 180

[104] L. Guasch, F. Corcoles, J. Pedra, and L. Sainz, “Effects of symmetrical voltage sags on three-phase three-legged transformers,” *IEEE Transactions on Power Delivery*, vol. 19, no. 2, pp. 875–883, April 2004. 121, 122, 180, 181

[105] S. Chou, C. Lee, H. Ko, and P. Cheng, “A low-voltage ride-through method with transformer flux compensation capability of renewable power grid-side converters,” *IEEE Transactions on Power Electronics*, vol. 29, no. 4, pp. 1710–1719, April 2014. 121, 181

[106] J. Vaheeshan, M. Barnes, and R. Shuttleworth, “Dynamic analysis of a modular multilevel converter based VSC-HVDC system incorporating transformer magnetisation characteristics,” in *11th IET International Conference on AC and DC Power Transmission,*, Feb 2015, pp. 1–9. 122

[107] H. Chen, H.Ko, and P. Cheng, “An inrush current mitigation method for the grid-connected converters in the low-voltage ride-through operation,” in *2013 IEEE Energy Conversion Congress and Exposition (ECCE)*, Sept 2013, pp. 1717–1724. 122

[108] Y. Wang, X. Su, and X. Han, “Fault ride-through control of the wind farm integrated with VSC-HVDC,” in *2013 International Conference on Electrical Machines and Systems (ICEMS)*, Oct 2013, pp. 267–272. 122

[109] S. Shilpa Mishra, Sandeep Shukla, “Performance analysis and limitations of grid connected DFIG wind turbine under voltage sag and 3-phase fault,” in *International Journal of Engineering Research and Development*, Sept 2013, pp. 1717–1724. 122

[110] M. Mohseni, S.Islam, and M. Masoum, “Impacts of symmetrical and asymmetrical voltage sags on DFIG-based wind turbines considering phase-angle jump, voltage recovery, and sag parameters,” *IEEE Transactions on Power Electronics*, vol. 26, no. 5, pp. 1587–1598, May 2011. 126

[111] U.A.Bakshi and V.Bakshi, *Magnetic Circuits and Transformers.* Technical Publications, 2008. 169

[112] R. Yacamini and H. Bronzeado, “Transformer inrush calculations using a coupled electromagnetic model,” *IEE Proceedings-Science, Measurement and Technology*, vol. 141, no. 6, pp. 491–498, 1994. 170

[113] Y. Husianycia and M. Rioual, “Determination of the residual fluxes when de-energizing a power transformer / comparison with on-site tests,” in *2005 IEEE Power Engineering Society General Meeting*, June 2005, pp. 449–454. 171

[114] W. Ge, Y. Wang, Z. Zhao, X. Yang, and Y. Li, “Residual flux in the closed magnetic core of a power transformer,” *IEEE Transactions on Applied Superconductivity*, vol. 24, no. 3, pp. 1–4, June 2014. 171, 172

[115] M. Vanti, S. Bertoli, S. Cabral, A. Gerent, and P. Kuo, “Semianalytic solution for a simple model of inrush currents in transformers,” *IEEE Transactions on Magnetics*, vol. 44, no. 6, pp. 1270–1273, June 2008. 172

[116] M. Rioual and C. Sicre, "Energization of a no-load transformer for power restoration purposes: sensitivity to parameters," in *2000 IEEE Power Engineering Society Summer Meeting*, vol. 2, 2000, pp. 892–895. 172

[117] D. Taylor, N. Fischer, J. Law, and B. Johnson, "Using labVIEW to measure transformer residual flux for inrush current reduction," in *2009 North American Power Symposium (NAPS).* IEEE, 2009, pp. 1–6. 173, 174

[118] Y. Tao, W. Man-fang, R. Zhen, and C. Ka-wing, "Simulation study of impact of transformer excitation inrush current on oil-fired thermal plants as black-start sources," in *2005 IEEE/PES Transmission and Distribution Conference and Exhibition: Asia and Pacific*, 2005, pp. 1–4. 174, 179

[119] L. Prikler, G. Bánfai, G. Bán, and P. Becker, "Reducing the magnetizing inrush current by means of controlled energization and de-energization of large power transformers," *Electric power systems research*, vol. 76. 174

Appendix A

Synchronous reference frame and Droop controller

A.1 Park transformation

To enable the control scheme of a three-phase converter system and provide a simpler structure, the system variables such as currents and voltages require to become constant values in steady state. Therefore, under such condition, the rejection of disturbances and tracking the reference signals by means of the PI and other regulators will be possible. Hence, a Park transformation known as synchronous reference frame is applied to achieve the fixed quantities. Note that the Park transformation synthesizes the Clarke transformation and a rotation.
The transformation of the x_{abc} vector to a qd0 frame with angle θ is characterized as:

$$x_{qd0} = T(\theta) x_{abc} \tag{A.1}$$

where x_{abc} is a vector with the three-phase quantities in the stationary frame and x_{qd0} is a vector with the transformed quantities in the qd0 frame.
The Park transformation matrix $T(\theta)$ is defined as

$$T(\theta) = \frac{2}{3} \begin{bmatrix} \cos(\theta) & \cos(\theta - \frac{2\pi}{3}) & \cos(\theta + \frac{2\pi}{3}) \\ \sin(\theta) & \sin(\theta - \frac{2\pi}{3}) & \sin(\theta + \frac{2\pi}{3}) \\ \frac{1}{2} & \frac{1}{2} & \frac{1}{2} \end{bmatrix} \tag{A.2}$$

Since the matrix $T(\theta)$ is invertible, the inverse transformation can be obtained as

$$x_{abc} = T^{-1}(\theta)x_{qd0} \tag{A.3}$$

with

$$T^{-1}(\theta) = \begin{bmatrix} \cos(\theta) & \sin(\theta) & 1 \\ \cos(\theta - \frac{2\pi}{3}) & \sin(\theta - \frac{2\pi}{3}) & 1 \\ \cos(\theta + \frac{2\pi}{3}) & \sin(\theta + \frac{2\pi}{3}) & 1 \end{bmatrix} \tag{A.4}$$

In present thesis, the q-and d-axes deal with the active and reactive powers, respectively.

A.2 Instantaneous power theory in the synchronous reference frame

A sinusoidal three-phase signal, $x_{abc}(t)$, can be presented as

$$x_{abc}(t) = \sqrt{2}X \begin{bmatrix} \cos(\omega t + \varphi_x) \\ \cos(\omega t + \varphi_x - \frac{2\pi}{3}) \\ \cos(\omega t + \varphi_x + \frac{2\pi}{3}) \end{bmatrix} \tag{A.5}$$

Using the Park transformation matrix, $T(\theta)$, for a general signal, $x_{abc}(t)$, and replacing $\theta = \omega t + \varphi$, a $x_{qd0}(t)$ signal can be derived as

$$x_{qd0}(t) = T(\omega t + \varphi)x_{abc} = \sqrt{2}X \begin{bmatrix} \cos(\varphi_x - \varphi) \\ -\sin(\varphi_x - \varphi) \\ 0 \end{bmatrix} \tag{A.6}$$

The voltage and current in synchronous reference can be expressed in the conventional phasor form, namley

$$V_{qd} = \frac{1}{\sqrt{2}}(v_q - jv_d) \tag{A.7}$$

$$I_{qd} = \frac{1}{\sqrt{2}}(i_q - ji_d) \tag{A.8}$$

Thus, the three-phase power can be concluded as

$$S = P + jQ = 3V_{qd}I_{qd} = 3(\frac{1}{\sqrt{2}}(v_q - jv_d))(\frac{1}{\sqrt{2}}(i_q - ji_d)) \tag{A.9}$$

As a result, the instantaneous active and reactive powers can be represented as functions of the instantaneous voltages and currents as

$$P = \frac{3}{2}(v_q i_q + v_d i_d) \tag{A.10}$$

$$Q = \frac{3}{2}(v_q i_d - v_d i_q) \tag{A.11}$$

And considering the system voltage is aligned with the q-axis and the $v_d = 0$, the active and reactive powers can be simplified as follows

$$P = \frac{3}{2}v_q i_q \tag{A.12}$$

$$Q = \frac{3}{2}v_q i_d \tag{A.13}$$

From previous equations, it can be deduced that the active and reactive powers can be independently regulated by the active current and reactive current, i_q and i_d, respectively.

A.3 Droop controller design

At high DC voltages, the converter keeps the voltage approximately fixed by a proportional control law, so-called droop control. There are several droop implementations in order to achieve the control of the DC voltage. The current and power based droop controls are the most prevalent type of these controllers.

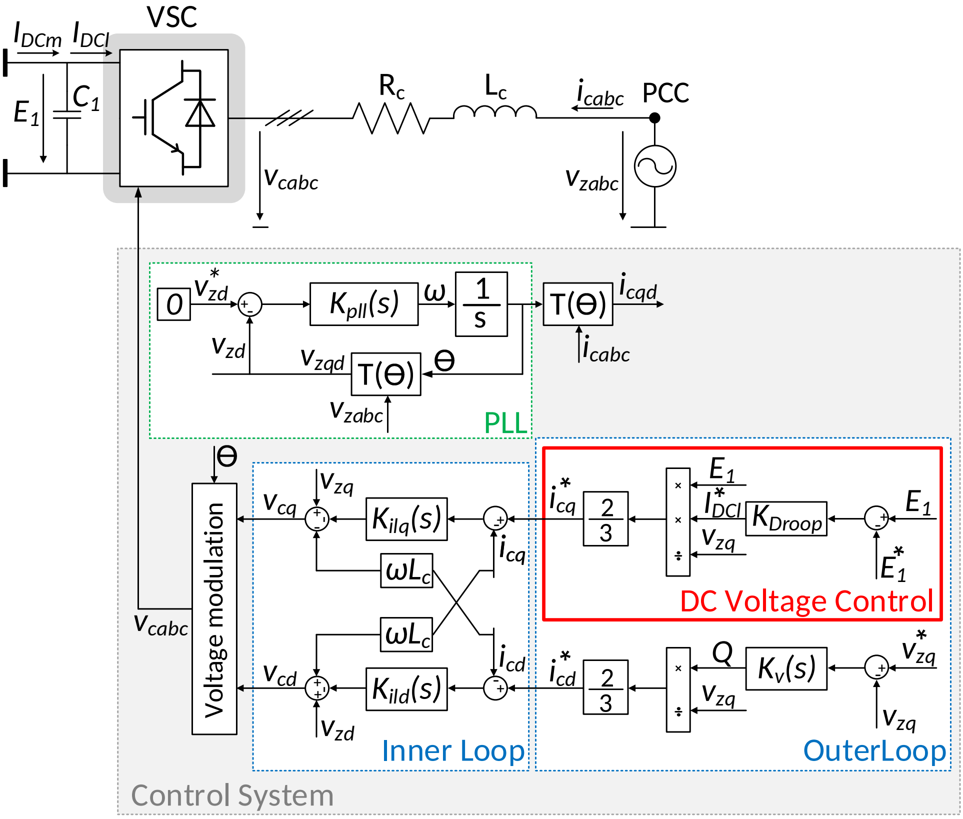

Figure A.1: Scheme of the DC voltage droop control in a converter linked to the main AC grid through L coupling filter.

In this study, the current based control is used to regulate the DC current based on the DC voltage. The reasons are that the mentioned method reflects linear control behavior as well as the droop scheme is associated with the dynamics of the DC system.
Furthermore, the droop design is according to the calculation of the DC

current extracted by the converter.

$$i^*_{DCl} = k_{droop}(E_1 - E_1^*) \tag{A.14}$$

Where i^*_{DCl} denotes the DC current reference of the converter, E_1^* and E_1 represent the reference and actual values of converter DC voltage, respectively. The k_{droop} is the proportional coefficient which depends on the design of control system.
The scheme of a DC voltage droop controller is sketched in Figure A.1.

Appendix B

Magnetic characteristics

B.1 Introduction

This appendix presents a summary of the magnetic characteristics of transformer core such as $B - H$ curve, residual flux and saturation flux in order to realize the inrush transient phenomenon.

B.2 The $B - H$ curve

For magnetic material of transformer core, there is a relationship between the magnetic flux density (B) and the magnetic field strength (H) which can be represented as a graph [111]. The mentioned graph is called magnetization curve or $B - H$ curve.

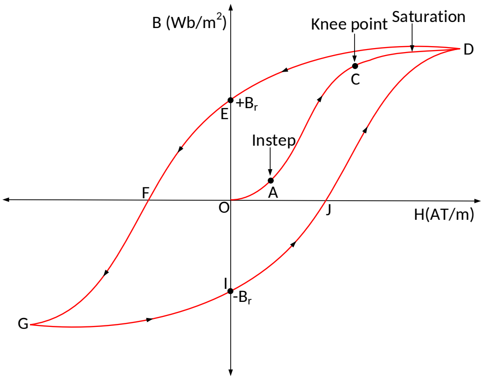

Figure B.1: B-H curve.

The above nonlinear $B - H$ curve illustrates a hysteresis loop which consists of some portions as: [111]
OACD:

- Initial segment (O-A): In this portion, the amount of flux density does not rapidly increase for the low values of the magnetic field strength. This section can be shown by curve OA. The point A is called as instep.

- Middle segment (A-C): In this section, when H enhances, the B increases quickly. This is almost straight line curve. At point C, it starts bending again. The point C in which this segment bends is called as knee point.

- Saturation segment (C-D):
  After the knee point, rate of increment in B decreases drastically and the slope $\frac{dB}{dH}$ in this portion becomes a air-core inductance.
  Eventually, the curve becomes parallel to H axis indicating that any increase in H is not going to cause any variation in B. This area is known as saturation region.

D-E: In this part, current is reduced to zero, but core can not be completely demagnetized. OE represents the residual magnetism and residual flux density (B_r).
E-F: The current is reversed and increased in the reversed direction to get complete demagnetization of the core.
F-G: In the FG region, the current is increased in reversed direction till saturation in opposite direction is achieved.
G-I: Here, the current is reduced to zero but again flux density lags and core can not be completely demagnetized. OI represents residual flux density in other direction i.e. $-B_r$.
I-J: The current is again reversed and increase till complete demagnetization is achieved.
J-D: In this region, the current is again increased in original direction till saturation is reached.
It should be noted that the nonlinear $B-H$ curve can be represented as a piece-wise linear curve, as shown in Figure B.2 [112].
To convert the $(B-H)$ curve to a $(\phi-i)$ curve, two equations are applied as follows [80]

$$I = \frac{d}{N}H \tag{B.1}$$

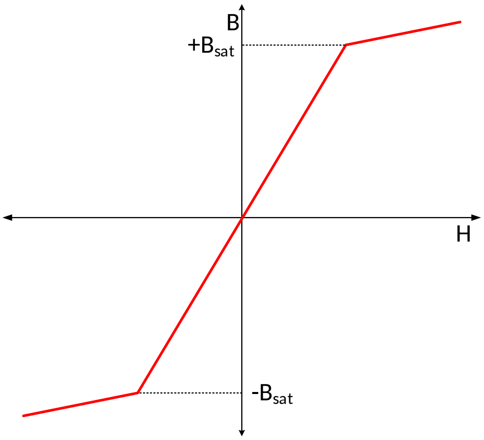

Figure B.2: Piecewise linear B-H curve.

$$\phi = BA \tag{B.2}$$

Where I represents the magnetizing current, N is the number of turns per phase, d shows the mean length of the winding, ϕ is the flux and A is the cross-sectional area of the core.

The amount of A is dependent on the situation of the magnetic flux density (B) relative to the saturation point of the $B-H$ curve [80, 86].

According to Equations (B.1) and (B.2), it can be concluded that the variations of B and H lead to the changing of the flux and magnetizing current, respectively.

Moreover, the $(\phi - i)$ characteristic curve of the transformer core is provided by the manufacturer [86].

B.3 Residual flux

At the instant of transformer disconnection from a supply source, a certain amount of flux will remain in the magnetic core which is called residual flux (Φ_r) [60]. In fact, the reason of its occurrence is the remanent magnetization of the core after the transformer de-energization [113].

The existence of residual flux, as initial magnetic flux left in the core, represents one of the hysteresis characteristics of the core. This flux is a vector with direction and numerical value [114]. Figure B.3 illustrates a hysteresis curve for a core driven into the saturation. In this figure, $\pm\Phi_r$ shows the residual flux when the transformer is de-energized and Subsequently, the current is interrupted.

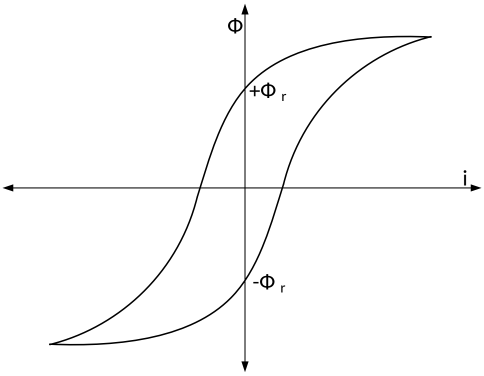

Figure B.3: Hysteresis loop.

The direct measurements of the residual flux in the transformer core are not easy, therefore, several indirect techniques are available in order to approximate it [70, 114]. The most well-known method for obtaining the residual flux is based on the integration of the winding voltage during the de-energization process. [70, 115, 116].

Hence, the residual flux can be calculated by the following equation at the time of transformer de-energization, $t_{de-energization}$ [86].

$$\phi_r = \frac{1}{N}\int v(t)dt \qquad \text{(B.3)}$$

using $v(t) = v_0 \sin(\omega_0 t)$ in the Equation (B.3), it can be deduced that [86]

$$\phi_r = -\phi_0 \cos(\omega_0 t_{de-energization}) \qquad \text{(B.4)}$$

Due to the presence of DC component, the estimation of residual flux by using this approach is hardly fulfilled.

The residual flux magnitude for power transformers is usually in the range of 70 to 100 % of the nominal magnetic flux [1].

$$0.7(p.u.)\,\langle|\phi_r|\,\langle 1(p.u)(\text{B.5})$$

It is noticeable that the magnitude and polarity of residual flux in the transformer core influences on the peak inrush current [114]. Hence, the study of residual flux has a considerable importance in the investigation of inrush current.

For the three-phase transformer energization in this chapter, it is assumed that the Φ_r includes the values of +94, -94 and +84 % of the magnetizing flux in the first, second and third limbs of transformer, respectively.

B.4 Saturation flux

Figure B.4 illustrates how the magnitude of the inrush current are related to the residual flux and the angle of the system voltage at the time of switching on.

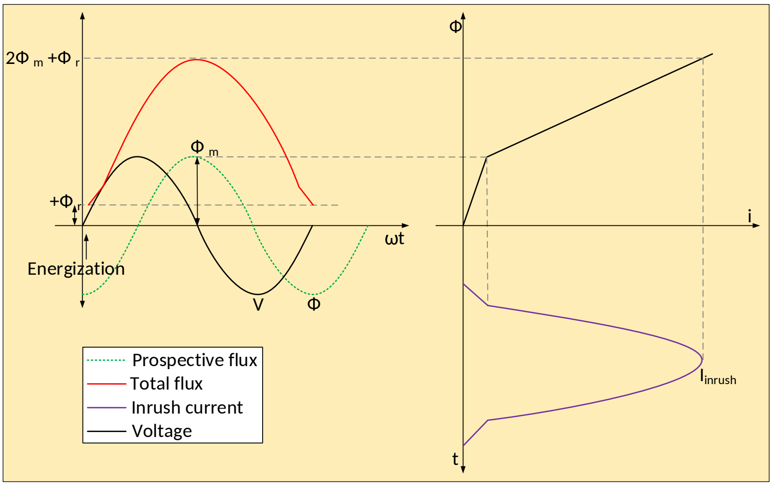

Figure B.4: Magnetic flux and inrush current during core saturation.

As shown in Figure B.4, a no-load transformer with a positive residual flux is energized at the positive zero crossing of the sinusoidal voltage.

At this instant, the prospective flux has the peak value with a 90 electrical degree delay and also it is the same direction with the residual flux. The mentioned prospective flux will circulate within the transformer core under steady-state conditions and its value is obtained by the integral of the energized voltage. Therefore, a total flux in the magnetic core of transformer which is sum of the prospective flux and the residual flux is generated and follows the residual flux and attains its highest amplitude with a 180 electrical degrees delay [117].

The total flux of the magnetic core during the first period of energization can be mathematically characterized by [117]

$$\phi(t) = \frac{1}{N}\int v(t)dt + \phi_r \tag{B.6}$$

solving of the Equation (B.6) and substituting $v = v_m \sin(\omega t + \theta)$ and $\phi_m = \frac{v_m}{N\omega}$, the total flux can be deduced as follows [118]

$$\phi = -\phi_m \cos(\omega t + \theta) + \phi_m \cos(\theta) + \phi_r \tag{B.7}$$

where v_m is peak value of the applied primary voltage, θ is the phase angle of voltage at switching instant, ϕ_m is the peak value of magnetic flux, ϕ_r is the transformers residual flux and N is the number of turns in the primary winding [117].

Once transformer is switched on at the positive zero crossing of the sinusoidal voltage, e.g. $\theta = 0$, and the direction of prospective flux is equal with that of the residual flux and also $\omega t = \pi$, the highest magnitude of the total flux becomes [74, 68]

$$\phi = 2\phi_m + \phi_r \tag{B.8}$$

Consequently, at this level of flux, the magnetic core is fully saturated and hence, a high unsymmetrical magnetizing current corresponding to this total flux is drawn by the primary winding to be able to support this value of flux [117]. In this condition, the instantaneous inductance of the magnetic core is very low and equal to the air-core inductance of the transformer winding [119].

However, when the transformer is energized at the peak value of voltage, nam ely $\theta = \pi/2$, the transient flux and the inrush current will reduce, because the value of prospective flux is zero. Therefore, the value of total flux becomes $\phi_m + \phi_r$ [74].

Appendix C

Parameters calculation of the transformer equivalent circuit

C.1 Introduction

In order to use the T-equivalent circuit, the determination of its parameters is necessary. Hence, these specifications can be estimated from transformer geometry or from measurements of the open-circuit and short-circuit tests. Due to the manufacturers of power transformers do not usually prepare the design and construction information of transformers, the parameters can be derived from these tests [78]. The winding resistances and leakage inductances of the transformer equivalent circuit can be obtained based on the short circuit tests. Also, the magnetizing reactance and the resistance representing losses in the transformer core can be calculated through open circuit tests [73, 90].
In this study, due to the lack of information of open-circuit and short-circuit tests for transformer with power 350 MVA and voltage 195/33 kVA and also, the lack of the transformer geometry, the parameters are defined according to the following sections.

C.2 Voltage and current at the primary and secondary Windings

The nominal currents of primary and secondary windings are obtained based on the Equation (C.1)

$$I_n = \frac{S}{\sqrt{3}\ \ v_{L-L}} \tag{C.1}$$

where v_{L-L} shows the line voltage at the primary or secondary side and S is the power of three-phase transformer. Also, in the windings with structure of star

$$v_{phase} = \frac{v_{L-L}}{\sqrt{3}} \quad and \quad I_{phase} = I_{L-L} \tag{C.2}$$

and in the delta connected windings

$$v_{phase} = v_{L-L} \quad and \quad I_{phase} = \frac{I_{L-L}}{\sqrt{3}} \tag{C.3}$$

C.3 Winding resistances and the leakage inductances

In the three-phase transformers, the base impedance for the primary and secondary windings with configurations star, Y, and delta, Δ is defined as

$$Z_{bY} = \frac{v_{L-L}^2}{S} \tag{C.4}$$

$$Z_{b\Delta} = 3\ \frac{v_{L-L}^2}{S} \tag{C.5}$$

Based on the base impedance and the topology of windings (Y or Δ), the leakage inductance and resistance of both windings are calculated as

$$X = \frac{U_k}{100}\ Z_{b(Y/\Delta)} \tag{C.6}$$

$$L = \frac{X}{\omega} \tag{C.7}$$

$$R = \frac{U_R}{100}\ Z_{b(Y/\Delta)} \tag{C.8}$$

where ω is the angular frequency. It should be noted that U_R and U_K in the primary and secondary windings are identical.

C.4 Characteristics of the core

The magnetizing curve used in the saturation model of the transformer core can be approximated based on the fluxes and currents produced at the transformer primary winding during energization. These fluxes and currents are required for obtaining the magnetizing inductance and are as follows

$$\phi = \phi_{pu} \cdot\ \phi_b \tag{C.9}$$

$$i_{mag} = i_{pu} \cdot\ i_b \tag{C.10}$$

where the base of flux and current are computed as follows

$$\phi_b = \sqrt{2}\ \frac{v_{p,phase}}{\omega} \tag{C.11}$$

$$i_b = \sqrt{2}\ \frac{S}{v_{p,phase}} \tag{C.12}$$

where S is the power for single phase transformer and $v_{p,phase}$ is the phase voltage at the primary side. In this chapter, we assume that $\phi_{pu} = [0,\ 1.25,\ 1.45]$ pu and $i_{pu} = [0,\ 0.0012,\ 1]$ pu.

The value of core losses resistance is based on the nominal power of three-phase transformer and the voltage of the primary winding, which is defined as

$$R_m = R_{m,pu}\ \frac{v_{L-L}^2}{S} \tag{C.13}$$

It should be noted that $R_{m,pu}$=500 pu is applied in the Equation (C.13) in order to generate 0.2 of active loss at rated voltage.

Appendix D

Calculation of Flux offset impacting on recovery inrush current

Analytical calculation of DC component of total magnetic flux when the voltage returns to the pre-fault value is determined in this section. This DC component is the main reason of the transformer recovery inrush current generation. Hence, in order to obtain this factor, the total flux of the magnetic core, ϕ_j, which is sinusoidal, is characterized according to the following equations [103, 118].

$$\begin{aligned}\phi_j(t) &= \phi_{rj} + \frac{1}{N}\int_0^t v_j(t)dt \\ &= \phi_{rj} - \frac{v_{mj}}{N\omega}\sin(\theta_j - \pi/2) + \frac{v_{mj}}{N\omega}\sin(\omega t + \theta_j - \pi/2) \\ &= \underbrace{\phi_{rj} + \phi_{mj}\cos(\theta_j)}_{\equiv \phi_{j,dc}} - \underbrace{\phi_{mj}\cos(\omega t + \theta_j)}_{\equiv \phi_{j,steady-state}}\end{aligned} \tag{D.1}$$

where ϕ_{rj} represents the residual value of the magnetic flux, $v_j = v_{mj}\sin(\omega t + \theta_j)$, v_{mj} is peak value of the voltage applied to the transformer, θ_j is the phase angle of voltage, ϕ_{mj} is the peak value of magnetic flux and N is the number of turns in the primary winding.

In the steady-state operation of transformer, the DC component of total flux ,$\phi_{j,dc}$, is zero. Namely, the following condition is correct for the initial flux, as the mean value of the transformer flux is zero.

$$\phi_{mj}\cos(\theta_j) + \phi_{rj} = 0 \tag{D.2}$$

and accordingly, the equation of total flux in the steady-state can be deduced as

$$\phi = -\phi_{mj}\cos(\omega t + \theta_j) = \frac{v_{mj}}{N\omega}\sin(\omega t + \theta_j - \pi/2) \tag{D.3}$$

supposing the voltage sag occurrence in the system, the voltage applied to the transformer for conditions: before, during and after the sag can be expressed as [103, 104]

$$v_j = \begin{cases} v_j(t) = v_{mj}\sin(\omega t + \theta_j) & 0 \le t \le t_i \\ v_{j,sag}(t) = v_{mj,sag}\sin(\omega t + \theta_{j,sag}) & t_i \le t \le t_f \\ v_j(t) = v_{mj}\sin(\omega t + \theta_j) & t_f \le t \end{cases} \tag{D.4}$$

where pre- and post-sag voltages are equal to the peak voltage value (v_{mj}). Also, $v_{j,sag}$ represents the value of voltage during sag.
According to the Equation (D.1), the magnetic flux of transformer can be obtained at any instant even when the voltage varies under the sag. Therefore, the flux after the fault clearance can be defined as follows [103]

$$\phi_j(t) = \phi_{rj} + \frac{1}{N}\int_0^{t_i} v_j(t)dt + \frac{1}{N}\int_{t_i}^{t_f} v_{j,sag}(t)dt + \frac{1}{N}\int_{t_f}^{t} v_j(t)dt \tag{D.5}$$

where sag takes place between time interval $[t_i, t_f]$. These instants indicate the occurence time and the finish time of voltage sag, respectively. Considering the following equation [103].

$$\frac{1}{N}\int_0^{t} v_j(t)dt = \frac{1}{N}\int_0^{t_i} v_j(t)dt + \frac{1}{N}\int_{t_i}^{t_f} v_j(t)dt + \frac{1}{N}\int_{t_f}^{t} v_j(t)dt$$

$$\Rightarrow \frac{1}{N}\int_0^{t} v_j(t)dt - \frac{1}{N}\int_{t_i}^{t_f} v_j(t)dt = \frac{1}{N}\int_0^{t_i} v_j(t)dt + \frac{1}{N}\int_{t_f}^{t} v_j(t)dt \tag{D.6}$$

and substituting this equation in the expression (D.5), the post-sag flux can be written as

$$\phi_j(t) = \phi_{rj} + \frac{1}{N}\int_0^{t} v_j(t)dt + \frac{1}{N}\int_{t_i}^{t_f} (v_{j,sag}(t) - v_j(t))dt \tag{D.7}$$

where the two first terms are identical to the terms of the flux formula in the steady-state case of transformer. Therefore, the total magnetic flux as the voltage returns to the nominal value can be defined by additional DC magnetic flux to the steady-state flux.

$$\phi_j(t) = -\phi_{mj}\cos(\omega t + \theta_j) + \phi_{j,dc} \tag{D.8}$$

Hence, the DC component of the transformer total magnetic flux which is a constant component can be determined as follows

$$\phi_{j,dc}(t) = \frac{1}{N}\int_{t_i}^{t_f}(v_{j,sag}(t) - v_j(t))dt \tag{D.9}$$

where the magnetic flux deviation ($\phi_{j,dc}$) represents the flux disturbance induced by the grid voltage sag, v_j and $v_{j,sag}$ indicate the transformer voltage in the normal and sag conditions, respectively. The value of this DC component of flux ,$\phi_{j,dc}$, is not null when the voltage is recovered. As a result, the magnitude of total flux will be high under this situation and the transformer saturation phenomenon can easily take place.
Eventually, with assumptions $v_{j,sag} = hv_j$, $\Delta t = t_f - t_i$ and $\psi_i = \omega t_i + \theta_j$ and substituting in the previous equation, the value of constant flux can be concluded as

$$\begin{aligned}\phi_{j,dc}(t) &= \frac{1}{N}\int_{t_i}^{t_f}(h-1)v_j(t)dt\\ &= \frac{\sqrt{2}(h-1)v_{mj}}{N\omega}\Big[\sin(\omega t_f + \theta_j - \pi/2) - \sin(\omega t_i + \theta_j - \pi/2)\Big]\\ &= \frac{2\sqrt{2}(1-h)v_{mj}}{N\omega}\Big[\cos(\tfrac{\psi_i + \omega\Delta t}{2} - \pi/2).\sin(\tfrac{-\omega\Delta t}{2})\Big]\end{aligned} \tag{D.10}$$

where h is the magnitude of voltage sag [104, 105].